Investigation of Random Channel Effects on the Performance of Underwater Wireless Optical Communication Links

Ikenna Chinazaekpere Ijeh

▶ To cite this version:

Ikenna Chinazaekpere Ijeh. Investigation of Random Channel Effects on the Performance of Underwater Wireless Optical Communication Links. Signal and Image processing. Ecole Centrale Marseille (ECM), 2021. English. NNT : . tel-04278725

HAL Id: tel-04278725
https://hal.science/tel-04278725v1

Submitted on 10 Nov 2023

École Doctorale – 352

Unité de recherche – INSTITUT FRESNEL

THÈSE DE DOCTORAT

pour obtenir le grade de

DOCTEUR de l'ÉCOLE CENTRALE de MARSEILLE

Discipline :

Optique, Photonique et Traitement d'Image

TITRE DE LA THÈSE :

ÉTUDE DES EFFETS ALÉATOIRES DU CANAL DE TRANSMISSION POUR LES LIAISONS DE COMMUNICATION OPTIQUE SOUS-MARINE SANS-FIL

Par

IJEH Ikenna Chinazaekpere

Directeur de thèse: M. KHALIGHI Mohammad-Ali
Co-Directeur de thèse: M. HRANILOVIC Steve

Soutenue le 01 Décembre 2021

devant le jury composé de :

M. FRACASSO Bruno	IMT Atlantique, France	Président
M. DIOURIS Jean-François	Université de Nantes, France	Rapporteur
Mme LOSCRI Valeria	INRIA Lille-Nord Europe, France	Rapporteur
M. MAROT Julien	Aix-Marseille Université, France	Examinateur
M. KHALIGHI Mohammad-Ali	École Centrale Marseille, France	Dir. de thèse
M. HRANILOVIC Steve	Université McMaster, Canada	Co-Dir. de thèse

DOCTORAL SCHOOL – 352

Research unit – INSTITUT FRESNEL

DOCTORAL THESIS

to obtain the degree of Doctor of Philosophy

issued by ÉCOLE CENTRALE MARSEILLE

Discipline :

Optics, Photonics and Image Processing

THESIS TITLE :

INVESTIGATION OF RANDOM CHANNEL EFFECTS ON THE PERFORMANCE OF UNDERWATER WIRELESS OPTICAL COMMUNICATION LINKS

By

IJEH Ikenna Chinazaekpere

Thesis advisor: Dr. KHALIGHI Mohammad-Ali
Thesis co-advisor: Prof. HRANILOVIC Steve

Presented and defended on 01 December 2021

in front of the thesis committee composed of :

Prof. FRACASSO Bruno	IMT Atlantique, France	Panel Chair
Prof. DIOURIS Jean-François	Nantes University, France	Reviewer
Dr. LOSCRI Valeria	INRIA Lille-Nord Europe, France	Reviewer
Dr. MAROT Julien	Aix-Marseille University, France	Examiner
Dr. KHALIGHI Mohammad-Ali	École Centrale Marseille, France	Thesis advisor
Prof. HRANILOVIC Steve	McMaster University, Canada	Thesis co-advisor

Abstract

In underwater environments, there is an essential need for efficient wireless communication techniques in several applications, including installation monitoring, underwater robotics, port security, etc. Underwater wireless optical communications (UWOC) offer low implementation cost, low latency, high data rate, and energy efficiency, compared with traditional acoustic communications. Among the main challenges in the realization of UWOC links is to deal with link misalignments, which are particularly problematic in underwater applications where precise localization and tracking of mobile units is very challenging. In addition to these pointing errors (PEs), oceanic turbulence can further degrade the performance of UWOC links by causing random fluctuation of the received optical signal intensity.

This thesis focuses on the effect of pointing errors (PEs) and oceanic turbulence on the performance of UWOC links. More specifically, accurate mathematical and statistical channel modeling are developed, in particular, for the case of a vertical transmission link, e.g., between a buoy of a surface vessel and an underwater node or an autonomous underwater vehicle. There, PEs are modelled by taking into consideration the wind at the sea surface and Rx angular misalignments, in particular. Based on the proposed models, the impact of PEs and turbulence on the link performance are studied under various channel conditions. In addition, we consider the appropriate selection of the transmitter/receiver parameters in order to optimize the link performance based on the criteria of the average bit error rate and outage probability.

In this study, we consider a highly sensitive photodetector, i.e., a Silicon photo-multiplier, at the receiver in order to increase the operational range. Lastly, some preliminary experimental works have been carried out to assess the practical issues of establishing an UWOC link using a dedicated laboratory testbed. The presented work fosters the UWOC system design and research towards practical considerations of link deployment ensuring reliable communications.

KEYWORDS: Underwater wireless optical communications; Vertical underwater links; Link misalignment; Pointing errors; Oceanic turbulence; Silicon photo-multiplier.

Résumé

De nos jours, il y a un besoin grandissant pour établir des liaisons de communication sans-fil haut-débit dans diverses applications sous-marines, telles que la surveillance de l'environnement, la maintenance et la vérification des installations, la sécurité portuaire, etc. Les communications optiques sous-marines sans-fil (UWOC pour Underwater Wireless Optical Communications) offrent un débit de transmission élevé, une faible latence, une bonne efficacité énergétique et un faible coût de mise en œuvre, comparées aux communications acoustiques. L'un des principaux défis dans la réalisation des liaisons UWOC est de traiter les erreurs de pointage, qui sont particulièrement problématiques dans les applications sous-marines où la localisation et le suivi précis des unités mobiles sont très difficiles. De plus, les turbulences océaniques peuvent dégrader davantage les performances de ces liaisons en causant des fluctuations aléatoires de l'intensité du signal optique reçu.

Cette thèse s'intéresse aux effets des erreurs de pointage et des turbulences océaniques sur les performances des liens UWOC. Plus précisément, nous développons une modélisation mathématique et statistique précise du canal, en particulier, pour le cas d'un lien de transmission vertical. Ce dernier peut être établi entre une bouée ou un navire de surface d'une part et un capteur sous-marin ou encore un véhicule sous-marin autonome d'autre part. Les erreurs de pointage sont ainsi modélisées en prenant en compte l'effet du vent à la surface de la mer et les désalignements angulaires du récepteur, notamment. En utilisant les modèles proposés, nous étudions ensuite l'impact de ces effets aléatoires du canal sur les performances de la liaison. En outre, nous considérons la sélection appropriée des paramètres de l'émetteur et/ou du récepteur afin d'optimiser les performances de la liaison en termes du taux d'erreur binaire et de la probabilité de coupure (outage).

Dans cette étude, nous considérons un photo-détecteur ultra-sensible, qui consiste à un photo-multiplicateur en silicium (SiPM pour Silicon Photo-Multiplier), au niveau du récepteur afin d'augmenter la portée. Enfin, nous avons mené des travaux expérimentaux préliminaires à l'aide d'un banc d'essai de laboratoire pour appréhender les problèmes pratiques de l'établissement d'une liaison UWOC. Les résultats présentés dans cette thèse apportent de l'éclairage sur les considérations pratiques de déploiement des liaisons UWOC, qui peuvent être particulièrement profitables dans la conception de tels systèmes.

MOTS CLÉS : Communications optiques sous-marines sans-fil ; erreurs de pointage ; turbulences océaniques ; fiabilité des liaisons ; photo-multiplicateur en silicium.

Résumé étendu

L'environnement maritime occupe une grande majorité de la surface de la terre, et il n'est donc pas étonnant qu'il connaisse des avancées technologiques considérables. Les technologies de communication sous-marine sont les plus importantes pour de nombreuses applications telles que la surveillance des océans, la collecte et le transfert de données entre une station sous-marine et une station à la surface de l'eau, la détection et la maintenance des pannes de pipelines, la recherche, l'exploration et l'exploitation des ressources naturelles. Ces activités ont créé une forte demande pour des techniques de communication plus sophistiquées et fiables qui tiennent compte des particularités des moyens de propagation de l'information dans les milieux aquatiques. Le besoin croissant de spécifications telles qu'un débit de données élevé, une portée de liaison maximale atteignable, la sécurité de la transmission, une faible latence, une faible complexité de mise en œuvre et une faible consommation d'énergie ont rendu difficile le déploiement de réseaux de communication efficaces.

L'utilisation des technologies de communications sans fil sous-marines (UWC pour Underwater Wireless Communications) est plus souhaitable que leur équivalent câblé, notamment en raison de leur facilité d'installation. Les trois technologies UWC existantes sont la communication Radiofréquence (RF pour Radio Frequency), acoustique et optique, dont la dernière sera le sujet de cette thèse. Étant donné les différences de propriétés inhérentes aux technologies susmentionnées, leur utilisation peut être affectée par les conditions de l'eau, la présence de la lumière du soleil, les vents, la vie marine, etc. limitant ainsi leur faisabilité dans certains scénarios (voir Fig. 1). Cette thèse s'intéresse à la technologie de communication optique sous-marine sans fil (voir Fig. 2).

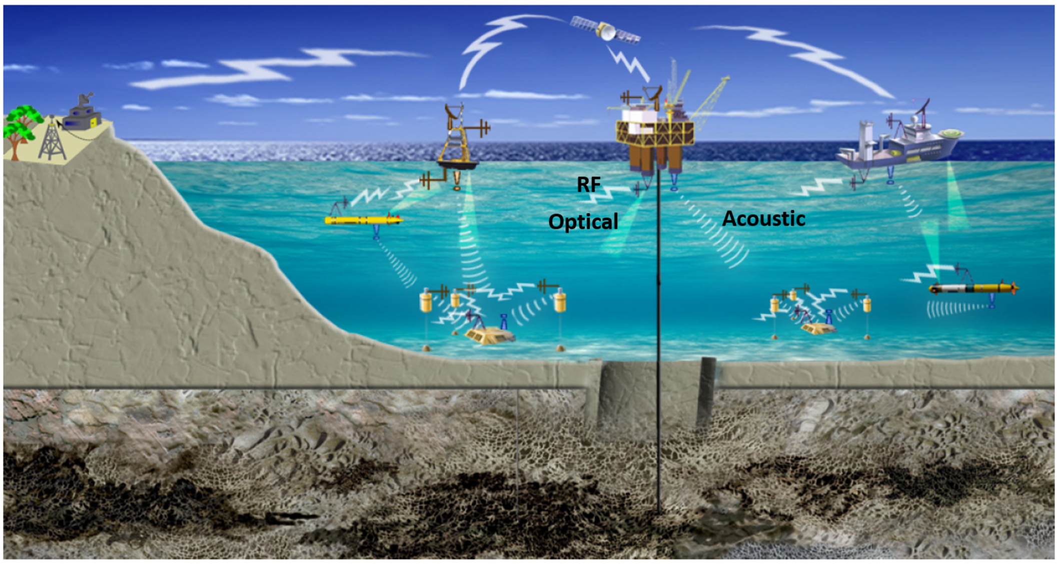

Figure 1: Scénarios de déploiement des différentes technologies de communication sans fil sous-marines.

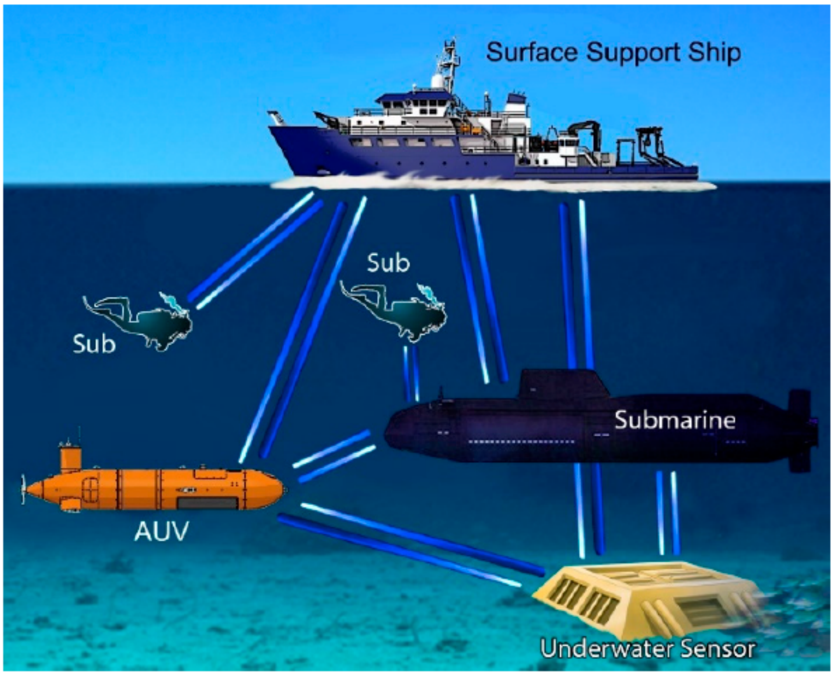

Figure 2: Illustration de la technologie de communication optique sous-marine sans fil pour la collecte et le transfert de données.

Le caractère unique des différents moyens de communication sans fil, terrestres et sous-marins, est très évident dans les communications basées sur les radiofréquences. Le premier bénéficie d'une communication à grande vitesse sur de longues distances, contrairement au second. L'utilisation des communications RF dans l'UWC pour les transmissions à haut débit de données, telles que la diffusion audio et vidéo en temps réel, est limitée à une distance de liaison de 10 m pour une mise en œuvre simple. Cela est dû à la nature très conductrice de l'eau de mer (du fait de sa température et de sa salinité) dans les plages de fréquences de ces applications. Cependant, à des fréquences plus basses (3 Hz à 30 kHz), le niveau d'atténuation du signal RF est très minime et la transmission sur plusieurs kilomètres est possible mais à des débits faibles, avec des équipements (comme l'antenne) encombrants, coûteux et consommant beaucoup d'énergie. Malgré les contraintes de surface des communications RF sous-marines, plusieurs travaux ont exploré sa mise en œuvre et peu d'entre eux avec l'intention de l'améliorer. Dans certains cas, la fréquence MHz a été transmise à l'aide d'ondes RF sur une liaison sous-marine de 100 m. Cependant, cela n'a été possible qu'à une puissance de transmission élevée d'environ 100 watts avec l'utilisation d'antennes avancées et encombrantes. De même, le débit de données dans les communications RF peut être amélioré en utilisant une stratégie MIMO (multiple input multiple output) avec une modulation par déplacement de phase en quadrature (QPSK pour quadrature phase shift keying) pour atteindre 48 kbps sur une liaison sous-marine de 2 km. Il convient de noter que la faculté de propagation de type multicanal (eau-air-sol) des communications RF les rend exploitables pour de nombreuses applications potentielles.

Les communications acoustiques sont la technologie la plus courante pour les UWC, et la plus adaptée à l'établissement de transmissions de données à très longue portée. Cependant, la possibilité d'établir des transmissions à longue portée n'est possible qu'à basse fréquence. En effet, les signaux acoustiques à basse fréquence subissent peu d'atténuation de propagation par rapport aux signaux à haute fréquence. De plus, la communication acoustique dans l'environnement sous-marin est altérée par plusieurs facteurs tels que la latence élevée, la propagation multi-trajet et l'évanouissement. De plus, étant donné la faible largeur de bande des ondes acoustiques, la technologie est limitée à des applications à faible débit de données de l'ordre de quelques kilobits par seconde (kbps). Des recherches approfondies ont été menées au cours des dernières années pour améliorer les performances des communications acoustiques sous-marines. Par exemple, afin d'éliminer la distorsion du signal par trajets multiples, certaines stratégies de compensation des trajets multiples ont été utilisées et le débit a été amélioré. En outre, l'utilisation du multiplexage par répartition en fréquence orthogonale (OFDM pour orthogonal frequency division multiplexing) a permis de réaliser des débits de données élevés sans avoir à ajouter des égalisateurs complexes.

Compte tenu des diverses contraintes susmentionnées des UWC basés sur la RF et l'acoustique, il existe un besoin non négligeable de répondre à la demande croissante d'une technologie UWC efficace et fiable pour les applications à haut débit sur des distances de liaison conséquentes. La technologie de communication optique dans l'UWC, que nous appellerons simplement communication optique sans fil sous-marine (UWOC pour Underwater Wireless Optical Communications), constitue une alternative prometteuse avec un haut débit de transmission de données (jusqu'à Gbps) et une efficacité énergétique bien garantis sur des distances de liaison courtes à modérées, principalement en raison de sa grande largeur de bande disponible. L'UWOC offre également une faible complexité de mise en œuvre et une faible latence de transmission. On peut facilement constater l'intérêt de l'UWOC par rapport aux autres technologies UWC, en particulier pour les scénarios d'application à courte et moyenne portée, à haut débit et multi-utilisateurs. La Fig. 3 est une illustration de la liaison UWOC, où LD est diodes laser et SiPM est photomultiplicateur en silicium.

Une poignée de systèmes UWOC présentant divers intérêts d'application sont disponibles dans le commerce ou sous forme de prototypes. Par exemple, Shimadzu Corporation a mis au point le MC100, un modem UWOC, installé sur des drones sous-marins et capable de réaliser un Wi-Fi optique sous-marin à des débits de données supérieurs à 95 Mbps sur une distance de plus de 10 mètres. Un autre modem optique, LUMA X d'Hydromea, est un modem optique sans fil à grande vitesse et à longue portée, capable d'atteindre un débit de 10 Mbps sur une distance de plus de 50 m. De même, le BlueComm 200 de Sonardyne est un autre système UWOC commercialisé, capable d'un taux de transmission de données de 10 Mbps jusqu'à 150 m, même en cas de forte luminosité ambiante.

Plusieurs prototypes de systèmes UWOC qui ont été développés et testés sont sur la voie de la commercialisation. Plusieurs modems optiques existent, tels que le module modem op-

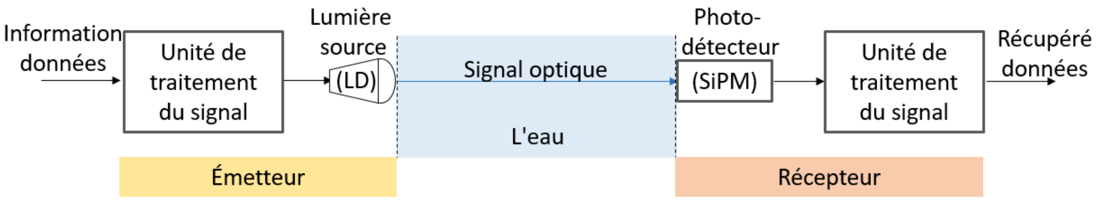

Figure 3: Le schéma fonctionnel de la liaison de communication UWOC.

tique (OMM) de UON technologies (voir Fig. 4). L'un des premiers prototypes est le modem AquaOptical développé par des chercheurs du MIT et capable de transmettre des Mbps de données sur quelques mètres. Une version améliorée ultérieurement, appelée AquaOptical II, permet d'atteindre des distances de transmission plus importantes avec des débits de données plus élevés. De même, un modem optique basé sur un SiPM très sensible, a été développé et testé par le laboratoire de recherche de l'Ifremer (Institut français de recherche pour l'exploitation de la mer) et de l'Institut Fresnel avec le soutien de la société Osean SAS Co. En outre, une démonstration d'un système UWOC compact, de faible puissance et de faible coût, appelé Aqua-Fi (voir Fig. 5) dans le domaine des applications Internet a été réalisée. Il exploite les caractéristiques d'une diode électroluminescente (LED pour Light Emitting Diode) ou d'un laser pour réaliser une communication bidirectionnelle de moyenne à longue portée.

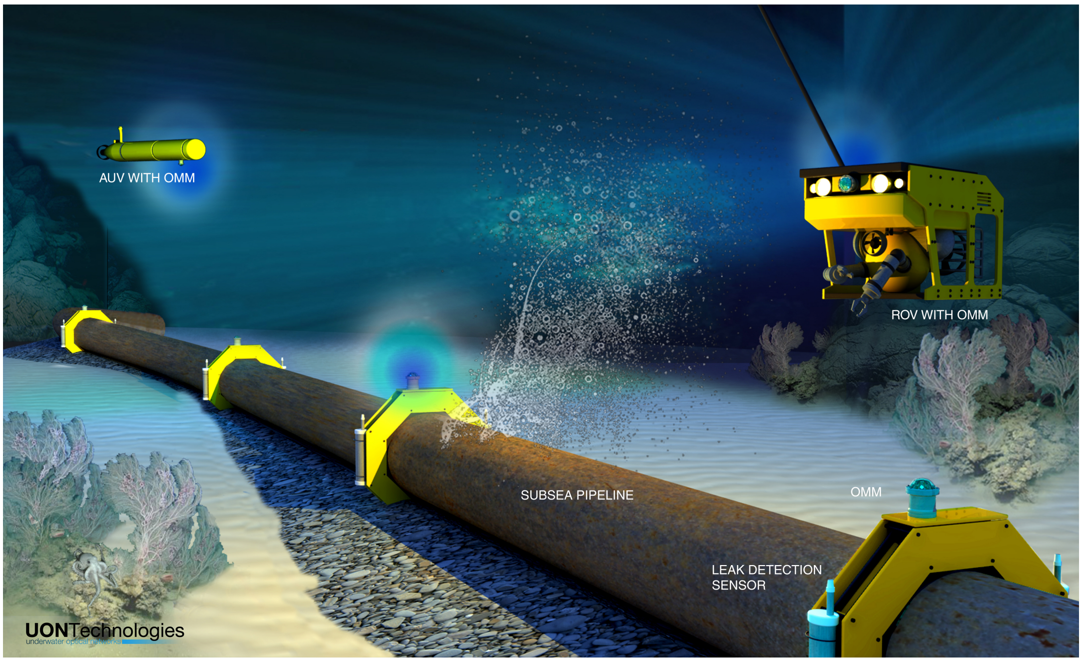

Figure 4: Utilisation de OMM des technologies UON pour la surveillance des pipelines sous-marines.

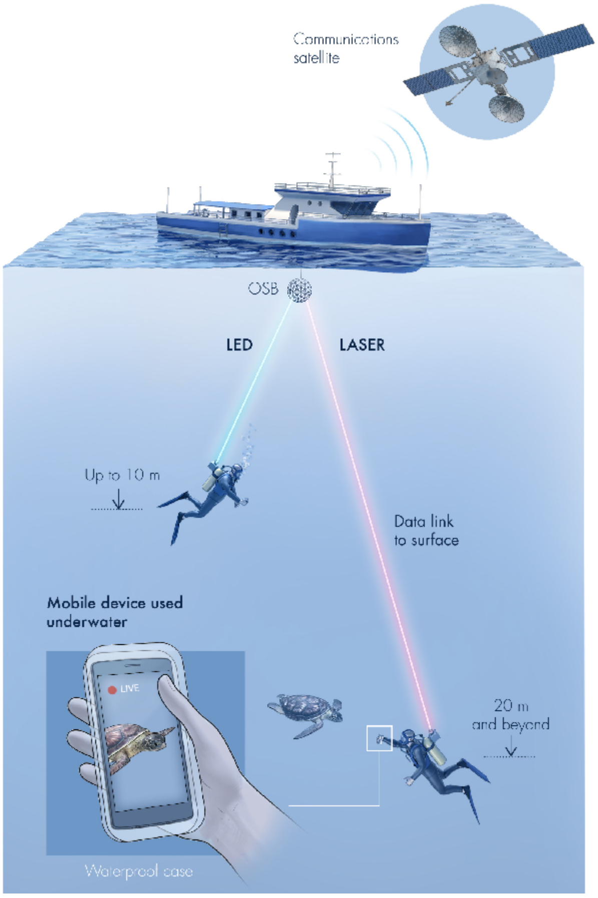

Figure 5: Architecture d'un système UWOC, l'Aqua-Fi.

Malgré les nombreux avantages de l'UWOC, son efficacité est compromise par l'absorption et la diffusion des particules dans l'eau, le bruit de fond solaire, les turbulences océaniques, le désalignement des liaisons émetteur (Tx pour transmitter)-récepteur (Rx pour receiver), les obstructions physiques, etc. Plusieurs travaux ont été menés pour évaluer les performances des liaisons UWOC et éventuellement les améliorer en tenant compte de certains des facteurs de dégradation mentionnés ci-dessus. Par exemple, une étude théorique et expérimentale a été menée sur l'effet du déplacement de la position du Rx et de son angle d'inclinaison par rapport à l'axe optique principal sur le signal détecté. L'impact du bruit solaire sur une liaison UWOC parfaitement alignée a été étudié. De plus, pour une liaison UWOC verticale, l'effet de la turbulence a été caractérisé et étudié comme ayant des puissances variables à travers les couches avec une épaisseur uniforme du canal de transmission.

Comme nous l'avons souligné précédemment, les demandes croissantes de la plupart des applications sous-marines pour des transmissions à haut débit de données sur des distances modérées ont fait des UWOC un choix prometteur par rapport aux communications acoustiques conventionnelles. Cependant, le canal aquatique et certaines exigences de mise en œuvre constituent un obstacle au déploiement des liaisons UWOC et, par conséquent, à leurs performances. Parmi

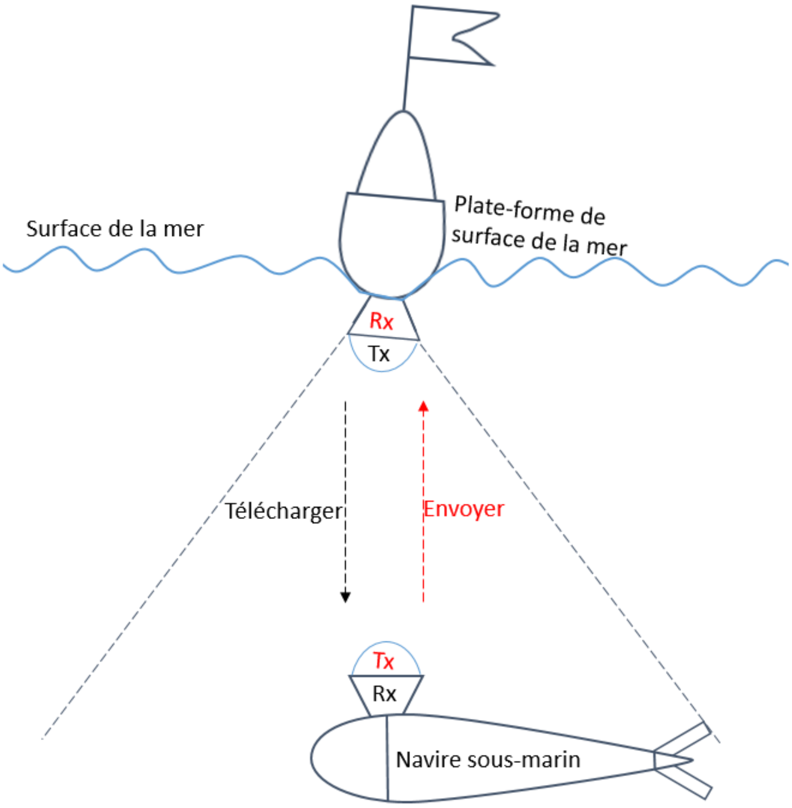

Figure 6: Illustration de la liaison verticale UWOC considérée dans le chapitre 5.

les principaux défis de mise en œuvre figure le désalignement entre la Tx et la Rx, en particulier dans les cas où l'utilisation d'un système de tracking pour le pointage et l'acquisition du signal optique augmenterait la complexité et le coût de la mise en œuvre. En plus de ces erreurs de pointage (PE pour Pointing Errors), la turbulence océanique peut dégrader davantage les performances des liaisons UWOC en provoquant une fluctuation aléatoire de l'intensité du signal optique reçu. Il devient donc nécessaire d'étudier l'effet de ces facteurs sur la qualité du signal transmis afin de s'assurer de la fiabilité du signal reçu et éventuellement d'optimiser le lien de communication. Par conséquent, cette thèse est motivée par la volonté de fournir un aperçu plus clair de la caractérisation d'un canal variant dans le temps en évaluant la performance d'un système UWOC typique soumis à ces contraintes pratiques dans le but de favoriser la proposition de schémas d'atténuation efficaces.

Notre objectif dans cette thèse est d'étudier les impacts des PEs et de la turbulence océanique sur la performance des liens UWOC. Plus spécifiquement dans cette thèse, dans le Chapitre 1 nous présentons une introduction aux systèmes UWCs. Nous discutons des caractéristiques des trois technologies UWC existantes et soulignons leurs différents scénarios d'application idéaux. Nous nous focalisons ensuite sur l'UWOC et donnons quelques-uns de ses systèmes et prototypes commercialisés existants. Nous donnons ensuite la motivation et les objectifs de cette thèse. Enfin, nous décrivons le travail effectué et les contributions apportées dans cette thèse.

Dans le Chapitre 2, nous présentons l'état de l'art de la recherche sur l'UWOC. Nous présentons une vue d'ensemble de la technologie et discutons, à travers des publications pertinentes, des composants qui composent le système, des performances obtenues à ce jour et des limitations du système UWOC. Nous mettons surtout l'accent sur les sujets qui sont d'intérêt dans cette thèse, tels que le choix des émetteurs-récepteurs optoélectroniques, les modèles de canaux de transmission et les défis pratiques.

Dans le Chapitre 3, nous étudions et soulignons le potentiel de l'utilisation des SiPMs dans les applications UWOC. Nous présentons, avec suffisamment de détails, la structure, les principes de fonctionnement et les limites des Rx basés sur les SiPMs. Notre discussion met en évidence les explications des caractéristiques inhérentes au SiPM, notamment sa grande sensibilité, même à une intensité optique très faible. En outre, nous effectuons des simulations pour démontrer les performances de la liaison UWOC en utilisant un SiPM, notamment en ce qui concerne l'augmentation de la portée de transmission.

Dans le Chapitre 4, nous étudions la littérature existante sur l'impact des désalignements et des turbulences océaniques sur les liaisons UWOC et certains des schémas d'atténuation proposés. Ce chapitre est le résultat de notre intérêt à étudier dans cette thèse les effets des erreurs de pointage et de la turbulence sur la performance d'une liaison UWOC. Nous passons en revue les différentes configurations de liens et les modèles de canaux de transmission considérés par les différents travaux pertinents. Nous nous concentrerons sur les ouvrages où des considérations réalistes ont été données dans le développement du système UWOC, en particulier dans les particularités des faisceaux à base de LED et de diodes laser (LD) se propageant dans le canal aquatique. L'objectif est de comprendre comment certains paramètres du système pourraient avoir un impact sur les performances d'une liaison soumise à des désalignements et à des turbulences.

Dans le Chapitre 5, nous étudions l'effet du désalignement de la liaison, causé par le vent à la surface de la mer et les courants sous-marins sur la performance de la liaison verticale UWOC (voir Fig. 6). Tout d'abord, nous développons un modèle analytique du désalignement de la liaison pour une configuration Tx à base de LED, en tenant compte des désalignements angulaires et des déplacements de Tx et Rx, puis nous étudions son impact sur la performance de la liaison UWOC en termes de probabilité de blocage. Notre étude basée sur les simulations considère deux scénarios : les communications en liaison descendante et en liaison montante, afin de couvrir une transmission bidirectionnelle. Nous montrons également l'intérêt de sélectionner de manière appropriée certains paramètres du système afin de minimiser l'effet du désalignement de la liaison. Nos résultats permettent de mieux comprendre la conception des systèmes UWOC, car ils analysent le choix des paramètres du système pour une communication fiable, compte tenu de certains défis pratiques.

Dans le Chapitre 6, nous étudions l'effet du désalignement et de la turbulence océanique sur une liaison UWOC verticale basée sur le LD (voir Fig. 7). Nous modélisons avec précision l'impact de la turbulence sur une liaison verticale inhomogène en considérant la méthode de moyennage

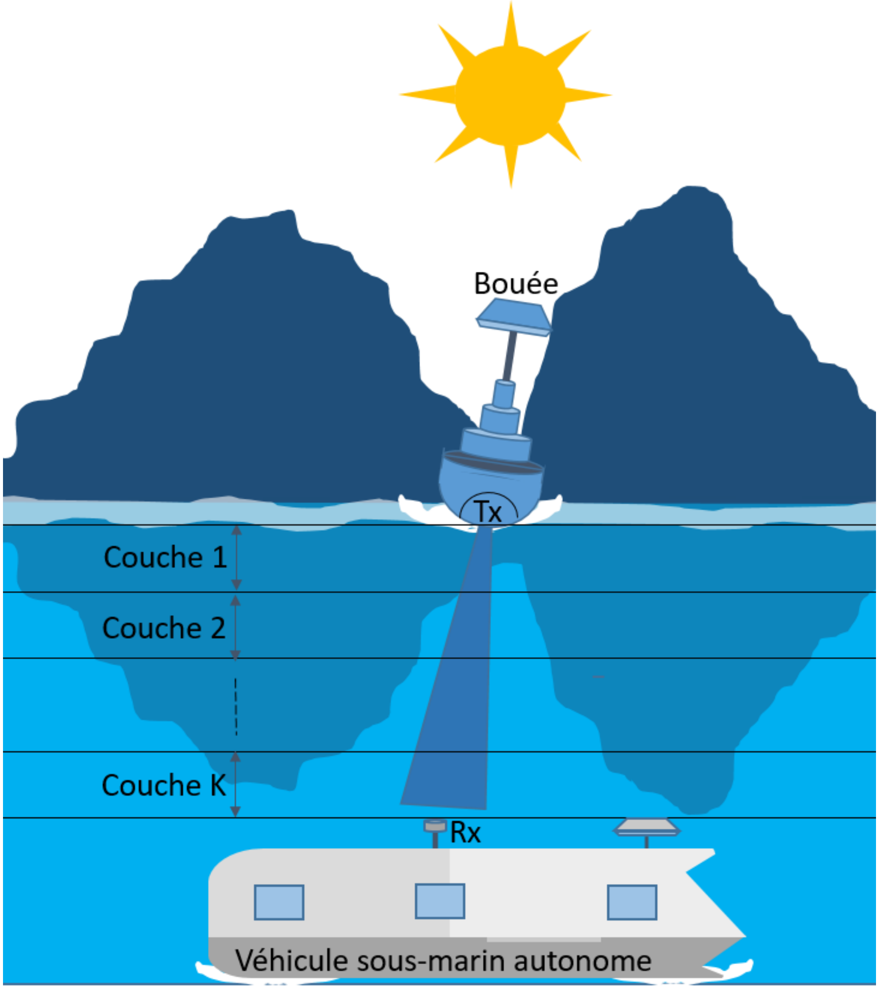

Figure 7: Illustration de la liaison verticale UWOC considérée dans le chapitre 6.

d'ouverture, et nous prenons en compte des valeurs réalistes pour son évaluation. Nous développons un modèle statistique pour tous les effets sur le canal et nous dérivons une expression compactes de Pout pour l'évaluation de la performance du lien. Enfin, nous montrons également l'intérêt d'une sélection appropriée des paramètres du système pour atténuer l'effet négatif du désalignement et de la turbulence.

Dans le Chapitre 7, nous démontrons expérimentalement la faisabilité de l'utilisation d'un système UWOC avec un Rx basé sur SiPM (voir Fig. 8). Nous décrivons le dispositif expérimental que nous avons développé, ainsi que les différents composants électroniques et optiques utilisés. Nous discutons les points les plus intéressants et présentons quelques résultats expérimentaux pour valider notre travail sur la liaison UWOC.

Enfin, dans le Chapitre 8, nous concluons notre travail dans cette thèse, et donnons quelques perspectives intéressantes pour les travaux futurs.

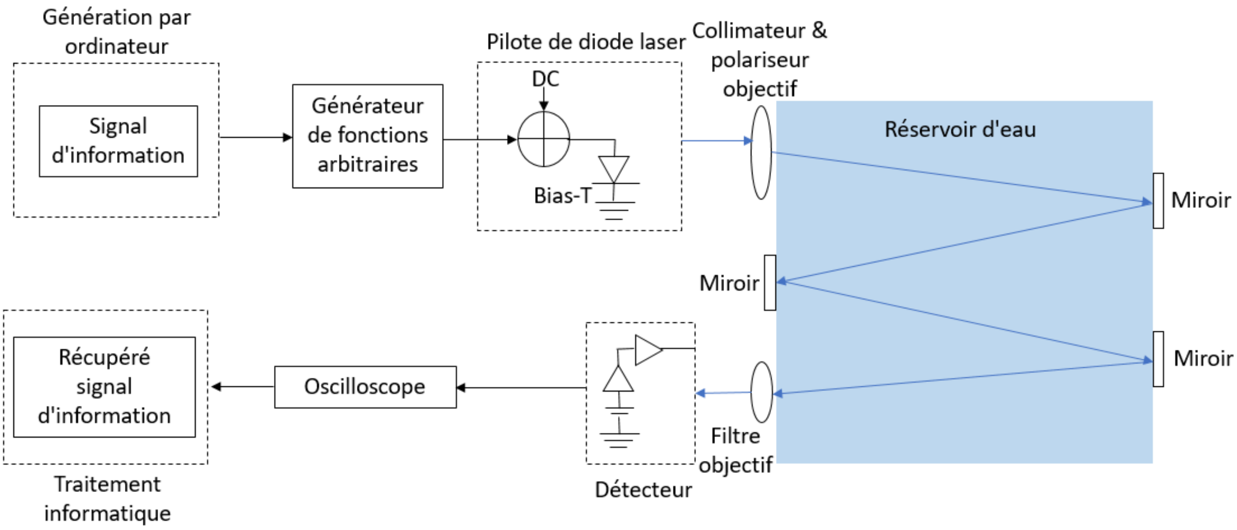

Figure 8: Configuration expérimentale pour les mesures de communication optique sans fil sous-marine dans le chapitre 7.

Les contributions majeures réalisées dans cette thèse sont les suivantes;

- Modélisation d'un canal UWOC vertical en termes de désalignement angulaire et de déplacement de position à la fois du côté Tx et Rx. La modélisation comprend un modèle dynamique qui prend en compte l'effet réaliste de la vitesse du vent sur la surface de la mer, affectant ainsi tout vaisseau à la surface de la mer abritant un émetteur-récepteur. Tout cela a permis de dériver des distributions statistiques du canal global, favorisant ainsi la modélisation précise de la dégradation du signal.

- Modélisation statistique précise de la turbulence océanique pour un lien de transmission vertical inhomogène. L'effet du moyennage d'ouverture au Rx a également été pris en compte, ce qui, à notre connaissance, n'a pas été considéré jusqu'à présent dans la littérature sur les liaisons verticales.

- Évaluation de l'impact du bruit de fond des radiations solaires sur la conception des liaisons optiques, en se basant spécifiquement sur les paramètres du système.

- Développement d'une expression compacte pour l'évaluation de la performance en terme de probabilité de blocage, pour une liaison verticale UWOC soumise à des erreurs de pointage, à la turbulence océanique et au bruit de fond solaire. Cela permet de réduire le temps de calcul des simulations et d'analyser facilement l'impact de certains paramètres sur la performance de la liaison.

- Évaluation de la performance de la probabilité de blocage des liaisons UWOC pour différentes configurations de désalignement et de conditions de turbulence océanique.

- L'étude et la mise en œuvre de l'optimisation de la liaison UWOC pour un FoV limité de Rx, avec un photo-détecteur (PD) à haute sensibilité, qui, à notre connaissance, n'a pas été considéré dans la littérature jusqu'à présent. Nous avons démontré et analysé l'importance d'une sélection appropriée des paramètres de liaison pour l'amélioration de la performance de la liaison dans des conditions de dégradation.

- L'étude expérimentale de la faisabilité du déploiement d'une liaison UWOC et l'évaluation de la limitation de la réponse en fréquence du canal.

Table of contents

Chapter 1

General Introduction

Contents

1.1 Underwater wireless communications

The water environment occupies a wide majority of the earth's surface, so it is not surprising that it experiences rapid growth in technology. Most significant are communication technologies for various applications such as ocean monitoring, data collection and transfer between a sea surface vessel and an underwater sensor, pipeline fault detection and maintenance, research, exploration and exploitation of natural resources, etc. These activities have put a high demand for improved and reliable communication techniques that take into account the peculiarities of the information propagation channel through the aquatic media. The growing need for features such as high data rate, long achievable link range, transmission security, low latency, low implementation complexity, and low energy consumption have made the deployment of efficient communication networks challenging.

The use of underwater wireless communication (UWC) technologies compared to the wired counterparts are more desirable in particular due to their flexibility in deployment. Three existing UWC technologies are radio frequency (RF), acoustic and optical communication (see Fig. 1.1)

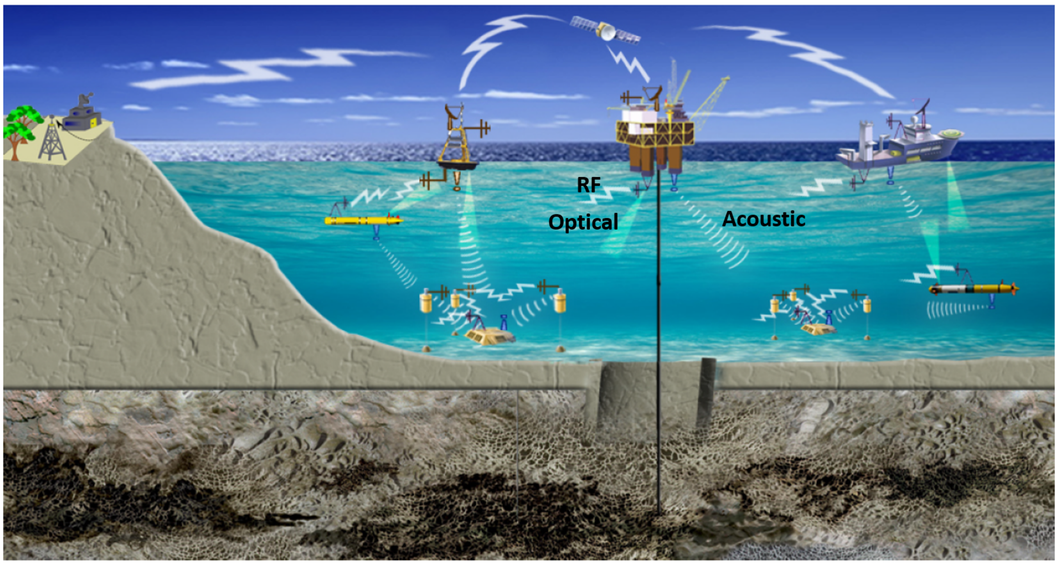

Figure 1.1: Deployment scenarios of the different underwater wireless communication technologies (reproduced from [2]).

[1, 2, 3, 4], with the latter being of interest in this thesis (see Fig. 1.2). Given the inherent property difference in the aforementioned technologies, their use can be affected by the water turbidity, presence of sunlight, marine life, etc.; hence, limiting their feasibility in certain scenarios. This necessitates the relevance in having a broad knowledge of the different UWC technologies in order to choose the most appropriate for a given application. Therefore, below is a brief discourse of these UWC technologies with their peculiar potentials and drawbacks, hence giving insight into their suitable scenario of application. Also, this aids especially in justifying the optical communication system applied to the work in this thesis.

1.1.1 Underwater RF communications

The uniqueness in different wireless communication media; especially through the atmosphere or water, is very evident in RF-based communications. The former enjoys high-speed communication over long distances in large contrast to the latter. The use of RF communications in UWC for high data rate transmissions, such as real-time audio and video streaming, is limited to a typical link range of 10 m with simple system requirements [2]. This is due to the very high conductive nature of seawater (from its temperature and salinity) at the frequency ranges of such applications. However, at lower frequencies (3 Hz to 30 kHz), the level of RF signal attenuation is minimal and transmission over several kilometers is possible but at low data rates, with equipment (such as the antenna) that is bulky, expensive and consumes much power [2].

Despite the surface constraints of underwater RF communications, several works have explored their implementation and a few of them with the intent to improve their performance [5, 6, 7]. A MHz transmission using RF waves was achieved in [6] over an underwater link of 100 m.

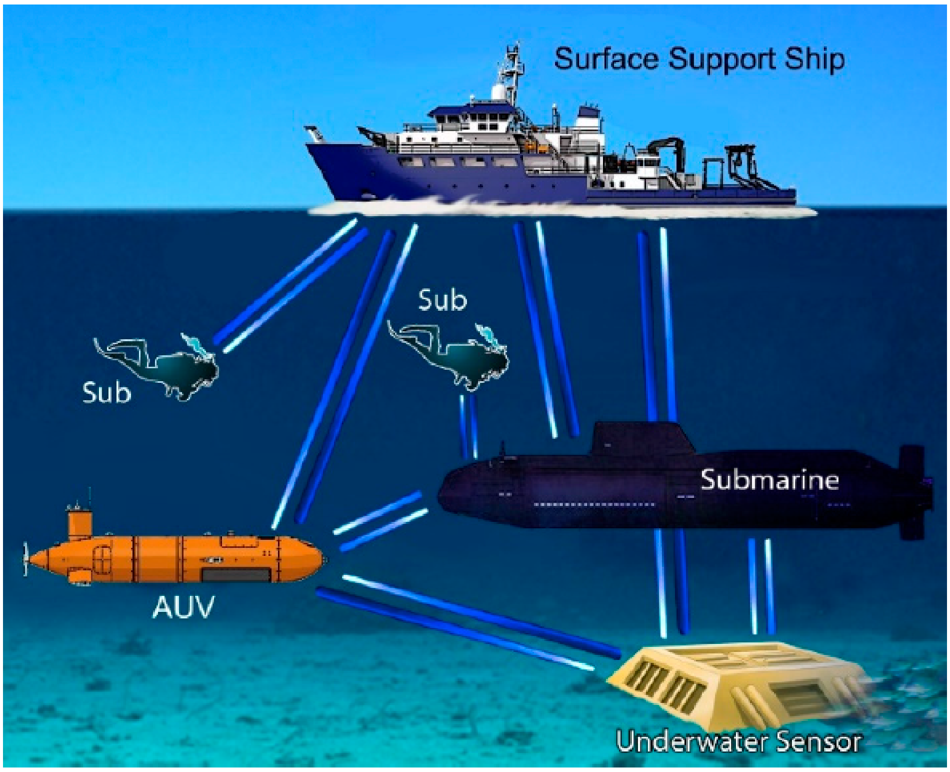

Figure 1.2: Illustration of the optical underwater wireless communication technology for data collection and transfer (reproduced from [4]).

However, this was only possible at a high transmission power of about hundreds of Watts with the use of advanced and bulky antennas. Aiming to improve the data rate in RF communications, [7] reported a multiple-input multiple-output (MIMO) configuration with quadrature phase shift keying (QPSK) modulation that could achieve 48 kilobits per second (kbps) over 2 km underwater link. It is worthy of note that the various scenarios for RF signal propagation (such as air-to-water or water-to-ground), makes it feasible for numerous potential applications.

1.1.2 Underwater acoustic communications

Acoustic communications are the most common technology for UWC, and the most suited for establishing very long-range data transmissions. However, the possibility of long-range transmissions comes at low frequencies, which for about 1000 km is within the frequency band of less than a kHz [8]. The acoustic signal at low frequencies experiences low channel attenuation compared to signals at high frequencies because of the very limited bandwidth of the underwater acoustic channel [9, 8, 2]. Furthermore, underwater acoustic communication is impaired by several factors such as; low speed, high latency, multi-path propagation and fading. Also, given the low bandwidth of acoustic waves, the technology is limited to low data rate applications of kbps typically [10].

Extensive research has been carried out to improve the performance of underwater acoustic communications [11, 12, 13]. In [11], with an intent to remove the multipath signal distortion, some multipath compensation strategies were proposed. Also, the use of orthogonal frequency division multiplexing (OFDM) has aided in realizing high data rates forgoing the addition of complex equalizers [12, 13].

1.1.3 Underwater optical communications

Given the various afore-discussed constraints of RF- and acoustic-based UWCs, there is an unsubstitutable need to meet the growing demand for an efficient and reliable UWC technology for high-speed applications over considerable link ranges. Optical-based UWC, which will be simply referred to as underwater wireless optical communication (UWOC), comes as a promising complementary technology [14, 15, 16] over short-to-moderate link ranges with well-secured high data rate transmission (up to Gigabits per second (Gbps)) [17] mainly due to its large available bandwidth. UWOC also offers low implementation complexity, low transmission latency, and high energy efficiency.

Despite the numerous advantages of UWOC, its efficiency is challenged by absorption and scattering from particles in the water, solar background noise, oceanic turbulence, transmitter (Tx)-to-receiver (Rx) link misalignment, physical obstructions, etc. Several works have been carried out to evaluate the performance of the UWOC link to possibly improve it given some of the above degrading factors. For instance, in [18], a theoretical and experimental study was carried out for the effect of displacement in the Rx position and its inclination angle with respect to the main optical axis on the detected signal. The impact of solar noise on a perfectly aligned UWOC link was investigated in [19]. Also, for a vertical UWOC link, [20] characterised and studied the effect of turbulence on the transmission channel, as having varying strengths across layers with uniform thickness.

It can easily be deduced from the discussions so far the interest of UWOC compared to other UWC technologies, especially for short-to-moderate range application scenarios. A brief comparison of these UWC technologies is provided in Table 1.1. In the following section, we will discuss some commercialized UWOC systems and prototypes.

1.1.4 Existing UWOC systems and prototypes

Some handful of UWOC systems with various application interests are available commercially or as prototypes. For instance, Shimadzu Corporation developed MC100, an UWOC modem, installed on underwater drones with the capability of achieving data rates above 95 Megabits per second (Mbps) through more than 10 m [21]. Another optical modem, LUMA X from Hydromea, is capable of attaining up to 10 Mbps across a range of more than 50 m [22]. Also, the BlueComm 200 from Sonardyne can achieve a data rate of 10 Mbps operating up to 150 m[23].

Table 1.1: Comparison of underwater wireless communication technologies (reproduced from [4]).

Parameters	RF	Acoustic	Optical
Data rate	~ hundreds of kbps	~ kbps	tens to hundreds of Mbps
Bandwidth	~ MHz	≈ 100 kHz	10-150 MHz
Range	up to ≈ 10 m	hundreds of kms	up to 100 m
Tx power	up to hundred of Watts	tens of Watts	few Watts
Attenuation	Frequency and conductivity dependent (3.5-5 dB/m)	Distance and frequency dependent (0.1-4 dB/Km)	0.39 dB/m (ocean) 11 dB/m (turbid)

On the road to commercialization, several prototypes of UWOC systems have been developed and tested. Several optical modems are in existence, such as the optical modem module of UON technologies (see Fig. 1.3) [24]. One of the earlier prototypes is the AquaOptical modem developed by MIT researchers and capable of transmitting Mbps of data across a few meters [25]. A later improved version, called AquaOptical II achieved higher transmission ranges with higher data rates [26]. Also, an optical modem based on the highly sensitive silicon photomultiplier (SiPM), was developed and tested by Ifremer (French Research Institute for Exploitation of the Sea) and Institut Fresnel research lab with the support of Osean SAS Co., a French instrumentation company [27]. In the domain of internet applications, [28] demonstrated in a lab environment, a compact, low power, and low cost UWOC system, called Aqua-Fi (see Fig. 1.4). It exploits the features of either a light-emitting diode (LED) or laser diode (LD) to achieve bidirectional moderate-to-long range communication.

1.2 Thesis motivation and objectives

As earlier emphasized, the increasing demands of most underwater applications for high data rate transmission over moderate distances have made UWOCs a promising choice, compared with the conventional acoustic communications. However, the aquatic channel and some implementation requirements challenge the deployment of UWOC links and subsequently, its performance. Among the major implementation challenges is the misalignment between the Tx and the Rx, especially in cases where the use of a tracking system for pointing and acquisition of the optical signal would increase implementation complexity and cost. In addition to these pointing errors (PEs), oceanic turbulence can further degrade the performance of UWOC links by causing random fluctuation of the received optical signal intensity. Thus, it becomes necessary to investigate the effect of these factors on the transmitted signal quality so as to ascertain the reliability of the received signal and possibly optimize the communication link. Hence, this thesis is motivated to

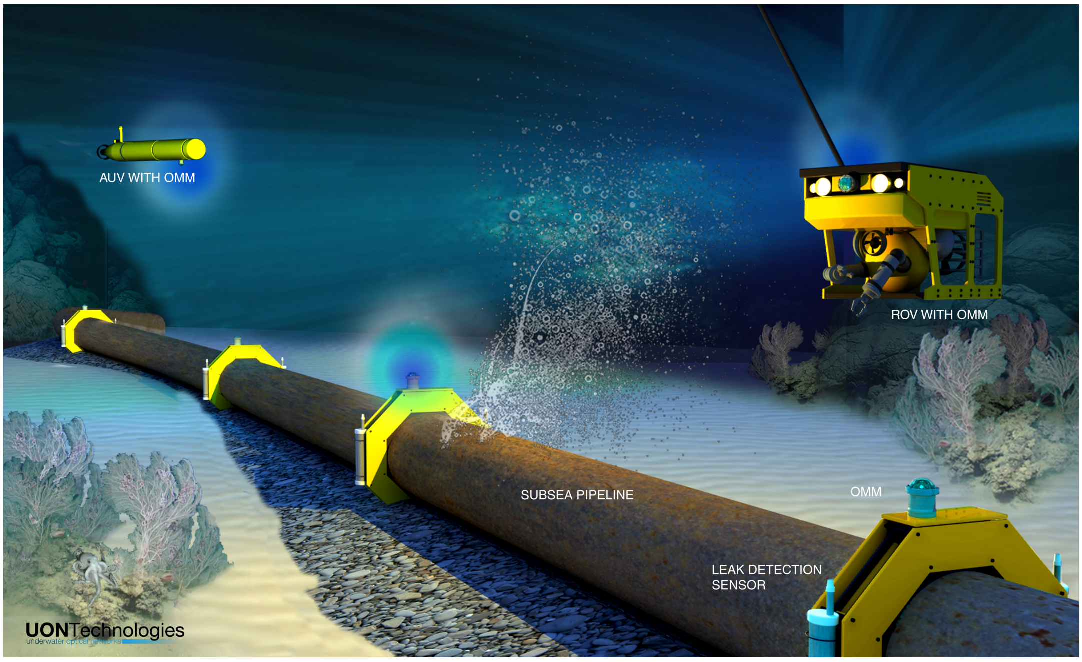

Figure 1.3: Using optical modem module (OMM) of UON technologies for monitoring underwater pipelines (reproduced from [24]).

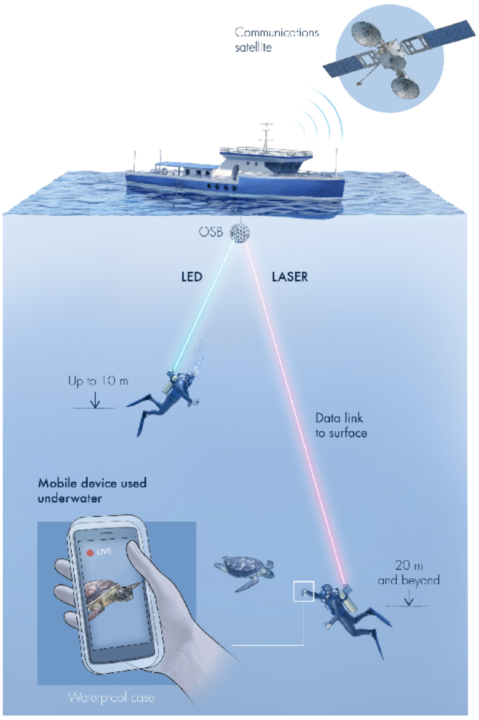

Figure 1.4: Architecture of an UWOC system, the Aqua-Fi (reproduced from [28]).

proffer clearer insights into the characterization of a time-varying channel by evaluating the performance of a typical UWOC system subject to these practical constraints with the intent to foster the proposing of efficient mitigation schemes.

Our objective in this thesis is to study the impacts of PEs and oceanic turbulence on the performance of UWOC links. More specifically, we focus on accurate mathematical, and statistical channel modeling, in particular, for the case of a vertical transmission link, e.g., between a surface platform and an underwater counterpart. There, PEs are modelled by taking into consideration the wind at the sea surface and Rx angular misalignments, in particular. Then we analyze the impact of PEs and turbulence on the link performance based on the developed channel model. In addition, we consider the appropriate selection of the Tx/Rx parameters in order to optimize the link performance based on the criteria of the outage probability.

All through this work, we consider a highly sensitive photodetector (PD), i.e., an SiPM, at the receiver in order to increase the operational range. Lastly, some preliminary experimental works have been carried out to assess the practical issues of establishing an UWOC link using a dedicated laboratory testbed. The presented work fosters the UWOC system design and research towards practical considerations of link deployment ensuring reliable communications.

In the following section, we give the outline of this thesis manuscript.

1.2.1 Thesis outline

This dissertation is organized into eight chapters, including this Introduction as **Chapter 1**, the rest are described in the following:

In **Chapter 2**, we provide the state of the art of UWOC research. We present an overview of the technology and discuss the components that make up the system, the achieved performance so far and limitations of the UWOC systems. We highlight in particular, the topics that are of interest in this thesis, such as the choice of optoelectronic components, channel model, and practical challenges.

In **Chapter 3**, we present the potentials of using SiPMs in UWOC applications. We present an adequate detail of the structure, working principles, and limitations of SiPM based Rxs. Our discourse showcases the reasons for the inherent features of the SiPM, especially its high sensitivity to very low-level optical intensity. Furthermore, we carry out some simulation-based studies to demonstrate the UWOC link performance while using an SiPM.

In **Chapter 4**, we study the existing literature on the impact of misalignments and oceanic turbulence on the performance of an UWOC link and some of the proposed mitigation schemes. This chapter is as a result of our interest in this thesis to investigate the effects of PEs and turbulence on the performance of UWOC links. We review the different link configurations and channel models considered by several relevant works. Our focus will be on the realistic considerations especially regarding LED and LD-based beam propagating through the aquatic channel. This is with the intent to understand how some system parameters could impact the link performance subject to both misalignments and turbulence.

In **Chapter 5**, we study the effect of link misalignment caused by wind on the sea surface and underwater currents on the UWOC vertical link performance. Firstly, we develop an analytical model of the link misalignment for an LED-based Tx configuration, considering the Tx and Rx angular misalignments and displacements, and then study their impact on the link performance in terms of the link outage probability. Our simulation-based study considers two scenarios of downlink and uplink communications in order to cover the study for bidirectional transmission. We further show the interest in appropriately selecting some system parameters in order to minimize the effect of link misalignment. Our results are insightful in the design of UWOC systems, as they analyze the choice of system parameters for reliable communication taking into account practical challenges.

In **Chapter 6**, we investigate the effect of both misalignment and oceanic turbulence on a vertical LD-based UWOC link. We accurately model the impact of turbulence on a vertical inhomogeneous link while considering aperture averaging, and take into account realistic values for its evaluation. We develop a statistical model for the entire effect on the channel and further derive a closed-form expression of outage probability for the evaluation of the link performance. Lastly, we show the interest in the appropriate selection of system parameters to mitigate the adverse effects of misalignment and turbulence.

In **Chapter 7**, we experimentally demonstrate the feasibility of implementing an UWOC system. We give a description of the experimental setup we developed, and the different electronic and optical components used therein. We present some experimental results to assess the performance of an UWOC link.

Finally, in **Chapter 8**, we conclude our work in this thesis and give some perspectives for future work.

1.2.2 Author's contributions

The major contributions of the author in this thesis are summarized in the following;

- Modelling of a vertical-UWOC channel in terms of angular misalignment and position displacement at both the Tx and the Rx side: The resulting dynamic model considers the realistic effect of wind speed on the sea surface, hence affecting any considered sea-surface vessel housing a transceiver. All this gave to the derivation of statistical distributions of the overall channel, thus fostering the accurate modeling of the signal degradation.

- Accurate statistical modelling of oceanic turbulence for an inhomogeneous vertical transmission link, taking into account the effect of aperture averaging at the Rx, which to the best of our knowledge, have not been considered in vertical links literature so far.

- Evaluation of the impact of background noise from solar radiations on the optical link design.
- Development of a closed-form expression for the outage probability performance for a vertical UWOC link subject to PEs, oceanic turbulence, and solar noise. This aids to reduce the computation time from simulations, and also easily analyze the impact some parameters have on the link performance.
- Investigation of UWOC link optimization for a limited Rx FoV with a high-sensitivity PD, and the resulting performance improvement, which to the best of our knowledge, has not been considered in the literature thus far.
- Experimental investigation of the feasibility of deploying an UWOC link, and evaluating the frequency response of the transmission system.

1.2.3 Author's publications

1. I. C. Ijeh, M. A. Khalighi, S. Hranilovic, "Parameter Optimization for an Underwater Optical Wireless Vertical Link Subject to Link Misalignments," *IEEE Journal of Oceanic Engineering*, pp. 1–14, Early Access, 2021.
2. I. C. Ijeh, M. A. Khalighi, M. Elamassie, S. Hranilovic, M. Uysal, "Parameter Selection for a Vertical Underwater Wireless Optical Link Subject to Oceanic Turbulence and Pointing Errors," (in preparation).

Chapter 2

Underwater wireless optical communications

Contents

2.1 Introduction

In our previous discussion, we have established the potentials and the application interests of UWOC technology, such as high data rate transmission at moderate range, compared to the conventional acoustic communications. An UWOC link basically consists of a Tx unit, the aquatic channel and an Rx unit. The general block diagram of the communication link is shown in Fig. 2.1.

At the Tx, the information data are modulated, then converted to an optical signal using the optical source, typically an LED. Assuming the use of intensity modulation with direct detection (IM/DD) scheme, the output light intensity from the optical source is varied according to the modulated signal, and at the Rx, direct detection is used for the recovery of the originally sent signal.

Following the transmission of the optical signal through the aquatic channel, it is susceptible to attenuation due to absorption and scattering, turbulence, pointing errors, background noise, and even physical obstructions. Indeed, accurate modelling of such degrading factors is necessary for efficiently evaluating the UWOC system performance.

At the Rx, which could be equipped with a lens for focusing the received signal, the optical signal is converted by a PD to an electrical signal. Afterwards, demodulation is carried out to recover the original information. Given the channel attenuation, ultra-sensitive PDs could be used to improve the transmission range of a signal.

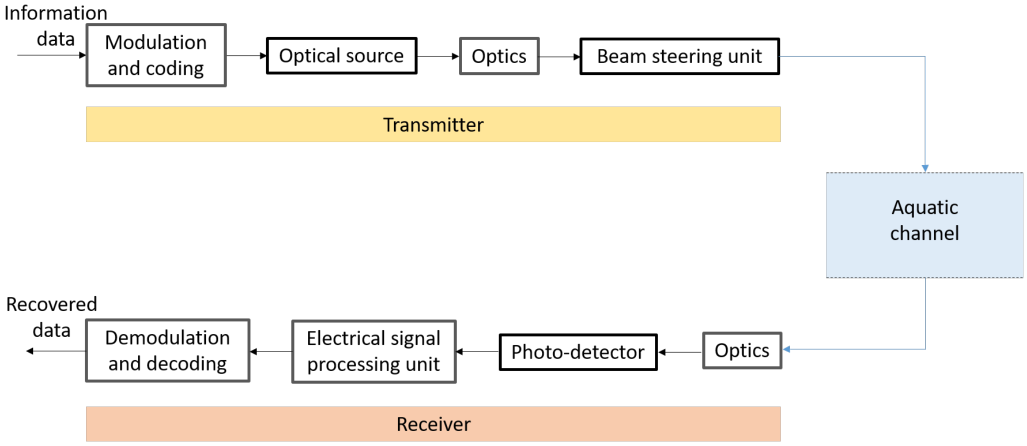

Figure 2.1: The block diagram of the UWOC communication system, reproduced from [1].

Further in this chapter, we will discuss more on the Tx, channel, and Rx of the UWOC system mentioned above. In Section 2.2 we present the concept of some commonly-used modulation schemes. The details of some optical sources at the Tx are given in 2.3. In Section 2.4, we discuss the Rx designs in UWOC systems in relation to the choice of PDs. Then, we study the possible channel models, and some existing practical challenges in Sections 2.5 and 2.6 respectively. Lastly, Section 2.7 concludes this chapter.

2.2 Signal modulation

The choice of signal modulation affects the power consumption, rate, reliability, and range of the data transmission. Hence it is necessary to consider the UWOC system design requirements and application in determining the choice of modulation scheme. The most widely used scheme is the IM/DD, due to its low implementation simplicity [3, 1]. This modulation type is based on the variations in the intensity of the light source, which for a non-coherent source such as the LED, is the only choice [29].

Signal modulation can be classified into two types: single-carrier modulation (SCM) and multi-carrier modulation (MCM). The SCM uses all the available bandwidth to transmit signals, while MCM splits the availabe bandwidth into multiple sub-carriers and the signals are transmitted along them [30, 29]. Our focus on this thesis is on the most commonly used SCM technique, the on-off keying (OOK). Briefly discussed below is the OOK and some other common SCM techniques.

2.2.1 OOK

The OOK is the most used technique due to its simplicity. In this scheme, transmitted bits (symbols) "1" and "0" are associated with two optical powers, $P_{\text{On,OOK}}$ and $P_{\text{Off,OOK}}$ respectively (where $P_{\text{On,OOK}} > P_{\text{Off,OOK}}$). The average transmit power of the OOK system $P_{\text{avg,OOk}} = (P_{\text{On,OOK}} + P_{\text{Off,OOK}})/2$, and the bandwidth (BW) BW_{OOK} is equal to the bit rate R_b. OOK is characterized by rectangular optical pulses with varying duty cycles denoted by γ, i.e., ratio between the durations of the pulse and the bit [31]. There are two types of OOK; non-return-to-zero (NRZ) OOK with $\gamma = 1$, and the return-to-zero (RZ) OOK for $\gamma < 1$, with the former being considered in this thesis. Hence, for NRZ OOK, the optical pulse occupies the entire bit duration while at RZ OOK, just a part of it. The unit energy pulse $p(t)$ of the OOK signal $s(t)$ can be expressed as [32]:

$$p(t) = \begin{cases} (2P_{\text{avg,OOK}})/\gamma, & \text{for } t \in [0, \gamma T_b) \\ 0, & \text{elsewhere,} \end{cases} \tag{2.1}$$

where T_b is the bit duration. Shown in Figs 2.2 and 2.3, are the illustrations of the two types of OOK scheme. It can be deduced that the $P_{\text{On,OOK}}$ for NRZ OOK and RZ OOK pulses are $2P_{\text{avg,OOK}}$, and $4P_{\text{avg,OOK}}$ respectively. Also, the pulse duration in Fig. 2.3 for bit ‘1’ is $T_b/2$ because of $\gamma = 0.5$.

2.2.2 PAM

The pulse amplitude modulation (PAM) scheme generalizes the ‘two-symbol’ OOK scheme to M symbols. It is an M-level scheme which utilizes the amplitude of an optical pluse to encode each data symbol. The input data symbols, having n positive integer bits per symbol (for $n = \log_2(M)$), are modulated using M different intensity levels. The PAM intensity levels shown in Fig. 2.4, can

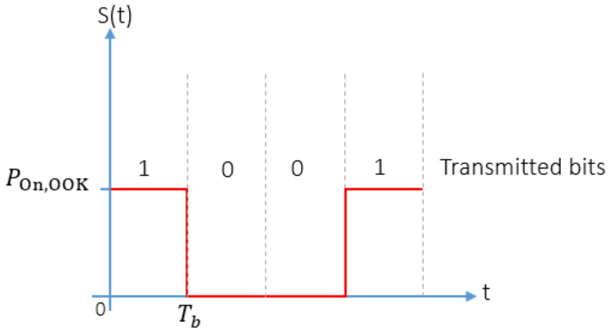

Figure 2.2: An NRZ-OOK Signal with $P_{\text{Off,OOK}} = 0$.

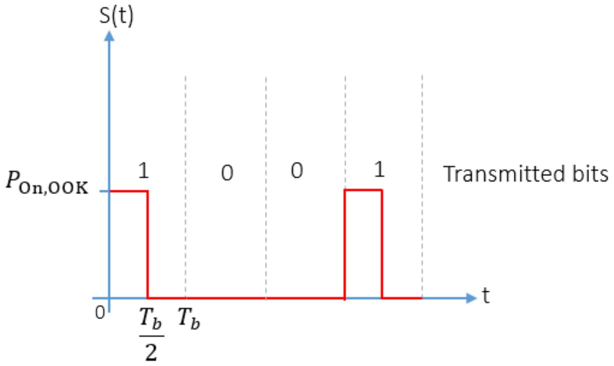

Figure 2.3: An RZ-OOK Signal with $P_{\text{Off,OOK}} = 0$, and $\gamma = 0.5$.

be expressed for $M > 2$ as [33, 29]:

$$P_m = \frac{2mP_{\text{avg,PAM}}}{M-1} + P_{\text{Off,PAM}}; \quad m = 0, 1, \ldots M-1, \tag{2.2}$$

where $P_{\text{avg,PAM}}$ is tha average transmit power and $P_{\text{Off,PAM}}$ is the lowest intensity level. Considering a PAM and OOK schemes with equal symbol duration T_s, at a fixed data rate, the PAM signal bandwidth BW_{PAM} is equal to BW_{OOk}/n, making PAM with $M > 2$ more bandwidth efficient [34, 29].

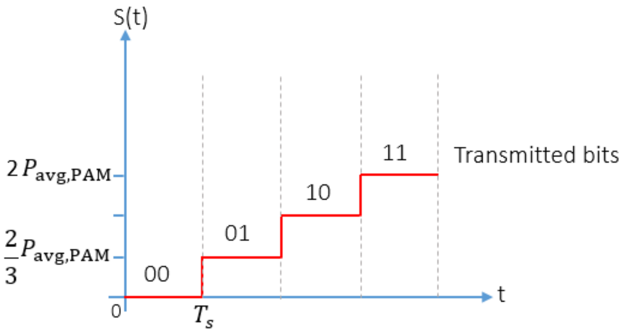

Figure 2.4: A 4-PAM Signal with $P_{\text{Off,PAM}} = 0$.

2.2.3 PPM

In the pulse position modulation (PPM) scheme, information data is encoded in the position of a pulse within a symbol. In an M-ary PPM, each symbol with duration T_s is assigned to M slots of equal duration T_{sl}, of which all the slots are empty except that with the information. Hence, $M-1$ slots are empty ("Off") while one slot is occupied ("On") with optical powers of $P_{\text{Off,PPM}}$ and $P_{\text{On,PPM}}$, respectively. As illustrated in Fig. 2.5, the pulse position depends on the sequence of the n bits to be transmitted. The average transmit optical power of the PPM scheme can be given as [29]:

$$P_{\text{avg,PPM}} = \frac{1}{M}\left((M-1)\,P_{\text{Off,PPM}} + P_{\text{On,PPM}}\right), \tag{2.3}$$

To achieve the same data rate R_b, the PPM has a bandwidth BW_{PPM} of lower efficiency compared to OOK, since $\text{BW}_{\text{PPM}} = MR_b/n$ [35, 34, 29].

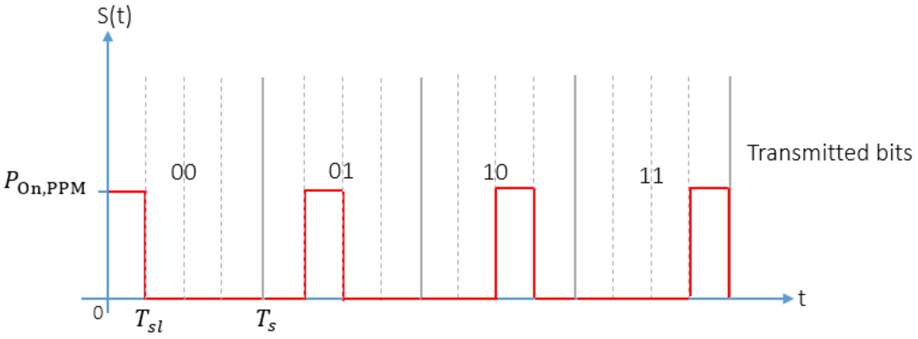

Figure 2.5: A 4-PPM Signal with $P_{\text{Off,PPM}} = 0$..

2.3 Transmitter

At the Tx of UWOC systems, LED- and LD-based optical sources are commonly used, which act as non-coherent and coherent sources respectively. Indeed, the choice of either LED- and LD-based optical sources mainly depends on the intended deployment of the optical link. In general, LED-based Txs offers a wide beam angle hence relaxing the effect of link misalignment with the trade-off of geometric loss. On the other hand, LD-based Txs have a narrow beamwidth that is more susceptible to PEs, which could be relaxed using retro-reflector while having considerably reduced loss from beam spreading. In the following, we discuss in more detail the considered optical source.

2.3.1 Light emitting diodes

LEDs has been receiving interest as an optical source in UWOC system benefiting from their low cost, power consumption and beam coverage [36, 37, 38, 39]. LED operation is based on the conversion of electrical energy into light, due to the energy released from the recombination of electrons and holes at the diode junction. The wavelength of the emitted light depends on the amount of energy released to travel across the band-gap of the semiconductor.

Several works have considered the use of LED-based Tx in UWOC system, especially with the intent to relax the stringent Tx-Rx beam alignment requirement. In [37], a single 3 W optical output power LED was experimentally used to transmit data using high level PPM over an underwater communication distance of 46 m to a highly sensitive PD at the Rx. Considering severe turbid water, [38] experimentally studied the channel of green LED-based Tx UWOC system installed on portable mobile platforms, where the channel was suggested to be a single-input multi-output system since the propagating beam is scattered in various directions. The work in [40] experimentally studied the effect of turbulence-induced scattering on LED transmitted light propagating through water, for proposing accurate turbulence channel modelling from a non-coherent light source.

2.3.2 Laser diodes

LDs are semiconductor light source devices with electrically pumped diodes creating lasing effects at the P-N junction. LD-based UWOC Txs have been considered for long-range, high data rate, and low power transmissions, especially in real-time sensitive applications. They offer advantages of relatively large modulation bandwidth, high energy efficient operations, and high beam directivity [41]. Hence LD has been used at the Tx in many UWOC experimental works.

In [42], a 520 nm green LD with 19.40 mW optical output power was used experimentally to achieve ∼ 2.70 Gbps data rate, over a communication range of 34.5 m with classical NRZ-OOK modulation scheme. Similarly, in [43], the UWOC system achieved a 500 Mbps data rate over a 100 m link distance.

Given these possibilites of the LD-based UWOC systems many works have investigated their potentials in the application of real-time video transmission. In [44], a 520 nm LD with 1.2 GHz BW was used to achieve real-time video streaming over an UWOC link range of up to 5 m. In addition, in [45], an LD-based UWOC bi-directional ultra-high definition video transmission was achieved. In [28], the concept of Aqua-Fi, a low power and compact UWOC system, was proposed for application in the internet of underwater things.

2.4 Receiver

Due to the attenuation of optical signal in UWOC systems, the choice of the photo-detecting device impacts the system performance. In general, the PD converts the optical signals into their corresponding electrical signals. To realize robust transmission over a relatively long range, PDs with high sensitivity, detection efficiency, and low-noise level components are essential. Some PDs used in UWOC include positive-intrinsic-negative (PIN) PD, avalanche photodiode (APD), photomultiplier tube (PMT), and SiPM. In this section we will discuss the advantages, drawbacks and potential applications of such PDs.

2.4.1 PIN PD

The PIN PD is one of the most commonly used PD in UWOC systems, especially at short wavelengths (400 - 500 nm). Although it features fast response time, low cost, and good tolerance to ambient light [1], its unit gain in photo-detection limits its application to a transmission distance of few tens of meters. The dominant noise source affecting signal detection in a PIN-based Rx is the thermal noise from the electronic circuitry [46].

Several works have explored the potentials of a PIN-based Rx in UWOC systems. In [47], the UWOC system performance for a 450 nm LD-based Tx and a PIN-based Rx was experimentally investigated. A reliable communication (i.e., having a relatively very low bit-error-rate (BER)) was achieved with data rates up to 50 Mbps over a link range of 3 m. Also, in [48], a 7.2 Gbps transmission rate was attained in seawater over a distance of 6.8 m.

2.4.2 APD

APD is one of the ideal PDs for long-range UWOC links since it has an internal gain in photo-detection, which is dependent on the applied bias voltage [1]. On the other hand, APD suffer from high operation voltage, complex control circuitry and high sensitivity to background noise [1]. The performance of APD-based Rxs are affected by shot noise from the received signal and thermal noise from the trans-impedance load resistor and the electronic circuitry [46].

Use of APD-based Rxs in UWOC systems have been extensively studied. Some works have studied the maximum attainable link range while using an APD especially in comparsion with a PIN PD [49, 50]. In [51], analysis of the UWOC link performance was carried out for an APD Rx considering various modulation techniques. Also, the interest of silicon APD- over germanium APD-based Rxs in UWOC systems was investigated. In [52], a real-time data transmission through the UWOC link of 50 m was experimentally achieved at a data rate of 25 Mbps using an APD Rx in clear water. Also, in another real-time experimental-UWOC work, [53] using an APD Rx, was able to carry out a full-duplex video communication with binary frequency shift keyiing modulation. The system was able to transmit at 1 Mbps with a signal-to-noise ratio (SNR) of 10.1 dB through a 10 m UWOC link.

2.4.3 PMT

PMT is a very high light-sensitive type of vacuum phototube, where the term photomultiplier describes the event as photons impinge on the sensitive area of the tube, the generated electrical energy in the form of current is largely multiplied. This PMT characteristic enables it to detect relatively low light intensities and also be used for long-range UWOC applications. The PMT-based PD offers high gain, low noise, and large aperture. On the other hand, PMT suffers from sensitivity to magnetic fields, high operation voltage, ease of malfunctioning due to exposure to high-intensity light, bulkiness and high cost [54, 55].

Given the aforementioned high sensitivity feature of the PMT, it will possibly undergo signal distortion if operating at saturation [55]. In [56], an UWOC system is evaluated experimentally based on the effect of the PMT saturation on BW limitation and performance degradation. An adaptive control scheme was proposed to enhance the system's stability and reliability due to the dynamic optical power change. The concept involved tuning the captured optical power and the PMT gain following the detected optical signal. Some experimental works on PMT are motivated by applications requiring high Rx sensitivity with probably low transmit power [57, 58]. Furthermore, [19] investigated the effect of solar noise on the performance of a PIN-, an APD- and a PMT-based UWOC system. Results show that for relatively low depths (typically less than 80 m), a PIN-based Rx is less susceptible to background noise, compared to that of an APD and a PMT. Due to the very high sensitivity of the PMT to the presence of solar radiations, it was proposed to be deployed at relatively large operational depths (more than 200 m) [19].

2.4.4 SiPM

SiPMs, which are also referred to as multi-pixel photon counter (MPPC), are similar to PMT due to their high sensitivity and time resolution. However, the already discussed drawbacks of PMT makes the SiPM a suitable alternative especially due to their implementation simplicity, low operation voltage, insensitivity to magnetic fields and mechanical robustness [36]. In [59] and [60], the suitability and limitations of using an SiPM-based Rx in an UWOC link was discussed respectively.

In several works, the practical interest of SiPMs in UWOC systems have been evaluated, particularly with respect to optical modems [27], optical orthogonal frequency-division multiplexing signaling [61, 29], and frequency-domain equalization [62]. Given in [36], was a concise discourse of the system modelling, practical advantages and drawbacks in deploying SiPM-based Rx in UWOC. For an attenuation length[1] of 9.28, [64] was able to experimentally demonstrate a transmission data rate of 1 Gbps in weak turbulence using a novel SiPM-based Rx. Also in [37], a reliable 46 m LED-based UWOC was established despite the very low received optical power. This was made possible by the use of MPPC Rx and a PPM scheme, both contributing to the high sensitivity and power efficiency of the system respectively. In [65], still leveraging on the potentials of MPPC and PPM, a LD-based UWOC system with ultra-low transmit optical power was able to achieve a 46 m link range with data rates in Mbps.

---

[1] Attenuation length is a mimic of the level of water turbidity [63].

2.5 Aquatic channel

The light propagating through the aquatic channel is affected by several factors, which vary according to the underwater environment and the type of optical source considered. This necessitates carrying out accurate channel modelling to reliably design and evaluate the UWOC system performance. In this section, we will briefly explain the dominant phenomena affecting the UWOC link performance, i.e., absorption and scattering, which are both dependent on the water type and wavelength of the optical source. Furthermore, we will discuss the characterization of the channel.

2.5.1 Absorption and scattering

Absorption and scattering occur from interactions between particles present in the seawater and the propagating optical signal. Absorption results from the loss in the signal intensity due to the absorbing of some of the emitted photons by the dissolved particles in water. On the other hand, scattering describes the change in direction of the photons that collide with undissolved particles. Note that, absorption is dependent on the signal wavelength and the constituents of the seawater, which are; pure seawater composition, phytoplanktons, color dissolved organic material, and non-algal materials [1]. Scattering occurs mainly due to the concentration of suspended particulates in the water, hence, it is dominant in coastal waters and experienced in clear waters due to the change of the water refractive index from fluctuations in pressure, salinity and temperature [1].

In this thesis, we assume the classical Beer-Lambert (BL) model, which follows an exponential decay, to calculate the optical signal power loss through the water channel for a given distance. The BL model accounts for the effect of both absorption and scattering (particularly for a single photon) on the propagating light beam. A combination of absorption and scattering coefficients is referred to as diffuse attenuation coefficient K_{d} (in the unit of m^{-1}). Following the BL model, channel loss L_{ch} through a distance L is given by [36]:

$$L_{\mathrm{ch}} = e^{-(L K_{\mathrm{d}})}. \tag{2.4}$$

2.5.2 Channel impulse response

We use the channel impulse response (CIR) to characterize the optical channel in order to efficiently analyze and implement the appropriate technique to improve the UWOC system performance. The impulse response (IR) of an aggregate channel is dependent on the optical source, the PD and the underwater channel, and could be expressed as [36]:

$$h_{\mathrm{ag}}(t) = h_{\mathrm{os}}(t) * h_{\mathrm{ch}}(t) * h_{\mathrm{pd}}(t), \tag{2.5}$$

where $h_{\mathrm{os}}(t)$, $h_{\mathrm{ch}}(t)$, and $h_{\mathrm{pd}}(t)$ denote the IRs of the optical source, the aquatic channel and the PD, respectively, and " $*$ " denotes convolution. Although many works in literature assume that the underwater channel is frequency non-selective, which is practically valid [66], however, due to scattering especially at high rate of data transmission, multipath propagation of the signal to the PD can result in the frequency selectivity of the channel. For a frequency non-selective channel, $h_{\mathrm{ch}}(t) = L_{\mathrm{ch}}\,\delta(t)$, where L_{ch} is the channel loss given in (2.4) and $\delta(\cdot)$ is the Dirac function. The IR of the optical source and the PD can be modeled as a 1^{st}-order low pass filter with cut-off frequencies of $f_{\mathrm{c,os}}$ and $f_{\mathrm{c,pd}}$, respectively. Hence, $h_{\mathrm{os}}(t)$ and $h_{\mathrm{pd}}(t)$ can then be given as [36]:

$$h_{\mathrm{os}}(t) = \exp\left(-2\pi f_{\mathrm{c,os}}\, t\right), \tag{2.6}$$

$$h_{\mathrm{pd}}(t) = \exp\left(-2\pi f_{\mathrm{c,pd}}\, t\right). \tag{2.7}$$

Underwater channel characterization has been explored by several simulation- and experimentally-based UWOC works [67, 66, 68]. In [66], Monte Carlo simulation was used in the channel characterization of an UWOC system for realistic system and channel parameters in different water types. It was observed that, except for highly turbid waters, the channel time dispersion is negligible for moderate link ranges. Also in [68], the frequency response of an underwater optical channel was experimentally measured for different attenuation lengths, using a high-sensitivity, and high-dynamic-range strategy. The measurements of the spatial and temporal dispersions of the signal was with respect to the pointing angle between the Tx and the Rx. Results confirm as in the simulation work of [66], that there is negligible temporal dispersion in clear waters while the effect of delay spread on the signal is significant at longer attenuation lengths.

2.6 Practical challenges

In the course of deploying an UWOC system, several practical challenges may arise and subsequently degrade the reliability of the communication. Some of these challenges are experienced as a result of fluctuations in the refractive index of the water, roughness of the sea surface, instability of the transceiver host platforms, movement of divers or marine life across transmission link, and unwanted light (i.e., noise) being captured by the PD. In this section, we will highlight some of these challenges and some of the proposed techniques to mitigate them.

2.6.1 Oceanic turbulence

Oceanic turbulence is the random variations of the refractive index along the aquatic medium, due to changes in density, temperature, and salinity. These inconsistencies result in fluctuations in both intensity and phase of the average received signal of an UWOC system [1], hence degrading its performance. In [40], the impact of turbulence-induced scattering on an optical signal from a coherent and non-coherent light source propagating through water was carried out. It was observed that the signal of a non-coherent light is less susceptible to temperature inhomogeneity induced turbulence. Some experimental works have confirmed that the turbulence-induced fading on the optical signal, described as weak and moderate-to-strong oceanic turbulence, follow log-normal and Gamma-Gamma distributions respectively [69, 70]. Also, several turbulence mitigation schemes such as aperture averaging, adaptive optics and spatial diversity based Rx have been proposed [71, 72, 73].

2.6.2 Link misalignment

Given the swerving nature of water bodies often initiated by wind waves, ocean currents, etc., there is often transceiver beam PEs, especially during communication involving mobile platforms (autonomous underwater vehicle (AUV)) even while stationary. Hence, to maintain reliable communication there is significant interest in keeping the optical beam focused on the effective light-collecting area of the PD at the Rx to mitigate the effect of beam misalignment. Note that the use of position acquisition and tracking systems may increase system cost, complexity and power consumption. In [74], the impact of link misalignment on an UWOC system performance was investigated. Results show that some range of link alignment offset is allowable to still maintain reliable communication. The use of smart transceiver arrays was explored in [75] to relax the beam pointing requirement. Furthermore, the impact of beam divergence angle on minimizing link misalignment was studied in [76]. It was observed to be more efficient in less turbid waters. It is worthy of note that due to scattering which causes the optical beam to spread in various directions, the impact of link misalignment is minimized in high turbid waters [68], hence pure sea waters are more susceptible to link misalignments.

2.6.3 Solar background noise

UWOC systems that operate at relatively shallow depths (depth of tens of meters) are susceptible to receiving solar radiations which results in an increase in the background noise level at the Rx, hence limiting the system performance especially for a large Rx field-of-view (FoV). The magnitude of such noise component depends on the position of the sun with respect to the optical source wavelength of the UWOC system, which could be minimized by the use of a narrow-band optical filter at the Rx. The effect of solar background noise on the performance of an UWOC system was investigated in [19, 60, 34], for various types of PDs. Considering a worst-case scenario, i.e., the sun being at its zenith, the effect of different Rx characteristics such as the FoV, and the aperture size was studied in [19]. Results showed the PIN PD to be less sensitive to background noise, in contrast to a PMT. In [77], the impact and physical constraints of optical filters was studied in mitigating background sunlight on LED-based UWOC system. An adaptive rate scheme coupled with a very narrow band spectral filter was used in [78] to reduce the background solar noise. It is of interest to design an UWOC optimization system, that adjusts FoV so as to reduce the amount of background light while maximizing the amount of captured optical signal [1]. It is worthy of note that at larger depths, biological luminance or blackbody radiation is the main source of unwanted background light [1].

2.6.4 Physical obstructions

Due to the nature of the UWOC channel, the performance of the UWOC systems may suffer from degradation due to obstruction of the communication link by the presence of marine life or activities, hence interrupting the signal transmission. In the advanced ray tracing based work which was studied in [79], the channel modeling and characterization study of an UWOC system affected by shadowing and blocking was presented. To overcome such obstruction, different techniques could be used to re-transmit the lost signal and achieve a reliable communication, such as forward error correction (FEC), automatic repeat request (ARQ) [80], hybrid ARQ [1], and also, spatial diversity techniques [81]. For instance, in [82], the performance of an UWOC system subject to both bubbles and obstruction were experimentally investigated for different spatial modes, namely; Gaussian, orbital angular momentum (OAM), and Bessel. Their results show the Bessel mode, with its diffraction-free and obstruction-tolerant inherent features, have the best performance against the impact of obstructions.

2.7 Chapter summary

In this chapter, we briefly discussed the different components of the UWOC systems and some practical challenges that could be encountered. In particular, we reviewed the choice of an optical source at the Tx, and the choice of PD at the Rx. Following this, we briefly discussed the aquatic channel, followed by the main challenges that affect the system performance. In the next chapter, we will discuss the SiPM-based Rx for an UWOC system, in relation to existing works, operating principle, limitations, and ideal deployment scenarios.

Chapter 3

Silicon photomultiplier for UWOC

Contents

3.1 Introduction

The light beam propagating through the aquatic media interacts with water molecules and other particulates, resulting in either absorption or scattering. Consequently, the transmission range of the UWOC system is limited due to the corresponding optical signal attenuation. Extensive research has focused on the deployment of sensitive PDs at the Rx with the intent to improve the level of received intensity despite the channel attenuation, and hence, to extend the achievable link range. A classically-used high inherent gain PD is the PMT, which is extremely sensitive making it possible to detect very low-intensity levels. Some drawbacks in the implementation of PMTs, especially in energy-efficient and portable-platform UWOC applications, are its large size, high operation voltage, high cost and sensitivity of the Rx to magnetic fields.

An effective alternative to PMTs, is the SiPM, which compared to PMTs, offers advantages such as low bias voltage, low cost, and small size. Like PMTs, SiPMs are highly sensitive to low optical signal levels even to a single photon. There have been several works highlighting the expectations on the use of SiPM for signal detection in UWOC applications.

In [36], for an OOK modulated LED at the Tx, the performance of SiPM and PMT based Rxs were studied based on simulation results for practical considerations. This study was subsequently implemented for an underwater optical modem in [27]. Also, [83] carried out an experimental work using differential phase-shift keying (DPSK), where the performance of an SiPM based Rx was compared with that of an APD. Given the limited BW of an SiPM, [62] considered using PAM with frequency-domain equalization (FDE) for an SiPM based Rx. Also, to boost the data rate of the UWOC system, the experimental work of [64] utilized analogue output signal operation mode with decision feedback equalization to achieve 1 Gbps over 10 attenuation length. Lastly, covering the scope of the suitability and the limitations of using SiPM in UWOC systems, the works of [59] and [60] gave a concise and analytical discussion with simulation results of the practical interests and drawbacks of SiPMs respectively. A tabulated summary of other works employing SiPM based Rxs for UWOC are given in Tables 3.1.

The remainder of the chapter is organized as follows. In Section 3.2, an overview of SiPMs is presented including their working principle, performance parameters, the photon-counting procedure and the impact of non-linear distortion. Then, in Section 3.3, using OOK modulation we investigate the achievable link range of an SiPM-based Rx for a desired BER and further present the impact of some Tx and Rx parameters on the link performance. Lastly, Section 3.4 concludes the chapter.

3.2 SiPM-based receivers

The potential and applications of SiPM based Rxs can be better accessed from its working principles. Hence, in this section, we discuss the SiPM in a technical context together with its associated parameters in relation to photon counting and its limitations including non-linear distortion.

3.2.1 SiPM structure

An SiPM, also known as MPPC, is a solid-state PD. It is a common-bias and common-output array of APD elements operating in the Geiger mode (i.e., reverse-biased above their breakdown voltage), causing them to have an avalanche breakdown when they have photons incident on them (see Fig. 3.1) [87]. In this mode of operation, the APD has the advantage of large gain resulting in a high sensitivity to very low optical intensity levels down to a single photon, hence referred to as a single photon avalanche diode (SPAD) [88]. Furthermore, these SPADs are connected in parallel to an active or passive quenching device that stops the Geiger discharge, thus reducing the reverse voltage below its breakdown. This drop in voltage is taken as the SPAD recharging back to its bias

Table 3.1: Recent works on the use of SiPM-based Rxs for UWOC.

Year	Refs.	Tx	Modulation	Data rate (Mbps)	Link range (m)	Approach	Water type
2017	[36]	Blue LED	OOK	-	-	Theoretical	Clear and coastal
2018	[65]	Blue LD	PPM	2.5	46	Experimental	Clear
2019	[62]	Blue LED	PAM + FDE	-	-	Theoretical	Clear
2019	[84]	Green LD	DMT-OFDM	312.03	21	Experimental	Tap
2019	[85]	Blue-Green μLED	OOK	100	1.5	Experimental	Harbour
2020	[61]	Blue LED	LACO-OFDM	20	74.3	Theoretical	Clear
2020	[86]	Blue LD	NRZ-OOK	16.78	50	Experimental	Clear
2021	[39]	Blue LD	OOK	1	100	Theoretical	Clear
2021	[63]	Green LD	OOK	20	24	Experimental	Coastal

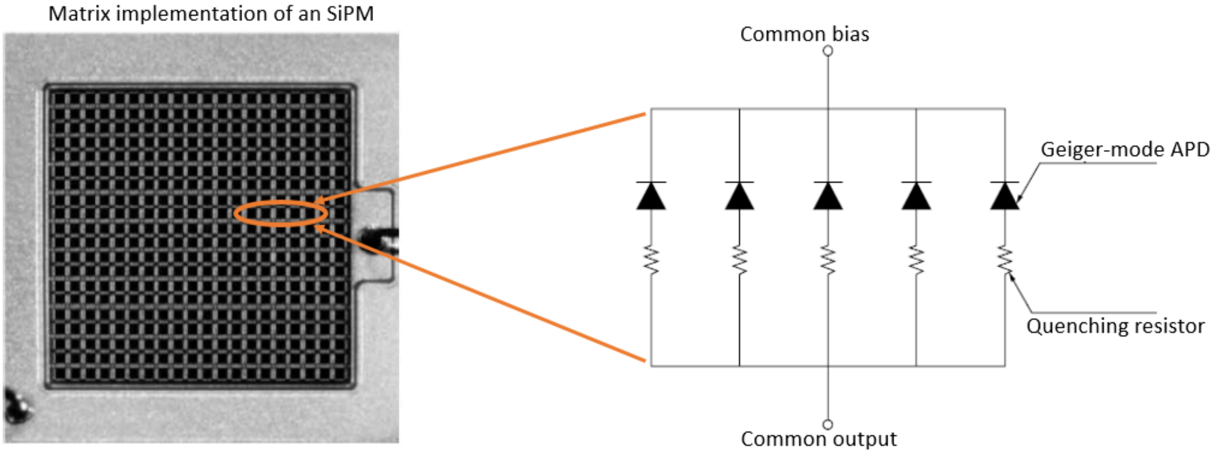

Figure 3.1: Illustration of a passively quenched SiPM structure (reproduced from [87]).

voltage and ready for further detection of arriving photons (see Fig. 3.2) [88].

The structure of an SiPM pixel is related to its photosensitivity. The two distinct structures of an SiPM pixel are n-on-p and p-on-n (see Fig. 3.3), where for an n-on-p structure, an n doped junction is on top of a p-type substrate (the inverse for p-on-n structure) [87]. Due to this structural

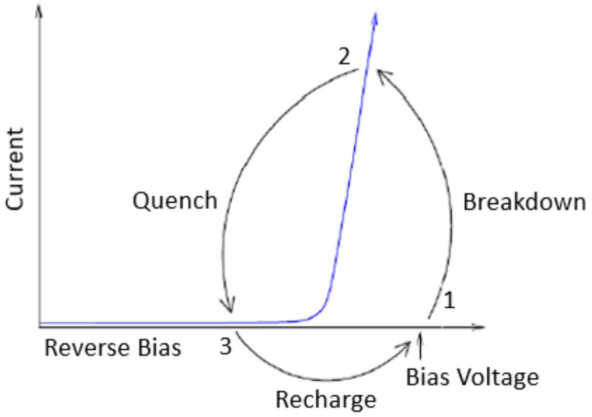

Figure 3.2: Current-Voltage characteristic of a SPAD working in Geiger mode (reproduced from [88]).

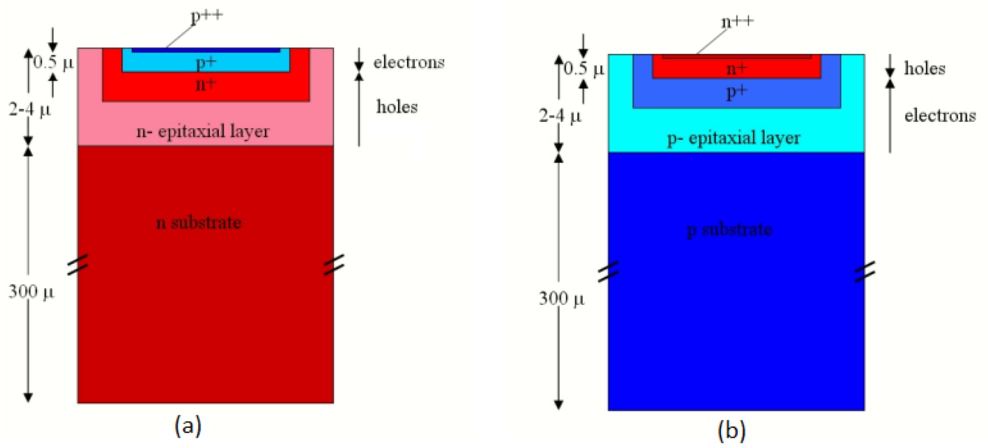

Figure 3.3: Illustration of (a) p-on-n and (b) n-on-p SiPM structure (reproduced from [89]).

configuration[1], the photosensitivity of an n-on-p structure is higher for longer wavelength photons at the expense of the shorter wavelength photons, and vice versa for the p-on-n structure. This results in SiPMs with the p-on-n structure more sensitive to wavelengths such as in the blue spectrum, and the n-on-p structure for the red region [87].

---

[1] Short wavelength photons (e.g. 450 nm) have shorter absorption length in silicon (~ 0.8 μm), while that of long wavelength photons (e.g. 680 nm) are longer (~ 5 μm) [89]. Once a photon is absorbed in a silicon layer (n- or p-type), an electron-hole pair is created. At the n (or p) layer, the hole (or electron) travels towards the high electric field of the pn junction where it generates an avalanche breakdown. Due to the low impact ionization threshold of electrons (1.75×10^5 V/cm), they trigger an avalanche with a higher probability than holes (2.5×10^5 V/cm) [90].

3.2.2 Photon counting

As aforementioned, an SiPM comprises of an array of SPADs. When a photon is incident on the sensitive area of a SPAD, an avalanche breakdown is initiated and a pulse is generated at the SPAD's output (hence considered as a single photon counter). The SiPM output C_{ph} is the combination of the SPAD outputs $c_{\mathrm{ph}}(i)$. Assumming an SiPM consists of $\mathrm{N_{SPAD}}$ number of SPADs, the SiPM output is expressed as [36]:

$$C_{\mathrm{ph}} = \sum_{i=1}^{N_{\mathrm{SPAD}}} c_{\mathrm{ph}}(i). \tag{3.1}$$

The detection of photons in an SiPM is modelled by a Poisson distribution [91]:

$$\Pr(C_{\mathrm{ph}} = k) = \exp(-\mu)\,\frac{\mu^k}{k!}, \tag{3.2}$$

where $\Pr(\cdot)$ denotes probability and μ stands for the average photon count, which is related to the responsivity of the SiPM at symbol duration T [92]:

$$\mu = \frac{T}{e\,G}\left(\mathcal{R}_{\mathrm{e}}\,P_{\mathrm{Rx}} + f_{\mathrm{DCR}}\big(1 + P_{\mathrm{AP}} + P_{\mathrm{CT}}\big)\,e\,G\right), \tag{3.3}$$

where, P_{Rx} is the received power, and $\mathcal{R}_{\mathrm{e}}$ is the SiPM responsivity, given by [88]:

$$\mathcal{R}_{\mathrm{e}} = \left(\frac{\Upsilon_{\mathrm{PDE}}}{E_{\mathrm{ph}}}\right)\big(1 + P_{\mathrm{AP}} + P_{\mathrm{CT}}\big)\,e\,G. \tag{3.4}$$

Here, Υ_{PDE} is the photon detection efficiency and $E_{\mathrm{ph}} = hc/\lambda$ is the photon energy at wavelength λ, with h the Planck constant and c the speed of light. Also, P_{AP}, P_{CT}, e, G denote the probability of after-pulsing, probability of cross-talk, electron charge, and SiPM gain, respectively. Also, both the SiPM signal current (I_s) and dark current (I_d) can be deduced from (3.3) as:

$$I_s = \mathcal{R}_{\mathrm{e}}\,P_{\mathrm{Rx}}, \tag{3.5}$$

$$I_d = f_{\mathrm{DCR}}\big(1 + P_{\mathrm{AP}} + P_{\mathrm{CT}}\big)\,e\,G, \tag{3.6}$$

where f_{DCR} is the dark count rate.

The evaluation of the SiPM performance depends on the aforementioned parameters. Some of the parameters of the SiPM are temperature-dependent, such as photon detection efficiency Υ_{PDE}, gain G, and dark count rate f_{DCR}. A more detailed description of the SiPM parameters is presented below.

Photon detection efficiency: Υ_{PDE} is the probability that a photon hits the sensitive area of the SiPM and then triggers an avalanche breakdown on one of the micro-cells (i.e., SPADs) [88]. It is formulated as the product of the silicon quantum efficiency, the SiPM pixel fill-factor and the Geiger-mode avalanche probability (i.e., the probability that a detected photon generates an avalanche) [87]. The quantum efficiency accounts for the probability that an incident photon creating an electron-hole pair can trigger an avalanche, it also depends on the wavelength of the incident light [88]. The fill factor is the ratio of the pixel photosensitive area to the total physical area of the SiPM taking into account the physical gaps between the micro-cells and the situated space for the quenching circuit.

Gain: The SiPM gain depends mainly on the overvoltage (difference between the breakdown voltage and the bias voltage of APDs) and the junction capacity. A large gain is as a result of the SPADs operating slightly (10% -20%) above the breakdown voltage [93]. For an efficient performance evaluation of an SiPM Rx based UWOC system, it is essential to work at a constant SiPM gain. However, SiPM gain decreases with increased temperature due to the increase in the breakdown voltage [87]. This necessitates a temperature control or compensation circuitry, since appropriately adjusting the applied bias voltage as temperature changes aids to maintain a fixed gain.

Dark count rate: f_{DCR} is a result of a SPAD breaking down due to thermally generated electrons, even in the dark. It is the average number of dark counts per second, with unit in Hz [87]. This random and obviously uncorrelated effect to the photon-initiated output pulses makes f_{DCR} undesirable for single-photon counting purposes. This noisy effect can be reduced by thermoelectric cooling of the SiPM at a rate of about 0.5 for every approximately 10°C reduction in temperature [87]. Another method to efficiently inhibit the f_{DCR} effect is through using a very small time range for the single-photon events and its knowledge made available at the detector via an external trigger [87].

After-pulsing probability: P_{AP} is the probability of triggering two successive avalanches in the same microcell caused by a single photon due to charge carriers blocked during the primary avalanche [87]. It increases proportionally to the bias voltage, since increasing the bias voltage leads to an increase in the number of charge carriers in an avalanche, thus, this noise is regarded as signal-dependent [94].

Optical cross-talk: As scattered avalanche carriers collide during avalanche breakdown, some have their kinetic energy emitted as photons. These resulting photons often travel to a neighbouring SPAD to initiate an avalanche. This occurrence is referred to as an optical crosstalk [87]. This crosstalk photon could create an electron-hole pair within or outside an SiPM pixels depletion layer and trigger an avalanche, the latter is a delayed crosstalk while the former is a prompt crosstalk [87]. During signal processing, to remove a prompt crosstalk and delayed crosstalk, one can use an upper-level discriminator in single-photon counting and a time-delay filtering algorithm respectively [87].

3.2.3 Non-linear distortion

A SPAD can only detect one photon at a time and requires some time to recharge before being able to detect any further impinging photon. This recharge time is referred to as dead-time or recovery time, denoted as τ_{d}. When more than one photon interacts with the same microcell within a time interval shorter than τ_{d} (eg. at increased optical intensity), the SiPM goes into saturation where its response undergoes a non-linear distortion (NLD), i.e., an unproportional relationship between the received photons and the output pulses of the SiPM [91].

The quenching circuitry used to stop the Geiger discharge determines the characteristics of the SPADs during the SiPM saturation. There are two types of quenching devices, namely; passive quenching (PQ) and active quenching (AQ). In PQ, the subsequent incident photons will not be detected but will prolong the microcell dead-time, leading to the SPAD collapse (i.e., paralyzing the photon detection). For AQ, the arriving photons during the dead-time are not detected and will not prolong the dead-time, hence they have a non-paralyzing effect [36]. During a symbol duration T, the relationship between the average photon count μ and the actual average photon count for PQ and AQ schemes are expressed as [91]:

$$\mu_{\mathrm{PQ}} = \mu \, \exp\left(-\frac{\mu \tau_{\mathrm{d}}}{T\,N_{\mathrm{SPAD}}}\right), \tag{3.7}$$

$$\mu_{\mathrm{AQ}} = \frac{\mu}{1 + \frac{\mu \tau_{\mathrm{d}}}{T\,N_{\mathrm{SPAD}}}}. \tag{3.8}$$

Their corresponding number of maximum counted photons before saturation are given by [91]:

$$\mu_{\mathrm{PQ,max}} = \frac{T\,N_{\mathrm{SPAD}}}{\exp(1)\,\tau_{\mathrm{d}}}, \tag{3.9}$$

$$\mu_{\mathrm{AQ,max}} = \frac{T\,N_{\mathrm{SPAD}}}{\tau_{\mathrm{d}}}. \tag{3.10}$$

To further show the effect of PQ and AQ, presented in Fig. 3.4 are the simulation results for the output photon count of an SiPM with respect to the captured optical power, P_{Rx}, at time intervals 1 μs and 1 ms. The parameters of the considered SiPM are given in Table 3.2 and λ is 470 nm.

Shown in Fig. 3.4 are the two operational regimes of the SiPM with distinctive characteristics for PQ and AQ devices. In the first regime, there is a linear relationship between the output average photon count and the received power P_{Rx}, until a maximum photon count ($\mu_{\mathrm{PQ,max}}$ or $\mu_{\mathrm{AQ,max}}$) subject to T is reached. Beyond this point is the second regime showing the NLD. The photon count is constant for the case of AQ-SiPM while it rapidly collapes and marks the start of the saturation regime for the case of PQ-SiPM. The time interval T = 1 ms allows more photons to be counted compared to T = 1 μs, despite having the same N_{SPAD}. Note that the saturation point occurs at the same optical received power P_{Rx} for both T = 1 μs and 1 ms. This suggests at the same dead-time, the maximum received intensity before saturation is equal even at varying time intervals. The amount of photons at the SiPM output can be converted to the corresponding electrical signal amplitude using a photon-to-amplitude equalizer [91, 36].

In this work, we consider only PQ devices since the commercially available AQ-SiPMs are more expensive with very small number of SPADs (e.g., 8 for the ID Quantique SiPMs [95]), compared to PQ devices (e.g., 10998 for SensL B-series 30020 SiPMs [96]) [36].

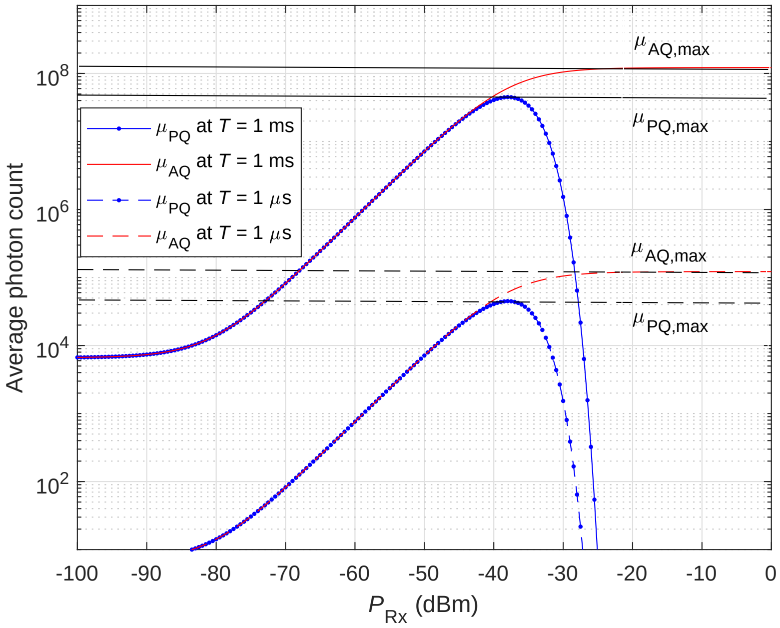

Figure 3.4: SiPM photon-count as a function of optical received power P_{Rx}, for the cases of AQ (red) and PQ (blue).

3.3 Performance evaluation for UWOC

In this Section, we study the UWOC link performance for an uncoded NRZ OOK optical signal transmission using an IM/DD scheme with an LED Tx and an SiPM-based Rx. The aquatic channel is considered to follow the BL attenuation model. Our first analysis are made based on the maximum achievable link range based on a target BER for UWOC systems operating in both clear and coastal waters. We further investigate the impact of some system parameters on the link performance and discuss their relevance in the UWOC system design.

3.3.1 Signal transmission model

We assume that at the Tx the LED follows a Lambertian model with order m, which specifies the optical beam directionality [97]. The resulting radiation intensity pattern at transmit optical power P_{Tx} is expressed as:

$$R_p(\phi) = P_{\text{Tx}} \frac{m+1}{2\pi} \cos^m(\phi), \tag{3.11}$$

where, $\phi \in \left\{\frac{-\pi}{2}, \frac{\pi}{2}\right\}$ is the angle of irradiance at the Tx, and $m = -\ln(2)/\ln\left(\cos\left(\phi_{\frac{1}{2}}\right)\right)$ where $\phi_{\frac{1}{2}}$ is the Tx semi-angle at half-power. The selected LED emits at $\lambda = 470\,\text{nm}$ [98], and $m \approx 45$, corresponding to $\phi_{\frac{1}{2}} \approx 10°$. At the Rx, the parameters of our considered SiPM is given in Table 3.2. The impact of solar background radiation is ignored as we assume operation at large depths. The op-

Table 3.2: Rx parameter specification

Parameter	Value
SiPM active area A_{PD}	$9\,\mathrm{mm}^2$
SiPM, number of SPADs	10998
SiPM gain G	10^6
SiPM Υ_{PDE}	24 %
SiPM f_{DCR}	6.6 MHz
SiPM P_{CT}	0.03 %
SiPM P_{AP}	0.2 %
SiPM deadtime τ_d	90 ns

tical power loss through the water is modelled by an exponential decay model as $e^{-(L K_{\mathrm{d}})}$, where K_{d} is the diffuse attenuation coefficient. The model takes into account the effect of seawater absorption and scattering on the beam, especially for relatively wide beam [99], which is typically the case when considering LEDs at the Tx [19].

Furthermore at the Rx, prior to the PD, we consider the use of an optical filter with signal transmission $T_{\mathrm{s}}(\theta)$ [19], as well as a non-imaging concentrator of refractive index $n_r = 1.5$ and gain $g(\theta)$ with $\theta \in \{0, \frac{\pi}{2}\}$ being the incidence angle [97]. The effective Rx light collection area A_{eff} is given in terms of the active area of the SiPM A_{PD}, as[97]:

$$A_{\mathrm{eff}}(\theta) = \begin{cases} A_{\mathrm{PD}}\, T_{\mathrm{s}}(\theta)\, g(\theta) \cos(\theta), & \theta \leq \theta_{\mathrm{FoVr}} \\ 0, & \theta > \theta_{\mathrm{FoVr}}, \end{cases} \tag{3.12}$$

where

$$g(\theta) = \frac{{n_r}^2}{\sin^2(\theta_{\mathrm{FoVr}})}, \tag{3.13}$$

and θ_{FoVr} is the Rx FoV. For the sake of simplicity, we assume the optical filter signal transmission T_{s} is nearly constant and equal to 1 [100].

Considering, a perfectly aligned Tx-Rx at a distance L, the received intensity P_{Rx} on the PD of area A_{PD} can be expressed as [101]:

$$P_{\mathrm{Rx}} = R_p(\phi)\, e^{-(L K_{\mathrm{d}})}\, \frac{A_{\mathrm{eff}}(\theta)}{L^2}. \tag{3.14}$$

BER analysis: Considering an IM/DD scheme based on uncoded NRZ OOK modulated signal bitstream, let $P_{\mathrm{Tx},0}$ and $P_{\mathrm{Tx},1}$ denote the transmitted optical power for bits '0' and '1', respectively with the extinction ratio, defined as $\xi = P_{\mathrm{Tx},0}/P_{\mathrm{Tx},1}$. Using (3.14) we calculate the received power for both "Off" and "On" symbols denoted by $P_{\mathrm{Rx},0}$ and $P_{\mathrm{Rx},1}$, as well as the corresponding average number of received photons $\mu_{\mathrm{PQ},0}$ and $\mu_{\mathrm{PQ},1}$. The detection threshold μ_{th}, for OOK demodulation at the Rx, is given as [36]:

$$\mu_{\mathrm{th}} = \sqrt{\mu_{\mathrm{PQ},0}\, \mu_{\mathrm{PQ},1}}. \tag{3.15}$$

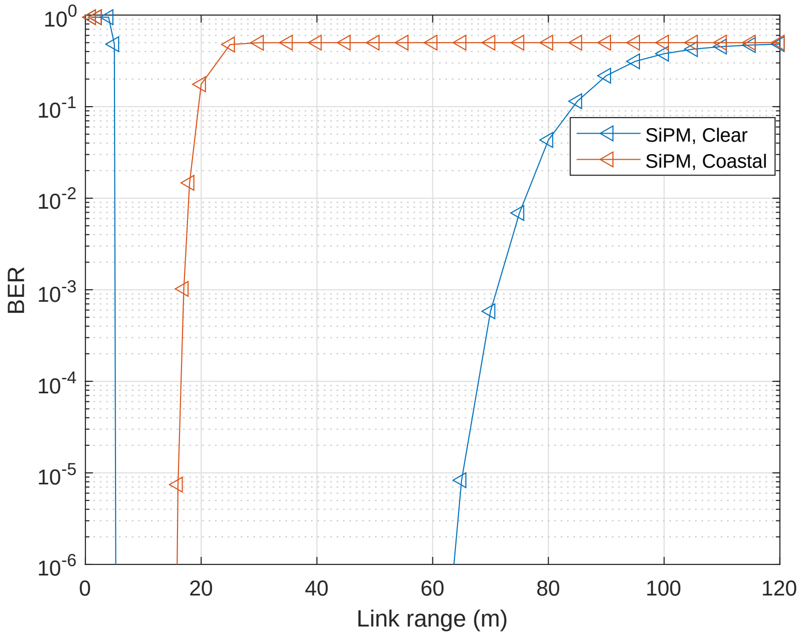

Figure 3.5: BER versus link range fo PQ-SiPM-based Rxs in clear and coastal waters. $P_{\mathrm{Tx},1}$ = 1 W, uncoded OOK with $\xi = 0$, $T = 1\mu$s, $m = 45$, $A_{\mathrm{PD}} = 9\,\mathrm{mm}^2$.

The above detection threshold is further used to realize the probability of error Pe, which for the SiPM-based Rx is given as [92]:

$$\begin{aligned} Pe &= \frac{1}{2}\Pr\left(\mu_{\mathrm{PQ}} \le \mu_{\mathrm{th}} | \mu_{\mathrm{PQ},1}\right) + \frac{1}{2}\Pr\left(\mu_{\mathrm{PQ}} > \mu_{\mathrm{th}} | \mu_{\mathrm{PQ},0}\right) \\ &= \frac{1}{2}\left[1 - P_c\left(\mu_{\mathrm{th}}, \mu_{\mathrm{PQ},0}\right) + P_c\left(\mu_{\mathrm{th}}, \mu_{\mathrm{PQ},1}\right)\right], \end{aligned} \tag{3.16}$$

where $P_c\left(x, y\right)$ denotes the cumulative distribution function of the Poisson distribution of x with parameter y.

3.3.2 Numerical results and analysis

In this subsection, we evaluate for the cases of clear and coastal waters through simulations, the BER performance of a horizontal UWOC system with respect to the communication range for SiPM-based Rx. Further, we investigate the effect of some Tx and Rx parameters on the link performance in clear waters.

3.3.3 Impact of clear and coastal ocean waters

Given in Fig. 3.5 are results of BER versus link range for a PQ-SiPM based Rx with no concentrator lens. We consider an UWOC system operating in both clear and coastal ocean waters, with K_{d} = 0.08 m^{-1} and 0.5 m^{-1} respectively. The 'paralyzing' effect from the SiPM NLD is observed at a

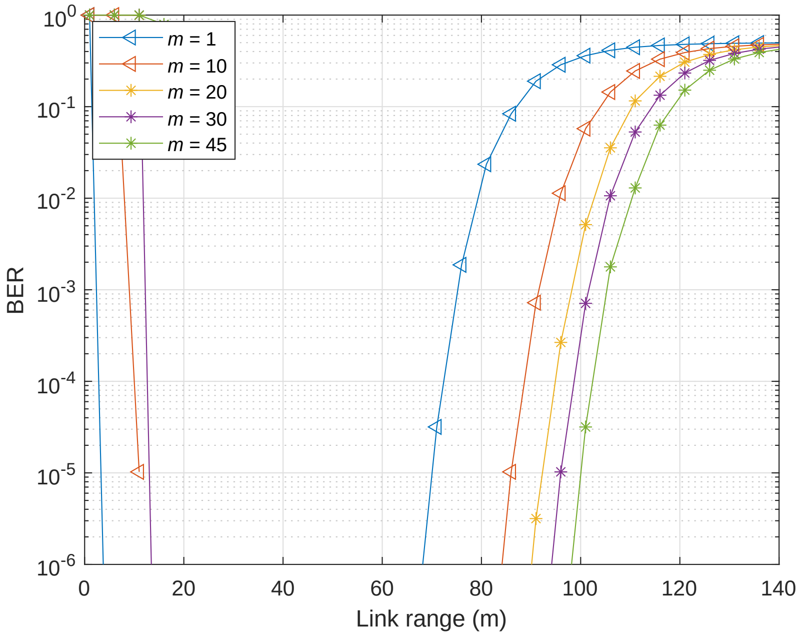

Figure 3.6: Effect of Lambertain order m on the link BER in clear waters. $P_{\mathrm{Tx},1}$ = 1 W, uncoded OOK with ξ = 0, $T = 1\mu$s, $A_{\mathrm{PD}} = 9\,\mathrm{mm}^2$, $\theta_{\mathrm{FoVr}} = 16°$.

short link range (less than 5 m) due to a very large impinging signal intensity. Assuming a target BER of 10^{-3}, the achievable range is about 19 and 70 m for in coastal and clear waters, respectively. This small link range in coastal waters is because the optical signal suffers from high channel attenuation. Note that in an uncoded system, a BER of ~ 10^{-3} is sufficiently low and could further be reduced below 10^{-9} by applying efficient error correction codes [102].

3.3.4 Effect of Tx beam divergence

In Fig. 3.6, to study the effect of the beam divergence on the link performance, we have considered different values of the lambertain order m. Also, a concentrator lens with $\theta_{\mathrm{FoVr}} = 16°$ was considered at the Rx. Assuming a target BER of 10^{-3}, as expected, as m increases, the maximum achievable link range increases. At small m, the beam width is large (vice versa) and due to geometric loss from the beam spread most of the photons are lost before reaching the PD. It is also worthy of note the improvement on the achievable link range, owing to the gain of the concentrator lens. At a BER of 10^{-3} and $m = 45$, the link range is increased from about 70 m in Fig. 3.5 for clear waters with no concentrator lens to almost 105 m in Fig. 3.6.

3.3.5 Effect of Rx parameters

Figure 3.7 shows the effect of the Rx FoV on the link performance. For a target BER = 10^{-3}, we notice an improvement in terms of maximum achievable link distance when the Rx FoV is reduced

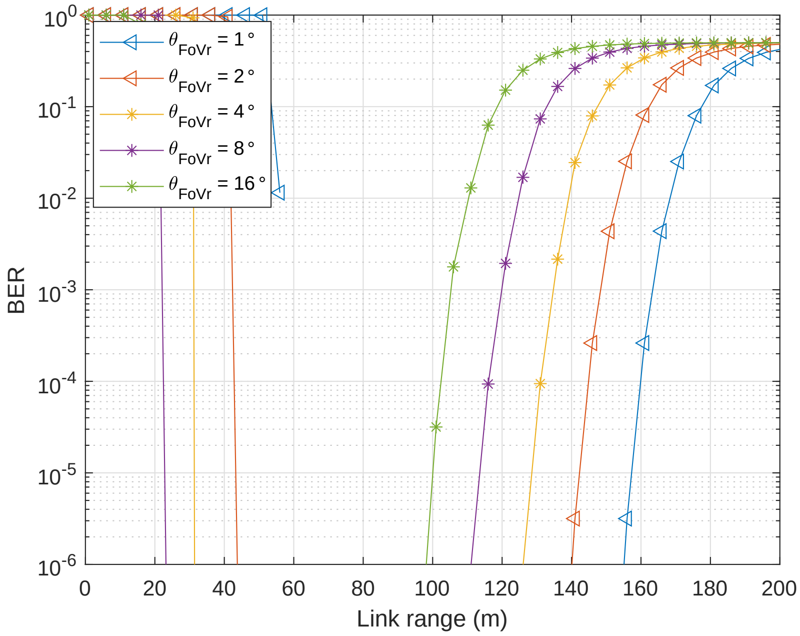

Figure 3.7: Effect of Rx FOV θ_{FoVr} on the link BER in clear waters. $P_{\mathrm{Tx},1} = 1$ W, uncoded OOK with $\xi = 0$, $T = 1\,\mu$s, $m = 45$, $A_{\mathrm{PD}} = 9\,\mathrm{mm}^2$.

from 16° to 1°. This behaviour is because of the increase in the optical concentrator gain $g(\theta)$ for smaller Rx FoV as can be seen from (3.13).

Further we have evaluated the impact of the PD physical area, A_{PD}, on the system performance in Fig. 3.8. Logically, the performance improves (i.e., the link range for a target BER increases) with increased A_{PD}.

3.4 Chapter summary

In this chapter, we discussed and showcased the potentials of utilizing SiPM based Rxs in UWOC applications. We gave a relatively detailed working principle of an SiPM and its associated parameters. The concept of the SiPM as a photon counter with photodetection modelled to follow a Poisson distribution, was also discussed. Further, we investigated the cause and effect of the nonlinear distortion of an SiPM. To further give a better understanding of the UWOC link performance for SiPM based Rxs, we presented some numerical results for a simple OOK modulation scheme. We showed the impact of clear and coastal waters on the system performance. We also showed the limitation due to nonlinear distortion that occurs in very short link ranges. Lastly, we briefly studied the effect of some Tx and Rx parameters on the link performance.

In some subsequent chapters, we will further discuss and exploit the effect of the appropriate setting of Tx and Rx parameters under various link conditions.

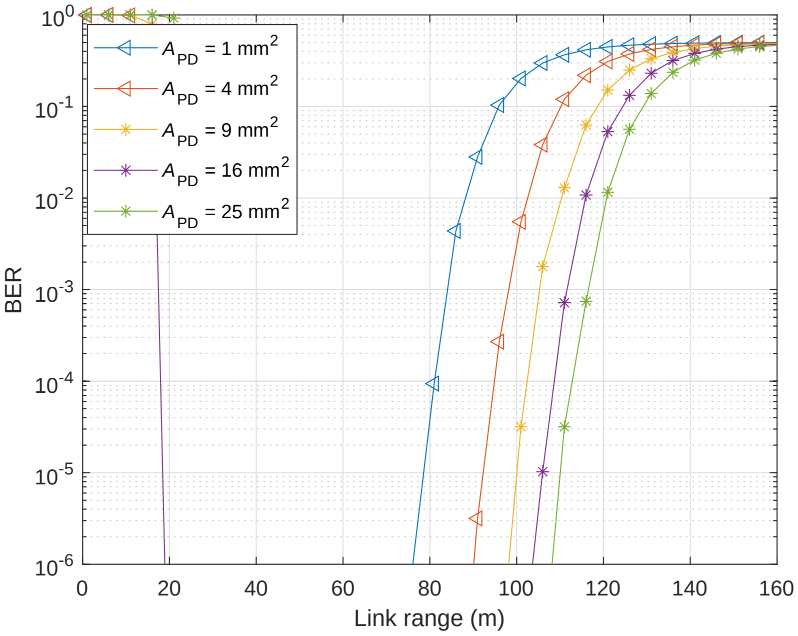

Figure 3.8: Effect of PD Area A_{PD} on the link BER in clear waters. $P_{\mathrm{Tx},1} = 1$ W, uncoded OOK with $\xi = 0$, $T = 1\mu$s, $m = 45$, $\theta_{\mathrm{FoVr}} = 16°$.

Chapter 4

Link misalignment and turbulence in UWOC

Contents

4.1 Introduction

Evidently, UWOC is a promising technology to meet the essential need for high-rate wireless data transmission in several technological applications, including installation monitoring, underwater robotics, port security, etc. These systems offer low implementation cost, low latency, high data rate, and energy efficiency, compared with the traditional acoustic communications [3, 103, 1, 104, 4]. However, in practice, the UWOC link performance is affected by several factors including water absorption and scattering [105, 68, 106, 66], solar background noise [19, 99], oceanic turbulence [107, 108, 109, 20], and pointing errors (PEs) [18, 74, 110, 111, 112, 113]. This has necessitated extensive research in the past few years in order to address these challenges of the UWOC technology [17]. It becomes necessary to investigate the effect of these factors on the transmitted signal quality so as to ascertain the reliability of the received signal.

Among the aforementioned challenges, this thesis is focused on link misalignments, which are particularly problematic in underwater applications where precise localization and tracking of mobile units is very challenging [17]. Another area of interest in this thesis is oceanic turbulence which induces intensity fading of the propagating optical signal due to fluctuations in the refractive index of the water from variations in pressure, temperature and salinity. Hence, in this chapter, we review the previous relevant works that have studied the impact of Tx-Rx misalignment and channel turbulence on the UWOC link performance. Furthermore, we focus on mitigation techniques that have been proposed in order to mitigate the resulting link performance degradation.

The subsequent discussions in this chapter are as follows. Section 4.2 explains the link misalignment problem, and further, consider its modeling for various link configurations and the proposed mitigation schemes. Next, Section 4.3 focuses on the effect of turbulence on UWOC links and presents the proposed approaches to reduce its effect. Lastly, Section 4.4 concludes the chapter and clarifies this thesis contribution regarding the modeling and minimizing of the effects of link misalignments and oceanic turbulence.

4.2 Link misalignments

Indeed, although the impact of beam misalignment and PEs is a well-explored topic in free-space optical (FSO) communications [114, 115], the past literature on UWOC systems mostly considered perfectly aligned line-of-sight (LOS) horizontal or vertical links [36, 60, 19]. However, maintaining the LOS link in an UWOC practical scenario is difficult due to the complexities of the underwater environment especially when considering mobile platforms. Also, link misalignment in underwater wireless optical links can considerably impact link reliability. Misalignments can be due to different phenomena in practical link deployment scenarios. For instance, for the case of communication with an underwater mobile unit, they can arise from its positioning inaccuracy or instability. Also, in the case of transmission from a fixed node, e.g., at the sea surface, they can be due to node movements as a result of surface waves, movement of other surface vehicles, etc. A simple concept of resolving link misalignment is through the tracking and positioning of the transceivers, but this comes at high implementation cost and system complexity, hence, making it challenging to maintain accurate pointing of the Tx and Rx link.

The fixed and random components of PEs are respectively, bore-sight, and jitter [116, 117]. Bore-sight is a fixed shift of the beam center from the detector center, whereas jitter is the random displacement of the beam center at the detector plane. Some works modeled the link misalignment in laser light source UWOC system using the beam spread function (irradiance distribution) [74, 111], which is suitable for small-angle approximation [118]. Particular interest in the evaluation, is the offset distance, which is between the centers of the Rx aperture and the beam at the Rx plane.

In [74], the investigation of the tolerable Rx offset distance to maintain a reliable communication was carried out, and further, a closed-form expression was developed, relating it to the transmit power and link range. Furthermore, for some special link configurations, e.g., a bottom-surface-bottom link in [119] or a surface-to-bottom link (see Fig. 4.1) in [111, 112], the link performance was evaluated taking into account the effect of the random sea surface, based on the

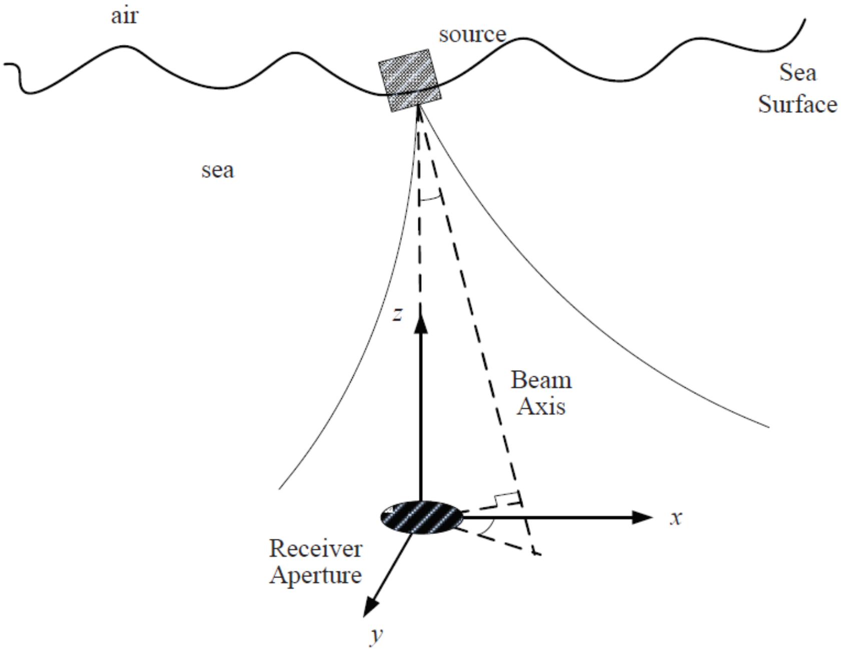

Figure 4.1: A surface-to-bottom link misalignment configuration (reproduced from [111]).

verified experimental model of [120].

Some other works that considered misalignment for UWOC links are [18], which gave a theoretical and experimental study of the effect of displacement in the Rx position and the inclination angle with respect to the main optical axis on the detected signal. Also, the impact of PEs on the BER and the capacity of an UWOC system were further studied in [121] and [122], respectively. Also, for the case of turbid waters, [123] studied the effect of Rx angular misalignments and its FoV on the received signal using a stochastic model. In turbid harbor waters, it has been observed that the dominant effect of scattering, resulting in beam spread, tends to relax the pointing requirements [1].

4.2.1 PE mitigation

Several schemes have been deployed so as to minimize the pointing requirement in UWOC links. One simple solution could be to use a large Rx aperture and consequently a wide FoV, but this comes at a high cost, bulkiness, and little implementation flexibility. Another approach could be the designing of intelligent systems to track and point the transceivers, as proposed in [75]. Therein, Txs are quasi-omnidirectional and can estimate the water quality from the backscattered light captured by an adjacent Rx. Also, the Rxs use FoV and have the capability of estimating the angle of arrival of signals, to further align the FoV using the electronic beam steering mechanism.

Also, modulating retro-reflectors (MRRs) can be deployed to relax pointing accuracy by retro-reflecting the modulated light back to the interrogating source [1]. Some demonstrations have been carried-out for MRRs based on ferro-electric liquid crystals [124], micro-electro-mechanical

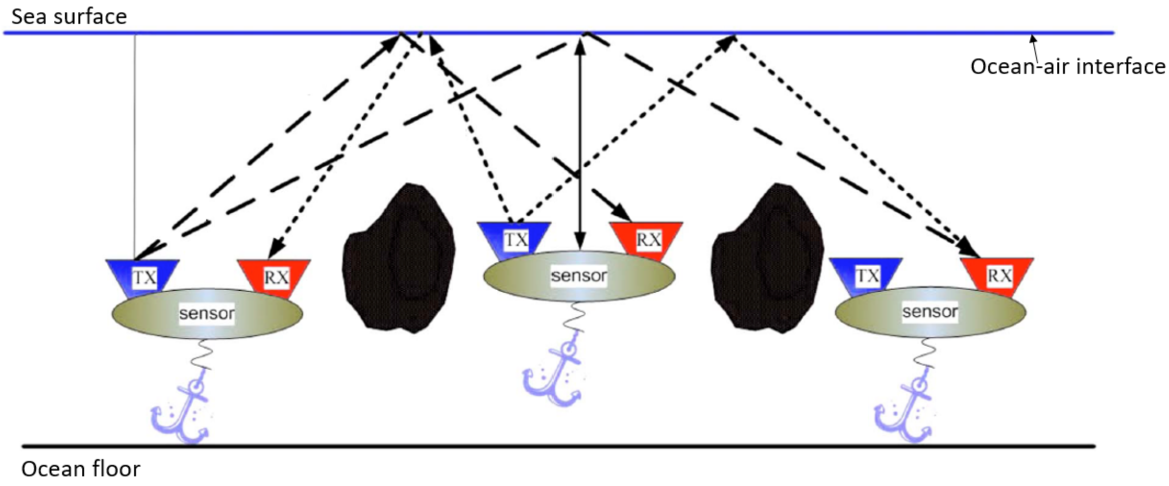

Figure 4.2: Link misalignment mitigation with NLOS strategy (reproduced from [119]).

systems [125], and multiple quantum well [126] electro-absorption modulators. The use of spatial light modulators in MRRs can aid in steering the optical beam, beam shaping or adaptive optics [1].

In a non line-of-sight (NLOS) communication scenario, a diffusive reflector, such as the ocean-air interface implemented in [119], can be used to minimize the impact of link misalignment, especially in broadcasting to multiple Rxs (see Fig. 4.2). However, due to the increase in the geometric loss from beam spreading, a diffuse NLOS link, as observed in [127] for clear waters, would require additional transmit optical power to achieve the same signal level at the Rx compared to a collimated source. Also in [128], the performance of a NLOS UWOC system was evaluated with the consideration of a static or a dynamic channel model. More recently, [129, 113] proposed an angular MIMO technique for relatively short UWOC links to relax the beam alignment requirements.

Another approach for improving the UWOC system performance of a link subject to misalignment, is the appropriate selection of the system parameters [110, 76, 39]. The effect of beam divergence angle on the received power was investigated in [110], taking into consideration the Tx-Rx lateral offset. Also, [76] studied the optimum divergence angle of a Gaussian beam required to reduce the Tx-Rx misalignment effect. In a recent work [39], we studied the effect of Tx-Rx parameter optimization on the performance of a vertical UWOC link subject to PEs.

4.3 Oceanic turbulence

As aforementioned, oceanic turbulence is another factor that can degrade the performance of an UWOC link considerably. Turbulence causes random fluctuations in the intensity and the phase of an optical signal (scintillations) at the Rx and also causes link misalignments [130, 131]. These fluctuations are a result of variations in the refractive index of water, which can be due to changes in water density, salinity and temperature, or air bubbles in the aquatic channel.

For most practical cases, we experience the weak turbulence regime. Under these conditions, the variations in the received signal intensity I, with mean I_0, at some point in the detector plane can be represented so as to follow a lognormal distribution [1]:

$$f_I(I) = \frac{1}{I\sqrt{2\pi\sigma_I^2}} \exp\left(-\frac{\left(\ln(I/I_0) + \sigma_I^2/2\right)^2}{2\sigma_I^2}\right), \tag{4.1}$$

where σ_I^2 is the scintillation index of the received signal intensity. It can be expressed as:

$$\sigma_I^2 = \frac{\langle I^2\rangle - \langle I\rangle^2}{\langle I\rangle^2} = \frac{\langle I^2\rangle}{\langle I\rangle^2} - 1, \tag{4.2}$$

where $\langle\cdot\rangle$ denotes the average.

A number of recent works have investigated the effect of oceanic turbulence on the performance UWOC links. It is worthy to note that turbulence has varying impacts on coherent and non-coherent light sources, with fewer research works on the latter. An experimental demonstration was done in [40] to showcase the effect turbulence has on an optical signal from coherent and non-coherent light sources, with the latter being less affected by the change in temperature. In another experimental work in [132], the effect of surface currents and tides was investigated. Also, [133] studied the effects of turbulence on the Rx SNR of an UWOC system. Taking into account air bubbles and the temperature gradient, [109] proposed a unified statistical model based on experimental data to characterize the turbulence. In the case of a vertical UWOC link, [20] proposed modeling the optical channel by several layers with uniform thickness but of different turbulent strengths (see Fig. 4.3). In fact, this proposed approach recognizes that oceanic temperature and salinity profiles are not smooth functions of the depth but rather change in a step-wise manner. This way, weak gradient layers with a thickness on the order of meters are separated by strong gradient sheets with a thickness on the order of centimeters [134]. Similarly for an inhomogeneous vertical link, [135] evaluated the link performance considering a cascaded turbulence effect from air bubbles and temperature.

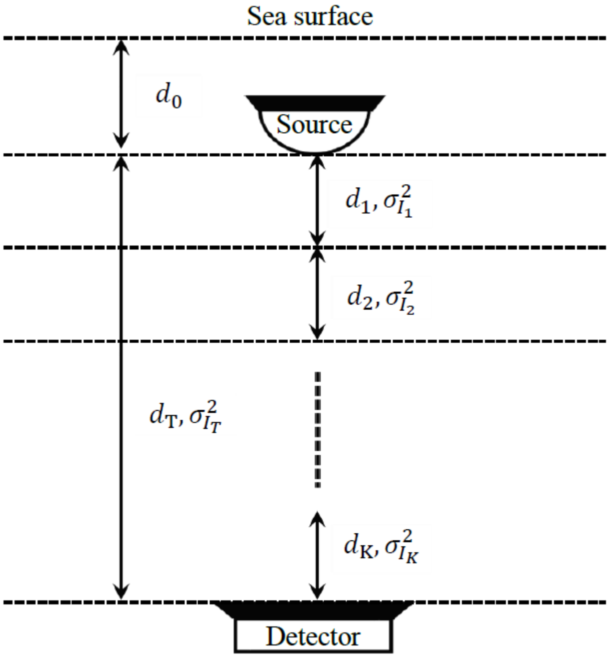

Figure 4.3: An inhomogeneous vertical underwater link subject to turbulence (reproduced from [20]).

4.3.1 Turbulence mitigation

To reduce the effect of turbulence, the choice of system parameters and aperture averaging was studied in [136] considering a Gaussian beam under weak oceanic turbulence. Also, [137] studied the improvement in the scintillation index by using adaptive optics and aperture averaging. The effect of aperture averaging on the average link BER performance subject to moderate to strong oceanic turbulence was investigated in [71]. Also, [138] considered the effect of Tx-Rx parameters on the UWOC link performance under different turbulence conditions. Given in Fig. 4.4 is an illustration of an UWOC system subject to oceanic turbulence and employing a Gaussian lens at the plane to perform aperture averaging.

Furthermore, some works have suggested turbulence mitigation through link parameter adaptation, especially at the Tx, based on the channel conditions. In [139] (also related to [140]), adaptive modulation schemes were considered for improving an UWOC link affected by absorption, scattering, and weak turbulence. The concept of adaptive beam shaping was proposed and experimentally demonstrated in [141] for enhancing the UWOC link. Also in a more recent work, assuming the availability of adequate information on the channel state at the Tx without a feedback loop from the Rx side, a feedback-free adaptive modulation selection algorithm was proposed in [142] for a free-space optical (FSO) system, which could be readily implemented in an UWOC system.

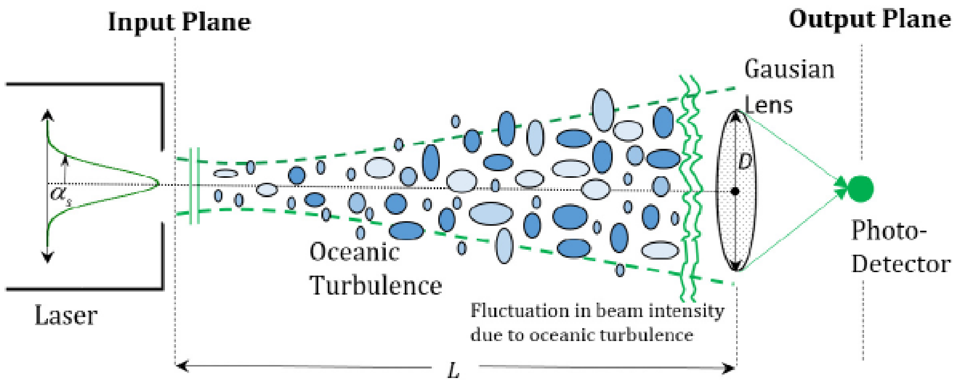

Figure 4.4: An UWOC link subject to oceanic turbulence with a Gaussian lens for aperture averaging (reproduced from [136]).

4.4 Chapter summary

In this chapter, we presented a brief state of the art on link misalignment and oceanic turbulence in UWOC systems. The impact of PEs on different link configurations have been considered by various works; some of them have proposed the optimization of system parameters as a way of minimizing their effect. Oceanic turbulence has been investigated for both horizontal and vertical links, of which the latter has relatively few literature so far. Most works have suggested using a large Rx aperture (compared to the coherence length of the beam) to reduce the fading effect.

In the subsequent chapters, we investigate channel modeling and mitigation techniques to deal with PEs and turbulence in a typical vertical UWOC link.

Chapter 5

Impact of misalignment on LED-based vertical UWOC link performance

Contents

5.1 Introduction

In the previous chapter, we have discussed the study of various works on the impact of link misalignment on UWOC system performance. Herein, we will investigate the effect of Tx-to-Rx misalignment for a vertical link considering both downlink and uplink communication. More specifically, in our case study, communication takes place between a buoy at the water surface and an AUV beneath it, as illustrated in Fig. 5.1. The typical application is in high-speed data transfer from a sea surface observation station to an AUV (download mode), or transmitting the collected data by an AUV to a surface station for further long-range through-the-air transmission (upload mode), e.g., for data muling. The position and orientation of the buoy in this scenario are subject to sea surface waves, while those of the AUV are subject to water currents and AUV instability in its *dynamic* positioning (i.e., static position, used when establishing a communication link with the buoy).

We consider a typical scenario for an UWOC link, employing LEDs at the Tx and a high-sensitivity PD, i.e., an SiPM at the Rx. The interest of using LEDs is their relatively high output power and the flexibility of being arranged in arrays to further increase the transmit power, and hence, the link span [27, 62]. Also, the SiPM, which is an array of Geiger mode biased APDs (SPADs), offers the advantages of high sensitivity, low implementation complexity, low operating bias voltage, mechanical robustness, and magnetic fields insensitivity, as compared to the PMT counterparts [36, 62, 88].

Further, we will consider optimization of the Tx and the Rx parameters to improve the link performance in terms of outage probability P_{out}. Several works in FSO, and indoor optical wireless communication (OWC) systems have employed this strategy, and given the substantially different beam propagation (including scattering), channel characteristics, Tx-Rx types, and operational particularities between FSO, and UWOC systems, there is the need for a unique study into the optimization of UWOC link parameters, which constitutes our motivation in using this approach. Our aim is to focus on the system design for UWOC links corrupted by misalignments in order to minimize their impact on the link performance. Specifically, the main parameters that we consider here are the Tx beam divergence and the Rx FoV.

To the best of our knowledge, the study of UWOC link optimization for a limited Rx FoV with a high-sensitivity PD has not been considered in the literature thus far. We provide an accurate and computationally efficient analytical framework for the evaluation of the link performance in terms of the BER and the P_{out}. This is based on precise mathematical modeling of angular misalignments and displacements of the AUV, as well as the angular misalignments at the buoy resulting from the sea surface waves. We show that careful selection of the Tx beam divergence and the Rx FoV allows significant performance improvement and substantially improved link reliability. Obviously, the link reliability can be further improved using powerful channel coding and/or more energy-efficient modulation techniques [143, 144].

The subsequent presentation of this chapter is as follows. Section 5.2 introduces the con-

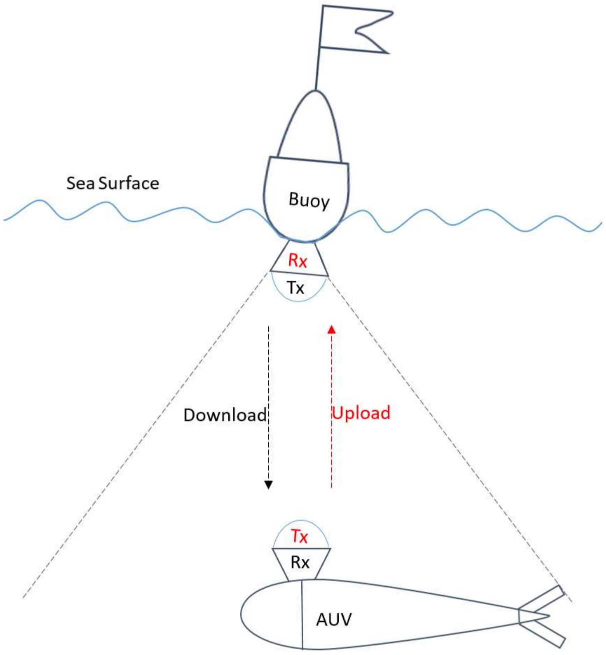

Figure 5.1: Buoy-AUV illustration of the considered UWOC link.

sidered UWOC link configuration and the related main assumptions. In Section 5.3, we present mathematical modeling for pointing errors. Next, in Section 5.4, the derivation of the distribution of channel coefficient is provided for the considered link configuration. Then, a set of numerical results are presented in Section 5.5 to show the performance improvement achieved by Tx-Rx parameter optimization. Lastly, Section 5.6 concludes the paper.

Notations: Boldface capital letters are used for matrices and boldface small letters for vectors. Also, $(.)^{\mathrm{T}}$ stands for transposition, $||.||$ is the Euclidean norm, $\boldsymbol{a}\cdot\boldsymbol{b}$ denotes the dot product of vectors $\boldsymbol{a}$ and $\boldsymbol{b}$, and $\delta(.)$ stands for the Dirac delta function. In addition, $\Pr(.)$ denotes probability, and $\operatorname{erfc}(x) = \frac{2}{\sqrt{\pi}}\int_x^\infty e^{-t^2}dt$ and $Q(x) = \frac{1}{2}\operatorname{erfc}(x/\sqrt{2})$ are the well-known complementary error function and Q-function, respectively. Lastly, $\operatorname{sgn}(x)$ is the sign function, which equals 1 for $x \geq 0$ and -1 otherwise.

5.2 Assumptions and performance metrics

For the sake of brevity, we provide in the following the system model for the case of downlink transmission for the link configuration shown in Fig. 5.1, when the Tx is located at the buoy and the Rx at the AUV. The general block diagram of the communication link is shown in Fig. 5.2.

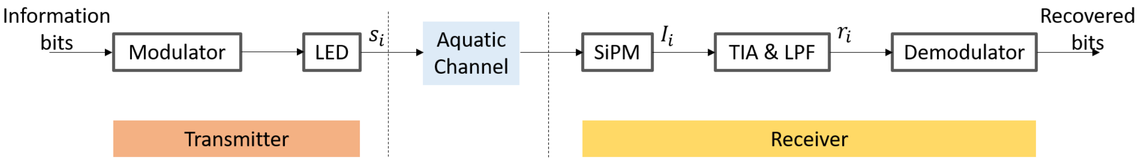

Figure 5.2: The block diagram of the UWOC communication link.

5.2.1 Signal transmission modeling

Figure 5.3 shows the corresponding link geometry, where the Rx is located at depth D, exactly beneath the Tx (i.e., when there is no displacement between the Tx and the Rx). The link distance L is then equal to D. At the Tx, the LED is assumed to follow a Lambertian model with order m, which specifies the optical beam directionality (see Section 3.3.1) [97]. At the Rx, the active area of the PD A_{PD} has the effective Rx light collection area A_{eff} given in (3.12) [97].

For a given transmit optical power P_{Tx}, the received intensity P_{Rx} on the PD can then be expressed as [101]:

$$P_{\text{Rx}} = P_{\text{Tx}} \frac{m+1}{2\pi} \cos^m(\phi_{\text{t}})\, e^{-(L\,K_{\text{d}})} \frac{A_{\text{eff}}(\phi_{\text{r}})}{L^2}\, \Pi\left(\frac{\phi_{\text{r}}}{\phi_{\text{FoVr}}}\right) \tag{5.1}$$

where, $\phi_{\text{t}} \in \left\{\frac{-\pi}{2}, \frac{\pi}{2}\right\}$ is the angle of irradiance at the Tx. We have used the definition of $\Pi(u) = 1$ if $u \leq 1$, and zero otherwise, which allows accounting for link interruption when the beam incident angle falls out of the Rx FoV.

We define the aggregate channel coefficient, which includes the effects of the Tx, the Rx, and the aquatic channel as:

$$h = P_{\text{Rx}} / P_{\text{Tx}}. \tag{5.2}$$

In general, h is a random variable due to channel turbulence and Tx-Rx random misalignments.

As we use an LED at the Tx, we consider IM/DD for signal transmission. Without loss of generality, the NRZ OOK is considered. At the Rx, the generated photo-current at the SiPM output is passed through a trans-impedance amplifier (TIA) followed by a low-pass filter (LPF) to limit the thermal noise variance (see Fig. 5.2).

The transmitted OOK signal s_i, $i \in \{0,1\}$, takes two values of P_{Tx_0} and P_{Tx_1}, given the average transmitted optical power P_{Tx} and the extinction ratio, defined as $\xi = P_{\text{Tx}_0} / P_{\text{Tx}_1}$. The generated photo-current I_i at the SiPM output is:

$$I_i = \underbrace{\mathcal{R}_{\text{e}}\, s_i\, h}_{I_{s,i}} + I_d + n_{s_i} = \check{I}_i + n_{s_i}, \tag{5.3}$$

where $I_{s,i}$ represents the useful signal, $\mathcal{R}_{\text{e}}$ is the SiPM responsivity (3.4), I_d is the dark current (3.6), and n_{s_i} is the photo-current noise, including background noise, shot noise, and dark current noise. Also, $\check{I}_i = I_{s,i} + I_d$, which includes the constant component of the dark current.

Denote the signal (voltage) at the LPF output by r_i:

$$r_i = R_\mathrm{L}\, I_i + n_\mathrm{th} = \underbrace{R_\mathrm{L}\, \check{I}_i}_{\check{r}_i} + R_\mathrm{L}\, n_{s_i} + n_\mathrm{th} \tag{5.4}$$

with R_L being the load resistance of the TIA, and n_th denotes the thermal noise component in r_i, arising from the TIA and LPF circuitry (mainly related to R_L). The corresponding total noise variance $\sigma^2_{n_i}$ (in units of V^2) is given by:

$$\sigma^2_{n_i} = R^2_\mathrm{L}\, (\sigma^2_{n_{s_i}} + \sigma^2_\mathrm{th}) = R^2_\mathrm{L}\, (\sigma^2_{\mathrm{sh},i} + \sigma^2_\mathrm{d} + \sigma^2_\mathrm{b}) + \sigma^2_\mathrm{th}, \tag{5.5}$$

where $\sigma^2_{\mathrm{sh},i}$, σ^2_d, σ^2_b, and σ^2_th (in V^2) denote the variances of the signal shot noise, dark noise, background noise, and thermal noise, respectively, where,

$$\begin{cases} \sigma^2_{\mathrm{sh},i} & = & 2\, e\, G\, F\, B\, I_{s,i}, \\ \sigma^2_\mathrm{d} & = & 2\, e\, G\, F\, B\, I_\mathrm{d}, \\ \sigma^2_\mathrm{th} & = & 4\, K_\mathrm{Z}\, T\, B\, R_\mathrm{L}. \end{cases} \tag{5.6}$$

Here, K_Z, T, F, and B denote the Boltzmann constant, the Rx equivalent temperature in Kelvin, the PD excess noise factor, and the BW of the Rx LPF, respectively. Let $B \approx R_\mathrm{b}/2$, with R_b being the bit rate [145].

In this work, channel delay dispersion is neglected, which is valid in practice when working in low-to-moderate turbidity waters [68, 66]. Also, we neglect the channel turbulence, which implies that sea currents and the gradient of salinity and temperature variations are considered negligible. Furthermore, for simplicity, we will neglect the effect of background noise from solar radiations, i.e., we set $\sigma^2_\mathrm{b} \approx 0$. In fact, considering a worst-case scenario, with a relatively high level of radiation when the sun is at zenith and assuming no shadowing for a vertical downlink transmission, [60] showed that an SiPM-based Rx is highly impacted by the background noise in relatively shallow waters, despite using a narrow-band optical filter. However, in our considered scenario, these worst-case conditions are not likely to happen: the more critical case is the downlink (from the buoy-based Tx to the AUV Rx), where the buoy installation would shadow the sunlight, for example, when the sun is at the zenith. For the uplink case, the Rx performance could be limited by the laterally-diffused sunlight in water. However, the major part of this noise can be rejected by using a spatial filter at the buoy Rx.

5.2.2 Performance evaluation

Given that channel variations due to misalignments occur at a much slower rate than the link bit-rate, the channel is modeled as non-ergodic for which the outage probability P_out is an appropriate performance metric. This P_out is defined as the probability that the link BER exceeds a target BER. We further consider the probability of link interruption P_int as the probability that the incident angle of the incoming beam at the Rx falls outside the Rx FoV, i.e., $\phi_\mathrm{r} > \phi_\mathrm{FoVr}$. Notice that interruption events are included in outage.

Recall that we consider NRZ-OOK modulation scheme. We do not consider any channel coding [143] in this work. We assume the Rx has perfect knowledge of the random channel attenuation coefficient h, based on which it sets the optimal detection threshold for signal demodulation.[1] Note from the previous subsection that, an important point is that the Rx noise is signal-dependent, given the use of an SiPM PD. The instantaneous BER $P_e(e|h)$ can be written as [147]:

$$P_e(e|h) = \frac{1}{4}\text{erfc}\left(\frac{\gamma_{\text{th}} - \check{r}_0}{\sqrt{2\sigma^2_{n_0}}}\right) + \frac{1}{4}\text{erfc}\left(\frac{\check{r}_1 - \gamma_{\text{th}}}{\sqrt{2\sigma^2_{n_1}}}\right), \tag{5.7}$$

where γ_{th} stands for the optimal detection threshold, and $\check{r}_0$ and $\check{r}_1$ denote the signals input to the demodulator, corresponding to bits '0' and '1', respectively. The corresponding noise variances are denoted by $\sigma^2_{n_0}$ and $\sigma^2_{n_1}$, calculated from (5.5). The optimal threshold γ_{th} is calculated as [147]:

$$\gamma_{\text{th}} = \frac{\check{r}_0\sigma^2_{n_1} - \check{r}_1\sigma^2_{n_0}}{\sigma^2_{n_1} - \sigma^2_{n_0}} + \left[\frac{\check{r}_1^2\sigma^2_{n_0}}{\sigma^2_{n_1} - \sigma^2_{n_0}} + \left(\frac{\check{r}_0\sigma^2_{n_1} - \check{r}_1\sigma^2_{n_0}}{\sigma^2_{n_1} - \sigma^2_{n_0}}\right)^2 - \frac{\check{r}_0^2\sigma^2_{n_1}}{\sigma^2_{n_1} - \sigma^2_{n_0}} - \frac{\sigma^2_{n_0}\sigma^2_{n_1}}{\sigma^2_{n_1} - \sigma^2_{n_0}}\ln\left(\frac{\sigma^2_{n_0}}{\sigma^2_{n_1}}\right)\right]^{0.5}. \tag{5.8}$$

The average BER[2] can then be calculated as:

$$P_e = \int_0^{\infty} f_h(h)\,P_e(e|h)\,dh, \tag{5.9}$$

where $f_h(h)$ is the probability density function (PDF) of h. Also, the outage probability can be defined as:

$$P_{\text{out}} = \Pr(h < h_{\text{th}}) = \int_0^{h_{\text{th}}} f_h(h)\,dh, \tag{5.10}$$

where h_{th} is defined so that $\text{BER}_{\text{th}} = P_e(e|h_{\text{th}})$. Lastly, the link interruption probability is:

$$P_{\text{int}} = \Pr\left(\phi_{\text{r}} > \phi_{\text{FoVr}}\right). \tag{5.11}$$

5.2.3 Analytical outage probability calculation

As will be explained in Section 5.5, the link performance can be evaluated through a statistical Monte Carlo (MC) approach. Obviously, there is interest to calculate these quantities analytically to avoid timely MC simulations. We provide here details on the derivation of the average BER and the outage probability. Whereas closed form expressions can readily be derived for the case of using a simple PIN PD [111], [148], the signal dependent noise in our case (resulting in a complex form for $P_e(e|h)$ and for the optimal detection threshold γ_{th} in (5.7) and (5.8)) and the relatively complex expressions for the PDF of h (as will be shown later in Section 5.4) make derivation of closed form expressions for P_{out} very complex. For this reason, we propose here to make some

---

[1] Note that this is a quite reasonable assumption since the channel varies slowly with respect to the bit duration, and can easily be estimated using pilot symbols [146].

[2] Although our channel is non-ergodic and the appropriate metric is the outage probability, P_e is also given for the sake of completeness.

simplifying assumptions. Firstly, we assume that the shot noise $R_{\mathrm{L}}^2\sigma_{\mathrm{sh},i}^2$ in (5.4) is the dominant noise factor at the Rx. This implies that we have a large PD gain G (which is actually the case), and that for OOK signaling, a relatively large[3] extinction ratio ξ is used, which implies that even for "off" OOK symbols, the thermal and dark noises are negligible, compared with the corresponding signal-dependent shot noise. As a result, given that $I_{s,0} = \xi\, I_{s,1}$, we set $\check{r}_0 \approx \xi\, \check{r}_1$ and also $\sigma_{n_0}^2 \approx \xi\, \sigma_{n_1}^2$. Then, considering optimal thresholding for signal detection, the error probability in (5.7) can be simplified as:

$$P_e(e|h) = \frac{1}{2}\mathrm{erfc}\left(\frac{R_{\mathrm{L}}\, I_{s,1} - \gamma_{\mathrm{th}}}{\sqrt{2\,\sigma_{n_1}^2}}\right) = Q\left(\frac{R_{\mathrm{L}}\, I_{s,1} - \gamma_{\mathrm{th}}}{\sqrt{\sigma_{n_1}^2}}\right). \tag{5.12}$$

Also, with the considered approximations, the expression of γ_{th} in (5.8) can be simplified as follows:

$$\gamma_{\mathrm{th}} = R_{\mathrm{L}}\sqrt{\xi\, I_{s,1}^2 - \frac{\xi\,\sigma_{n_1}^2}{1-\xi}\log\xi} \approx R_{\mathrm{L}}\, I_{s,1}\sqrt{\xi} \tag{5.13}$$

Now, to calculate P_{out} for a given h_{th} (which corresponds to a $\mathrm{BER}_{\mathrm{th}}$), we have $\sigma_{n_1}^2 = R_{\mathrm{L}}^2(2\,eGFB\,\mathcal{R}_{\mathrm{e}} s_1\, h_{\mathrm{th}} + \sigma_{\mathrm{d}}^2) + \sigma_{\mathrm{th}}^2$ and $I_{s,1} = \mathcal{R}_{\mathrm{e}}\, s_1\, h_{\mathrm{th}}$. Then, from (5.12) we can define:

$$\mathcal{A} \triangleq Q^{-1}(\mathrm{BER}_{\mathrm{th}}) = \frac{R_{\mathrm{L}}\,\mathcal{R}_{\mathrm{e}}\, s_1\, h_{\mathrm{th}} - R_{\mathrm{L}}\,\mathcal{R}_{\mathrm{e}}\, s_1\, h_{\mathrm{th}}\sqrt{\xi}}{\sqrt{R_{\mathrm{L}}^2(2\,eGFB\,\mathcal{R}_{\mathrm{e}}\, s_1\, h_{\mathrm{th}} + \sigma_{\mathrm{d}}^2) + \sigma_{\mathrm{th}}^2}} \tag{5.14}$$

$\mathcal{A}$ can be calculated, for instance, using the Matlab *qfuncinv* function [149]. We also define for notation simplicity $\mu = R_{\mathrm{L}}\,\mathcal{R}_{\mathrm{e}}\, s_1$ and $\beta = 2\,eR_{\mathrm{L}}GBF\mu$. We can then rewrite (5.14) as:

$$\mathcal{A} = \frac{\mu\, h_{\mathrm{th}}(1-\sqrt{\xi})}{\sqrt{\beta\, h_{\mathrm{th}} + R_{\mathrm{L}}^2\sigma_{\mathrm{d}}^2 + \sigma_{\mathrm{th}}^2}} \tag{5.15}$$

It can be easily shown that h_{th} can be calculated from the following equation:

$$h_{\mathrm{th}} = \frac{\mathcal{B} + \sqrt{\mathcal{B}^2 + 4\,\mathcal{D}\mathcal{C}}}{2\,\mathcal{D}}, \tag{5.16}$$

where $\mathcal{B} = \mathcal{A}^2\,\beta$, $\mathcal{C} = \mathcal{A}^2\,(R_{\mathrm{L}}^2\sigma_{\mathrm{d}}^2 + \sigma_{\mathrm{th}}^2)$, and $\mathcal{D} = \mu^2\left(1-\sqrt{\xi}\right)^2$. The accuracy of this approach will later be quantified by numerical results in Section 5.5.

5.3 Pointing error modeling

Consider the downlink configuration as the default case, i.e., when the Tx is on the buoy and the Rx is on the AUV. For the mathematical derivations, we assume that the buoy's position is nearly fixed, whereas its orientation is primarily affected by the surface waves as a result of wind. The

---

[3] We have verified by numerical simulations that the obtained solution is quite accurate for $\xi \gtrsim 30\%$, and even provides a good accuracy for ξ as small as $\sim 10\%$.

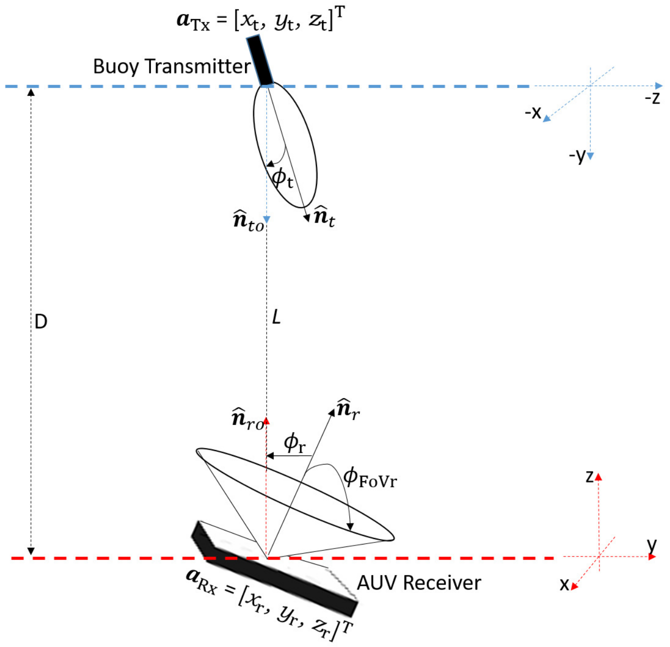

Figure 5.3: Geometry of the buoy-AUV downlink UWOC system (inspired from [97]).

orientation of the Rx is deviated by underwater currents and the instability of the AUV, whereas its displacement is due to positioning inaccuracies. To account for pointing errors, we consider the perfect alignment case when the AUV is exactly beneath the buoy and there is no orientation deviation with respect to the optical axis. Figure 5.3 illustrates the scenario where there is no position displacement between the Tx and the Rx but there are orientation deviations at both the Tx and the Rx with respect to the optical axis. A more general scenario is illustrated in Fig. 5.4, where there is also a position displacement of the Rx with respect to the Tx.

Consider the more general misalignment case as illustrated in Fig. 5.4. Under perfect Tx-Rx alignment, denote the normal vectors to the Tx and the Rx by $\hat{\boldsymbol{n}}_{to}$ and $\hat{\boldsymbol{n}}_{ro}$, respectively, where $\hat{\boldsymbol{n}}_{to} = [0, 0, -1]^{\mathrm{T}}$ and $\hat{\boldsymbol{n}}_{ro} = [0, 0, 1]^{\mathrm{T}}$. Under misaligned beam conditions, these normal vectors are denoted by $\hat{\boldsymbol{n}}_t$ and $\hat{\boldsymbol{n}}_r$, respectively. Let θ_{t} denote the polar angle between $\hat{\boldsymbol{n}}_{to}$ and $\hat{\boldsymbol{n}}_t$, and φ_{t} the azimuthal angle to $\hat{\boldsymbol{n}}_t$. Similarly, the polar and azimuthal angles of the Rx are denoted by θ_{r} and φ_{r}, respectively. Like in Fig. 5.3, here, ϕ_{t} and ϕ_{r} denote the polar angles with respect to the optical axis. We have:

$$\cos\left(\phi_{\mathrm{t}}\right) = \frac{\hat{\boldsymbol{n}}_t \cdot (\boldsymbol{a}_{\mathrm{Rx}} - \boldsymbol{a}_{\mathrm{Tx}})}{||\boldsymbol{a}_{\mathrm{Rx}} - \boldsymbol{a}_{\mathrm{Tx}}||}, \tag{5.17}$$

$$\cos\left(\phi_{\mathrm{r}}\right) = \frac{\hat{\boldsymbol{n}}_r \cdot (\boldsymbol{a}_{\mathrm{Tx}} - \boldsymbol{a}_{\mathrm{Rx}})}{||\boldsymbol{a}_{\mathrm{Tx}} - \boldsymbol{a}_{\mathrm{Rx}}||} \tag{5.18}$$

where $||\boldsymbol{a}_{\mathrm{Tx}} - \boldsymbol{a}_{\mathrm{Rx}}|| = L$. Denote the Cartesian coordinates of the Tx and the Rx by vectors $\boldsymbol{a}_{\mathrm{Tx}} = [x_{\mathrm{t}}, y_{\mathrm{t}}, z_{\mathrm{t}}]^{\mathrm{T}}$ and $\boldsymbol{a}_{\mathrm{Rx}} = [x_{\mathrm{r}}, y_{\mathrm{r}}, z_{\mathrm{r}}]^{\mathrm{T}}$, respectively. Also, without loss of generality, in the following, consider the buoy's position as the origin of the Cartesian coordinates, i.e., $\boldsymbol{a}_{\mathrm{Tx}} = [0, 0, 0]^{\mathrm{T}}$. Note that when there is no Rx displacement, like in Fig. 5.3, we have $\phi_{\mathrm{t}} = \theta_{\mathrm{t}}$ and $\phi_{\mathrm{r}} = \theta_{\mathrm{r}}$.

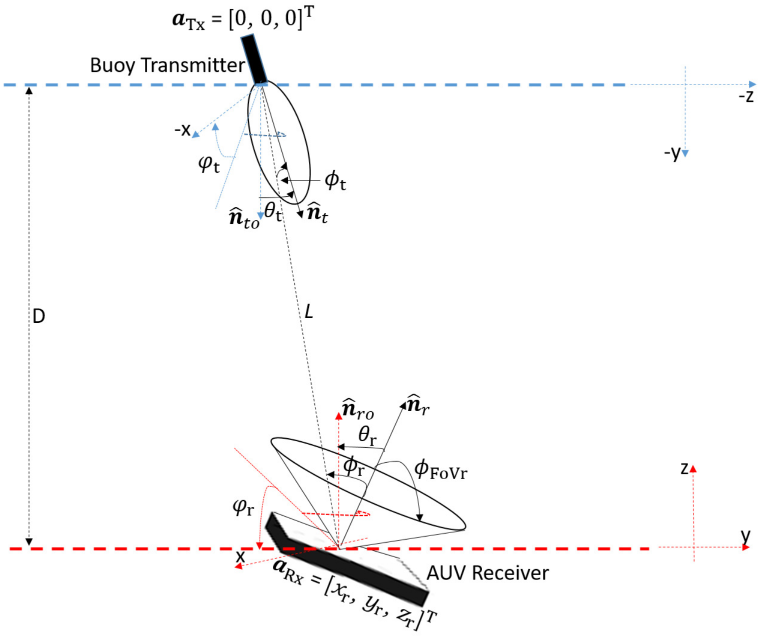

Figure 5.4: Transmitter and Receiver with Orientation and Position Deviations (inspired from [97]).

5.3.1 Modeling Tx orientation

The buoy at the sea surface swerves as the wind blows across it from different directions. A set of experimental measurements were carried out in [120] to measure the sea surface slope. Close linearity was then deduced between the variance of sea surface slopes and the wind speed U for an approximate range of 1 m/s $< U <$ 14 m/s. This model was later validated in [150] based on a derived and experimentally validated omni-directional wind-dependent sea surface spectrum. It was adopted in [111, 112] for a buoy-based vertical UWOC link, where the distribution of the random sea surface slope was expressed in terms of spherical coordinates as follows:

$$f_{\theta_t,\varphi_t}(\theta_t,\varphi_t) = \frac{\tan(\theta_t)\sec^2(\theta_t)}{2\pi\sigma_u^2}\exp\left(\frac{-\tan^2(\theta_t)}{2\sigma_u^2}\right), \tag{5.19}$$

where the variance σ_u^2 of the omni-directional sea surface slope (which is independent of the wind direction) is given by [120]:

$$\sigma_u^2 = 0.003 + 0.00512\,U \pm 0.004, \tag{5.20}$$

with U being in units of m/s. Note that in (5.19), φ_t is assumed to be uniformly distributed between 0 and 2π.

5.3.2 Modeling Rx orientation and displacement

We model the orientation of the Tx and the Rx by a rotation matrix $\boldsymbol{R}$ applied to their initial vectors $\hat{\boldsymbol{n}}_{to}$ and $\hat{\boldsymbol{n}}_{ro}$ (corresponding to the perfect link alignment, see Fig. 5.3), respectively [151]. This way,

$\hat{\boldsymbol{n}}_t = \boldsymbol{R}\hat{\boldsymbol{n}}_{to}$, and $\hat{\boldsymbol{n}}_r = \boldsymbol{R}\hat{\boldsymbol{n}}_{ro}$. Matrix $\boldsymbol{R}$ accounts for rotations around z, x, and y axes (yaw γ, pitch α, and roll β) through rotation matrices $\boldsymbol{R}_\gamma$, $\boldsymbol{R}_\alpha$, and $\boldsymbol{R}_\beta$, respectively:

$$\boldsymbol{R}_\gamma = \begin{bmatrix} \cos\gamma & -\sin\gamma & 0 \\ \sin\gamma & \cos\gamma & 0 \\ 0 & 0 & 1 \end{bmatrix}, \boldsymbol{R}_\alpha = \begin{bmatrix} 1 & 0 & 0 \\ 0 & \cos\alpha & -\sin\alpha \\ 0 & \sin\alpha & \cos\alpha \end{bmatrix}, \boldsymbol{R}_\beta = \begin{bmatrix} \cos\beta & 0 & \sin\beta \\ 0 & 1 & 0 \\ -\sin\beta & 0 & \cos\beta \end{bmatrix},$$

Here, α and β represent the sea surface slope effect from the up/downwind and the crosswind directions [120].

Given $\hat{\boldsymbol{n}}_{to} = [0, 0, -1]^{\mathrm{T}}$, $\hat{\boldsymbol{n}}_t$ can be written as:

$$\hat{\boldsymbol{n}}_t = \boldsymbol{R}\hat{\boldsymbol{n}}_{to} = \boldsymbol{R}_\gamma \boldsymbol{R}_\alpha \boldsymbol{R}_\beta \hat{\boldsymbol{n}}_{to} = \begin{bmatrix} -\cos\beta\sin\gamma\sin\alpha - \cos\gamma\sin\beta \\ \cos\gamma\cos\beta\sin\alpha - \sin\gamma\sin\beta \\ -\cos\alpha\cos\beta \end{bmatrix} = \begin{bmatrix} -\sin\theta_{\mathrm{t}}\cos\varphi_{\mathrm{t}} \\ -\sin\theta_{\mathrm{t}}\sin\varphi_{\mathrm{t}} \\ -\cos\theta_{\mathrm{t}} \end{bmatrix}. \tag{5.21}$$

Similarly,

$$\hat{\boldsymbol{n}}_r = \boldsymbol{R}\hat{n}_{ro} = \boldsymbol{R}_\gamma \boldsymbol{R}_\alpha \boldsymbol{R}_\beta \hat{n}_{ro} = \begin{bmatrix} \cos\beta\sin\gamma\sin\alpha + \cos\gamma\sin\beta \\ \sin\gamma\sin\beta - \cos\gamma\cos\beta\sin\alpha \\ \cos\alpha\cos\beta \end{bmatrix} = \begin{bmatrix} \sin\theta_{\mathrm{r}}\cos\varphi_{\mathrm{r}} \\ \sin\theta_{\mathrm{r}}\sin\varphi_{\mathrm{r}} \\ \cos\theta_{\mathrm{r}} \end{bmatrix}. \tag{5.22}$$

Based on the illustration of Fig. 5.4, and given that $z_{\mathrm{t}} = D$, (5.17) and (5.18) can be expressed as:

$$\cos(\phi_{\mathrm{t}}) = \underbrace{\left(-\frac{x_{\mathrm{r}}}{L}\cos(\varphi_{\mathrm{t}}) - \frac{y_{\mathrm{r}}}{L}\sin(\varphi_{\mathrm{t}})\right)}_{a_{\mathrm{t}}}\sin(\theta_{\mathrm{t}}) + \underbrace{\frac{D}{L}}_{b}\cos(\theta_{\mathrm{t}}) \tag{5.23}$$

$$\cos(\phi_{\mathrm{r}}) = \underbrace{\left(-\frac{x_{\mathrm{r}}}{L}\cos(\varphi_{\mathrm{r}}) - \frac{y_{\mathrm{r}}}{L}\sin(\varphi_{\mathrm{r}})\right)}_{a_{\mathrm{r}}}\sin(\theta_{\mathrm{r}}) + \underbrace{\frac{D}{L}}_{b}\cos(\theta_{\mathrm{r}}), \tag{5.24}$$

where we have defined the parameters a_{t}, a_{r}, and b for notation simplicity, similar to the approach in [151]. We model x_{r} and y_{r} by zero-mean independent Gaussian random variables (RVs) with variance σ^2_{pr}. Also, for simplicity, θ_{r} is modeled as a zero-mean Gaussian-distributed RV with variance $\sigma^2_{\theta\mathrm{r}}$.

5.4 Channel coefficient distribution

In order to analytically evaluate the link performance, we need the probability density function (PDF) of the received signal in the general case of a link subject to Tx-Rx angular misalignments and displacements. For the sake of simplicity, we assume that the concentrator gain $g(\phi_{\mathrm{r}})$ and the optical filter transmittance $T_{\mathrm{s}}(\phi_{\mathrm{r}})$ are independent of ϕ_{r}, and denote them simply by T_s and g, respectively. Regarding the optical filter, this simplification could be equivalent to removing the optical filter, as we assume negligible background noise, see the last part of Subsection 5.2.1.[4] From (5.1) and (5.2), we have:

$$h = h_c \cos^m(\phi_\mathrm{t})\cos(\phi_\mathrm{r})\,\Pi\Big(\frac{\phi_\mathrm{r}}{\phi_\mathrm{FoVr}}\Big), \tag{5.25}$$

where h_c denotes the deterministic part of h:

$$h_c = \frac{m+1}{2\pi}\frac{A_\mathrm{PD}\,T_\mathrm{s}\,g}{L^2}\,e^{-(LK_\mathrm{d})}. \tag{5.26}$$

Let us further separate in (5.25) the parts depending only on ϕ_t and ϕ_r, that we denote by h_{ϕ_t} and h_{ϕ_r}, respectively:

$$h = h_c\,h_{\phi_\mathrm{t}}\,h_{\phi_\mathrm{r}}, \tag{5.27}$$

$$h_{\phi_\mathrm{t}} = \cos^m(\phi_\mathrm{t}), \tag{5.28}$$

$$h_{\phi_\mathrm{r}} = \cos(\phi_\mathrm{r})\,\Pi\Big(\frac{\phi_\mathrm{r}}{\phi_\mathrm{FoVr}}\Big). \tag{5.29}$$

To derive the PDF of h, we consider the following cases in the subsequent subsections. First, in Subsection 5.4.1, only Tx angular misalignments are considered (without any displacement) while assuming a fixed Rx (orientation and position) and a (fixed) large Rx FoV. Then, in Subsection 5.4.2, both Tx and Rx angular misalignments are taken into account without any displacement, i.e., as illustrated in Fig. 5.3. The PDF is then modified in in Subsection 5.4.3 to account for Rx displacements, i.e., as in Fig. 5.4. Lastly, the generalization to the case of limited Rx FoV is considered in Subsection 5.4.4.

5.4.1 Tx angular misalignment and fixed Rx

The key point here is to relate the distribution of h back to the random angular misalignment of the buoy. For this case, $\phi_\mathrm{t} = \theta_\mathrm{t}$ and $\phi_\mathrm{r} = \theta_\mathrm{r} = 0$, thus $h_{\phi_\mathrm{r}} = 1$, and $h = h_\mathrm{c}\,h_{\phi_\mathrm{t}}$ that we denote by h_0 whose cumulative density function (CDF) can be obtained as:

$$\begin{aligned} F_{h_0}(h_0) &= \Pr\big(h_c h_{\phi_\mathrm{t}} \le h_0\big) = \Pr\big(h_c\cos^m(\theta_\mathrm{t}) \le h_0\big) \\ &= \Pr\Big(\theta_\mathrm{t} > \cos^{-1}\Big(\sqrt[m]{\frac{h_0}{h_c}}\Big)\Big) = 1 - F_{\theta_\mathrm{t}}\Big(\cos^{-1}\Big(\sqrt[m]{\frac{h_0}{h_c}}\Big)\Big), \end{aligned} \tag{5.30}$$

where $F_{\theta_\mathrm{t}}(.)$ denotes the CDF of θ_t. From (5.30), the PDF of h_0 can be obtained as follows:

$$f_{h_0}(h_0) = \frac{C_1}{m h_0\sqrt{\Big(\sqrt[m]{\frac{h_0}{h_c}}\Big)^{-2} - 1}}\,f_{\theta_\mathrm{t}}\Big(\cos^{-1}\Big(\sqrt[m]{\frac{h_0}{h_c}}\Big)\Big), \tag{5.31}$$

where C_1 is a normalization coefficient to have $F_{h_0}(\infty) = 1$, and $f_{\theta_\mathrm{t}}(.)$ is the PDF of θ_t that is obtained from (5.19) as $f_{\theta_\mathrm{t}}(\theta_\mathrm{t}) = 2\pi\, f_{\theta_\mathrm{t},\varphi_\mathrm{t}}(\theta_\mathrm{t},\varphi_\mathrm{t})$.

---

[4] Note that, in general, the approximation of a constant T_s is justified when the FoV is relatively small, with the range depending on the filter bandwidth. Nevertheless, recent techniques have shown the possibility of designing relatively wide FoV optical filters using metamaterials, e.g. [152]. Investigation of link parameter optimization while taking into account the dependence of T_s on ϕ_r, which is particularly interesting when background noise effect cannot be neglected (e.g., in downlink), can be subject of future research.

5.4.2 Tx-Rx angular misalignments and fixed Rx position

We consider now random $\phi_\mathrm{t} = \theta_\mathrm{t}$ and $\phi_\mathrm{r} = \theta_\mathrm{r}$, while considering $\phi_\mathrm{FoVr} > \phi_\mathrm{r}$. In this case, $h = h_c \cos^m(\theta_\mathrm{t})\cos(\theta_\mathrm{r}) = h_0\, h_{\phi_\mathrm{r}}$. The CDF of h_{ϕ_r}, $F_{h_{\phi_\mathrm{r}}}(.)$, can be written as:

$$F_{h_{\phi_\mathrm{r}}}(h_{\phi_\mathrm{r}}) = \Pr\big(\cos(\theta_\mathrm{r}) \le h_{\phi_\mathrm{r}}\big) = 1 - F_{\theta_\mathrm{r}}\big(\cos^{-1}(h_{\phi_\mathrm{r}})\big). \tag{5.32}$$

Subsequently, the PDF of h_{ϕ_r}, $f_{h_{\phi_\mathrm{r}}}(.)$, is:

$$f_{h_{\phi_\mathrm{r}}}(h_{\phi_\mathrm{r}}) = \frac{C_2}{\sqrt{1-{h_{\phi_\mathrm{r}}}^2}}\, f_{\theta_\mathrm{r}}\big(\cos^{-1}\left(h_{\phi_\mathrm{r}}\right)\big), \tag{5.33}$$

where C_2 is a normalization coefficient. Afterwards, the PDF of h can be obtained as:

$$f_h(h) = \int f_{h|h_{\phi_\mathrm{r}}}(h|h_{\phi_\mathrm{r}})\, f_{h_{\phi_\mathrm{r}}}(h_{\phi_\mathrm{r}})\, d h_{\phi_\mathrm{r}}, \tag{5.34}$$

where

$$f_{h|h_{\phi_\mathrm{r}}}(h|h_{\phi_\mathrm{r}}) = \frac{1}{h_{\phi_\mathrm{r}}} f_{h_0}\Big(\frac{h}{h_{\phi_\mathrm{r}}}\Big) = \frac{C_3}{m\,h\sqrt{\Big(\sqrt[m]{\frac{h}{h_c h_{\phi_\mathrm{r}}}}\Big)^{-2} - 1}}\, f_{\theta_\mathrm{t}}\left(\cos^{-1}\Big(\sqrt[m]{\frac{h}{h_c h_{\phi_\mathrm{r}}}}\Big)\right), \tag{5.35}$$

and C_3 is a normalization coefficient.

5.4.3 Tx-Rx angular misalignments and Rx displacements

In this case, $\phi_\mathrm{t} \neq \theta_\mathrm{t}$ and $\phi_\mathrm{r} \neq \theta_\mathrm{r}$. We assume that the Rx displacements are negligible, compared to the link range, which is reasonable in practice. Consequently, we assume $D \approx L$, and hence, consider h_c as almost constant. Given that we have six RVs that are involved in h (i.e., x_r, y_r, φ_t, φ_r, θ_t, and θ_r), the derivation of the general form of $f_h(h)$ is quite complex. Therefore, for simplicity, and similar to the approach considered in [151], we derive the PDF of h by fixing the Rx position (x_r and y_r) and the azimuthal angles[5] φ_t and φ_r. According to (5.23), we have $\cos(\phi_\mathrm{t}) = a_\mathrm{t}\sin(\theta_\mathrm{t}) + b\cos(\theta_\mathrm{t})$, which can be written as [151]:

$$\cos\left(\phi_\mathrm{t}\right) = \mathrm{sgn}(a_\mathrm{t})\sqrt{a_\mathrm{t}^2 + b^2}\,\sin\Big(\theta_\mathrm{t} + \tan^{-1}(b/a_\mathrm{t})\Big). \tag{5.36}$$

We consider in the following the case of $a_\mathrm{t} < 0$, i.e., $\mathrm{sgn}(a_\mathrm{t}) = -1$, which allows a simpler derivation[6] of $f_h(h)$. Recall our notation of $h = h_\mathrm{c}\, h_{\phi_\mathrm{t}}\, h_{\phi_\mathrm{r}} = h_0\, h_{\phi_\mathrm{r}}$. Thus,

$$f_{h|h_{\phi_\mathrm{r}}}(h|h_{\phi_\mathrm{r}}) = \frac{1}{h_{\phi_\mathrm{r}}} f_{h_0}\Big(\frac{h}{h_{\phi_\mathrm{r}}}\Big). \tag{5.37}$$

---

[5] As suggested in [153], this would correspond to the case where the Rx only tilts to front and back while the Rx normal $\hat{n}_r$ faces the Tx.

[6] The PDF of h for the case of $a_\mathrm{t} > 0$ is much more complex but can be obtained using the proposed approach in [151].

The CDF of h_0 can be written as:

$$\begin{aligned} F_{h_0}(h_0) &= \Pr\big(h_c \cos^m(\phi_\mathrm{t}) \leq h_0\big) = \Pr\left(\theta_\mathrm{t} > -\sin^{-1}\left(\frac{\sqrt[m]{\frac{h_0}{h_c}}}{\sqrt{a_\mathrm{t}^2+b^2}}\right) - \tan^{-1}\left(\frac{b}{a_\mathrm{t}}\right)\right) \\ &= 1 - F_{\theta_\mathrm{t}}\left(-\sin^{-1}\left(\frac{\sqrt[m]{\frac{h_0}{h_c}}}{\sqrt{a_\mathrm{t}^2+b^2}}\right) - \tan^{-1}\left(\frac{b}{a_\mathrm{t}}\right)\right). \end{aligned} \tag{5.38}$$

Consequently,

$$f_{h_0}(h_0) = \frac{-C_4 \sqrt[m]{\frac{h_0}{h_c}}}{m h_0 \sqrt{a_\mathrm{t}^2+b^2-\left(\sqrt[m]{\frac{h_0}{h_c}}\right)^2}}\, f_{\theta_\mathrm{t}}\left(-\sin^{-1}\left(\frac{\sqrt[m]{\frac{h_0}{h_c}}}{\sqrt{a_\mathrm{t}^2+b^2}}\right) - \tan^{-1}\left(\frac{b}{a_\mathrm{t}}\right)\right), \tag{5.39}$$

where C_4 is a normalization coefficient. Similarly, using (5.24), we can write $\cos(\phi_\mathrm{r}) = a_\mathrm{r}\sin(\theta_\mathrm{r}) + b\cos(\theta_\mathrm{r})$. Then, the PDF of h_{ϕ_r} can be given as:

$$f_{h_{\phi_\mathrm{r}}}(h_{\phi_\mathrm{r}}) = \frac{-C_5}{\sqrt{a_\mathrm{r}^2+b^2-h_{\phi_\mathrm{r}}^2}}\, f_{\theta_\mathrm{r}}\left(-\sin^{-1}\left(\frac{h_{\phi_\mathrm{r}}}{\sqrt{a_\mathrm{r}^2+b^2}}\right) - \tan^{-1}\left(\frac{b}{a_\mathrm{r}}\right)\right), \tag{5.40}$$

where C_5 is a normalization coefficient. Therefore for this case,

$$f_{h|h_{\phi_\mathrm{r}}}(h|h_{\phi_\mathrm{r}}) = \frac{-C_6 \sqrt[m]{\frac{h}{h_c h_{\phi_\mathrm{r}}}}}{m\, h \sqrt{a_\mathrm{t}^2+b^2-\left(\sqrt[m]{\frac{h}{h_c h_{\phi_\mathrm{r}}}}\right)^2}}\, f_{\theta_\mathrm{t}}\left(-\sin^{-1}\left(\frac{\sqrt[m]{\frac{h}{h_c h_{\phi_\mathrm{r}}}}}{\sqrt{a_\mathrm{t}^2+b^2}}\right) - \tan^{-1}\left(\frac{b}{a_\mathrm{t}}\right)\right), \tag{5.41}$$

and C_6 is a normalization coefficient. Lastly, $f_h(h)$ is obtained from (5.34) by marginalization.

5.4.4 Limited Rx FoV; Tx-Rx angular misalignments and Rx displacements

Now we apply to the last stage the FoV limitation. Inspired by the approach in [154], the CDF of h_{ϕ_r} needs to be modified as follows.

$$\begin{aligned} F_{h_{\phi_\mathrm{r}}}(h_{\phi_\mathrm{r}}) &= \Pr\left(\cos(\phi_\mathrm{r})\,\Pi\left(\frac{\phi_\mathrm{r}}{\phi_\mathrm{FoVr}}\right) \leq h_{\phi_\mathrm{r}}\right) = \underbrace{\Pr\left(\cos^{-1}(h_{\phi_\mathrm{r}}) < \phi_\mathrm{r} \leq \phi_\mathrm{FoVr}\right)}_{1-F_{\phi_\mathrm{r}}(\cos^{-1}(h_{\phi_\mathrm{r}}))} + \underbrace{\Pr\left(\phi_\mathrm{r} > \phi_\mathrm{FoVr}\right)}_{1-F_{\phi_\mathrm{r}}(\phi_\mathrm{FoVr})} \\ &= 1 - F_{\theta_\mathrm{r}}\left(-\sin^{-1}\left(\frac{h_{\phi_\mathrm{r}}}{\sqrt{a_\mathrm{r}^2+b^2}}\right) - \tan^{-1}\left(\frac{b}{a_\mathrm{r}}\right)\right) + \left(1 - F_{\phi_\mathrm{r}}(\phi_\mathrm{FoVr})\right). \end{aligned} \tag{5.42}$$

In the right side of the first line of (5.42), the first term accounts for the probability that an incident ray falls within the Rx FoV, while the second terms corresponds to a link interruption. The resulting PDF is then:

$$f_{h_{\phi_\mathrm{r}}}(h_{\phi_\mathrm{r}}) = \frac{-C_7}{\sqrt{a_\mathrm{r}^2+b^2-h_{\phi_\mathrm{r}}^2}}\, f_{\theta_\mathrm{r}}\left(-\sin^{-1}\left(\frac{h_{\phi_\mathrm{r}}}{\sqrt{a_\mathrm{r}^2+b^2}}\right) - \tan^{-1}\left(\frac{b}{a_\mathrm{r}}\right)\right) + \left(1 - F_{\phi_\mathrm{r}}(\phi_\mathrm{FoVr})\right)\delta(h_{\phi_\mathrm{r}}), \tag{5.43}$$

where the Dirac delta function accounts for the discontinuity of the CDF at $h_{\phi_\mathrm{r}} = 0$ [154], and C_7 is a normalization coefficient. The PDF of h can be obtained by marginalization from (5.34) using (5.41) and (5.43).

5.5 Numerical results

This section presents numerical results to study the link performance and the impact of link parameter optimization.

5.5.1 Parameter specification

We consider a vertical link operating at depth Z in clear ocean waters having a chlorophyll concentration of $C_{\mathrm{cl}} = 0.5\,\mathrm{mg/m^3}$. At the Tx, we use a blue LED of wavelength 470 nm with a spectral half-width of 20 nm [98]. For this wavelength and the considered C_{cl}, K_{d} is approximately $0.08\,\mathrm{m}^{-1}$ [155, 156]. At the Rx, we use an optical filter of BW $\Delta\lambda = 20\,\mathrm{nm}$, where for the sake of simplicity, we assume that its signal transmission T_{s} is nearly constant and equal to 1 [100]. Also, a blue-sensitive SiPM with reference SensL B-series MicroSB 30020 [96] is considered. Note that the deadtime of the SiPM is $\tau_d = 90\,\mathrm{ns}$, during which the detector is unable to detect a new incoming photon [59, 36]. The extinction ratio for OOK Off/On symbols is set to $\xi = 0.4$ and the bit rate to $R_b = 1\,\mathrm{Mbps}$. It is worth mentioning that τ_d is much smaller than the considered symbol duration, i.e., $1\,\mu\mathrm{s}$, and furthermore, the typical modulation BWs of the LED and the SiPM are assumed to be much higher than the signal BW [62]. Hence, no inter-symbol interference affects the transmitted signal.[7] Unless otherwise specified, the link range (i.e., the AUV operational depth in our case study) is set to 100 m, and the average Tx power is set to $P_{\mathrm{Tx}} = 20\,\mathrm{W}$ that can be obtained by using multiple LEDs at the Tx [27, 62]. Table 5.1 summarizes the considered parameters used for the link performance evaluation.

We do not consider any forward error correction (FEC) and set the target BER to the FEC threshold $\mathrm{BER_{th}} = 2\times10^{-3}$ [102]. To calculate P_{out}, we use statistical and analytical approaches. By the statistical approach, in the general case of misaligned link illustrated in Fig. 5.4, for instance, we generate independent RVs θ_{t}, ϕ_{t}, φ_{t}, θ_{r}, ϕ_{r}, φ_{r}, x_{r}, and y_{r} according to the considered distributions, and use them to calculate the corresponding channel attenuation h. Then, for each channel realization h, the BER is calculated from (5.7). The outage probability P_{out} is calculated based on more than 10^7 channel realizations and for a given $\mathrm{BER_{th}}$. On the other hand, by the analytical method, we calculate the approximate P_{out} from (5.10) using the derived analytical PDFs $f_h(h)$ in Section 5.4, through numerical integration [158].

Concerning the parameters related to angular misalignment and displacement of the AUV, we consider a range of a few degrees for $(\sigma_{\theta\mathrm{t}}, \sigma_{\theta\mathrm{r}})$ and a range of a few meters for σ_{pr}, which are close to practical uplink and downlink scenarios.[8]

---

[7] For very high data rates where the deadtime limitation induces inter-symbol interference, [157] proposed an optimal signal detection approach, based on the number of counts and arrival times of the photons. Also, appropriate signaling schemes were proposed in [62, 61] for the case of limited Tx/Rx modulation BW with respect to the data rate.

[8] For instance, some ultra-short baseline (USBL) underwater acoustic positioning systems used for AUVs, such as the Subsonus USBL and its corresponding transponder, Subsonus tag, have their respective pitch and roll accuracies as $\sim 0.1^\circ$ and $\sim 1^\circ$ [159, 160]. Also, the position accuracies of Subsonus USBL and Subsonus tag are around 0.5 and 1.5 m,

Table 5.1: Simulation Parameters

Parameter	Value
Tx wavelength λ	470 nm
Tx average transmit power P_{Tx}	20 W
OOK extinction ratio ξ	0.4
Bit rate R_{b}	1 Mbps
Optical filter BW	20 nm
SiPM active area A_{PD}	9 mm^2
SiPM, number of SPADs	10998
SiPM, fill factor	48 %
SiPM gain G	10^6
SiPM photon detection efficiency Υ_{PDE}	24 %
SiPM dark count rate f_{DCR}	6.6 MHz
SiPM dark current I_{d}	1.10 μA
SiPM prob. of cross-talk P_{CT}	0.03 %
SiPM prob. of after-pulsing P_{AP}	0.2 %
SiPM deadtime τ_d	90 ns
SiPM excess noise factor F	1.1
TIA load resistance R_{L}	1 kΩ
Target BER, $\mathrm{BER}_{\mathrm{th}}$	2×10^{-3}

In what follows, we first illustrate the effect of different factors that result in pointing errors in the considered case studies. Then, we focus on Tx/Rx parameter optimization, i.e., m and θ_{FoV}, and investigate its effect on the overall link performance.

5.5.2 Effect of misalignment parameters on outage probability, Buoy-to-AUV downlink

First, to get an idea of the effect of wind speed and AUV angular misalignments and displacements, consider the downlink configuration, i.e., from the buoy to the AUV, and see the impact of different parameters. Consider a (fixed) LED Lambertian order of $m = 20$, corresponding to a beam divergence of about 15°, a (fixed) large Rx FoV $\phi_{\mathrm{FoVr}} = \pi/2$, and a link range of 65 m. For the three cases specified in Subsections 5.4.1, 5.4.2, and 5.4.3, are presented in Fig. 5.5 the outage probability versus the corresponding misalignment parameter, i.e., U, $\sigma_{\theta\mathrm{r}}$, and σ_{pr}, respectively.
Notice the good match between the simulation-based (statistical MC) and analytical results, which

---

respectively, at a typical range of 100 m [159, 160].

shows the accuracy of the approximate analytical formulas. Indeed, they provide a tight lower bound on P_{out} for the considered operating conditions. From Fig. 5.5(a), for fixed (and exact) AUV position and orientation, notice a significant impact of the wind speed U on the link performance. Comparing this with Fig. 5.5(b), notice that AUV angular misalignments have a less significant impact on P_{out}; it is almost unaffected for $\sigma_{\theta\text{r}}$ up to 10° corresponding to little angular deviations of the Rx from the beam LoS. For angular deviations larger than $\sim 15°$ (which is close to the considered Tx beam divergence), a significant P_{out} degradation is noticed as the Rx largely turns away from the beam spot.
For Fig. 5.5(c), following our approach in Subsection 5.4.3 for the derivation of the analytical PDF of h, we have set $\varphi_\text{t} = \varphi_\text{r} = 30°$, and calculated P_{out} for a fixed displacement $x_\text{r} = y_\text{r}$. Notice a significant performance degradation with displacement error. For $x_\text{r} = y_\text{r} \gtrsim 5\,\text{m}$, P_{out} is almost equal to one, meaning that the Rx is completely away from the transmitted beam LoS.

Similar to Fig. 5.5(a), we have further presented in Fig.5.6 P_{out} as a function of the average transmit power P_{Tx} and the sea surface wind speed U, assuming exactly positioned Rx. We notice that with increase in U, an increase in P_{Tx} can only marginally compensate for this P_{out} degradation. However, it will be shown in the following subsection that the optimization of the Tx/Rx parameters can improve the link performance considerably.

5.5.3 Effect of Tx/Rx parameter optimization, Buoy-to-AUV downlink

For different link conditions, we investigate the effect of optimizing Tx and Rx parameters, i.e., m and ϕ_{FoVr} for limited Rx FoV. Two scenarios are considered: without and with Rx position displacement. The presented results are obtained using MC simulations.

5.5.3.1 Scenario 1: Negligible Rx position displacement

Consider first the case where there is no position displacement for the Rx, see Fig. 5.3. Figure 5.7 shows the 3D plot of P_{out} versus m and ϕ_{FoVr} for $U = 3\,\text{m/s}$ and $\sigma_{\theta\text{r}} = 5°$. We notice that significant performance improvement can be obtained by using the optimal parameters in terms of reducing the outage probability, here, $m_{\text{opt}} \approx 5$ and $\phi_{\text{FoVr,opt}} \approx 14°$ resulting in the minimum $P_{\text{out}} = 6.64 \times 10^{-3}$.

Subsequently, for increased wind speeds of $U = 6$ and $9\,\text{m/s}$ and $\sigma_{\theta\text{r}} = 5°$, we have shown in Fig. 5.8 plots of P_{out} versus m. To simplify the presentation in a 2D plot, we have considered for each m the corresponding $\phi_{\text{FoVr,opt}}$ resulting in the minimum P_{out}. As reference to the results in Fig.5.7, we have also shown the P_{out} plot for $U = 3\,\text{m/s}$. These results clearly show the destructive impact of U on the link performance. Also, optimized Tx-Rx parameters allow a significant improvement in the link performance; the optimum parameters and the corresponding P_{out} values are indicated in the figure. We notice that for increased U, a smaller m should be used. This is quite rational, since by increased Tx angular misalignments, we should use a wider Tx beam to

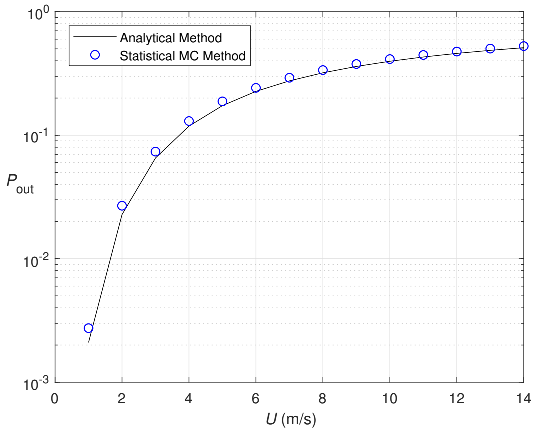

(a) Tx angular misalignments and fixed Rx

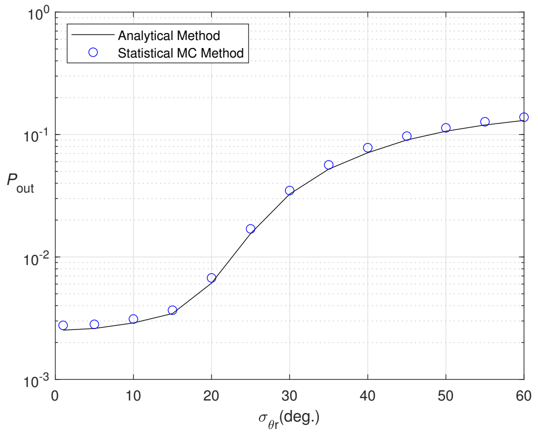

(b) Tx-Rx angular misalignments and fixed Rx

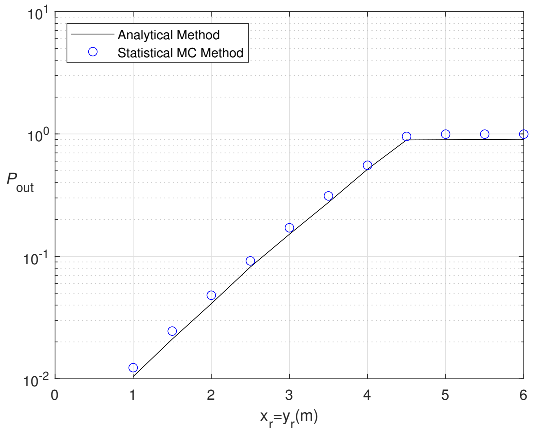

(c) Tx-Rx angular misalignments and Rx displacements

Figure 5.5: Effect of misalignment parameters on P_{out} performance using the analytical and statistical MC approaches; Downlink transmission with $m = 20$, $P_{\mathrm{Tx}} = 20\,\mathrm{W}$, $\xi = 0.4$, $\phi_{\mathrm{FoVr}} = \pi/2$, and $Z = 65\,\mathrm{m}$; (a) $\sigma_{\theta\mathrm{r}} = 0$, $\sigma_{\mathrm{pr}} = 0$; (b) $U = 1\,\mathrm{m/s}$, $\sigma_{\mathrm{pr}} = 0$; (c) $U = 1\,\mathrm{m/s}$, $\sigma_{\theta\mathrm{r}} = 5°$.

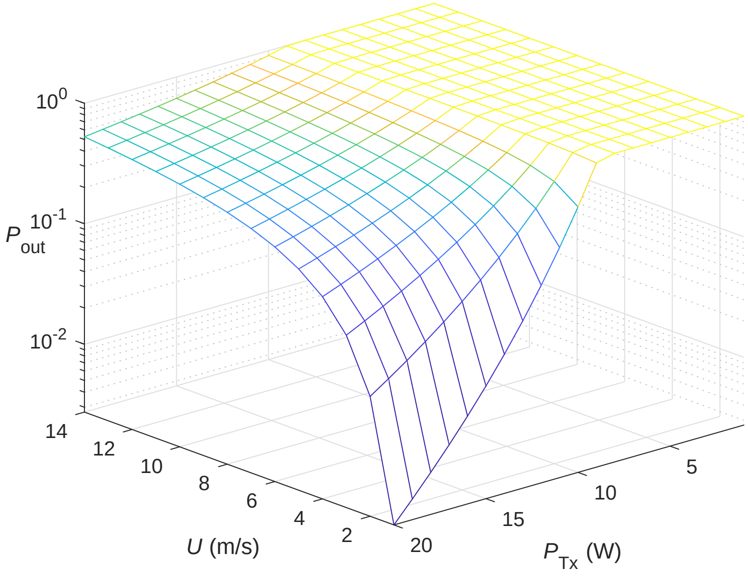

Figure 5.6: Effect of wind speed U and the average transmit power P_{Tx} on the P_{out}; $\sigma_{\theta\mathrm{r}} = 0$, $\sigma_{\mathrm{pr}} = 0$, $m = 20$, $\xi = 0.4$, $\phi_{\mathrm{FoVr}} = \pi/2$, and $Z = 65\,\mathrm{m}$.

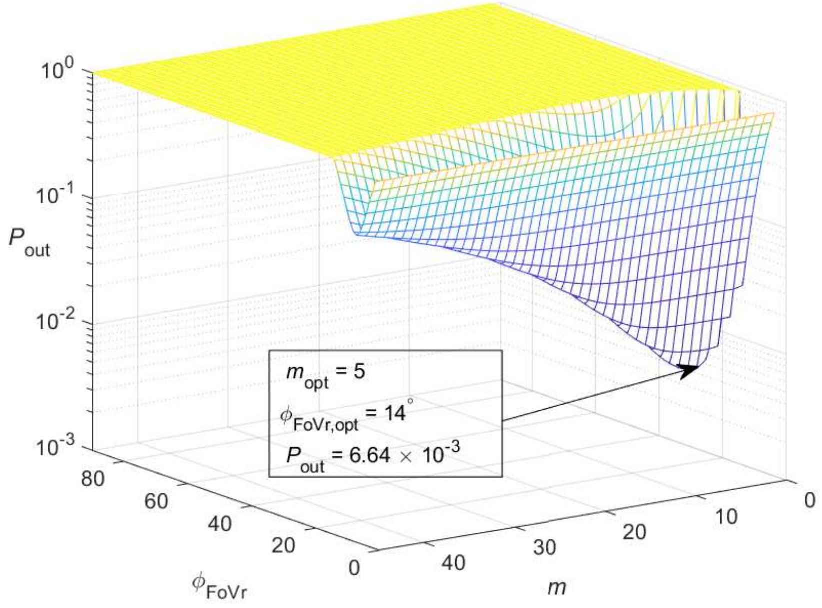

Figure 5.7: Scenario 1: Effect of m and ϕ_{FoVr} (in degrees) on P_{out} for $U = 3\,\mathrm{m/s}$ and $\sigma_{\theta\mathrm{r}} = 5°$. $Z = 100\,\mathrm{m}$, $P_{\mathrm{Tx}} = 20\,\mathrm{W}$.

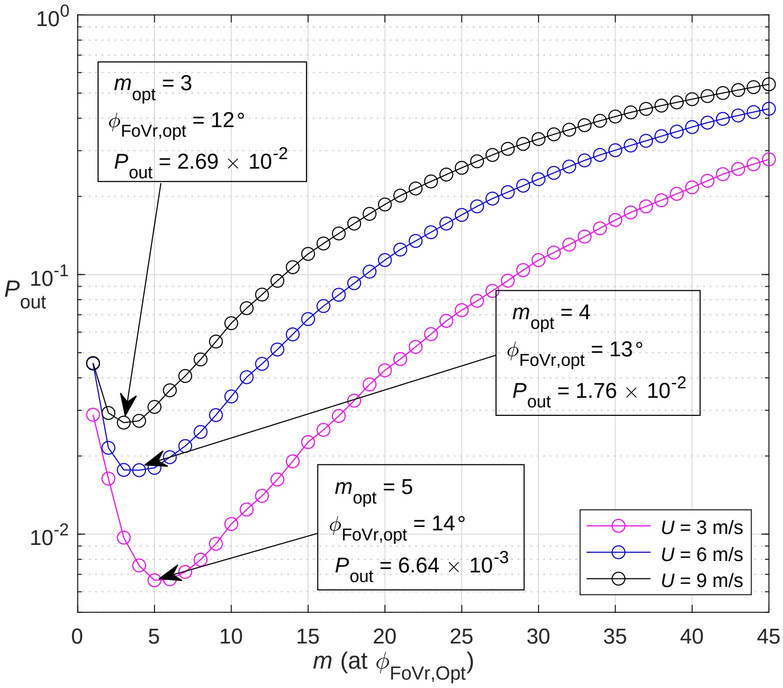

Figure 5.8: Scenario 1: Effect of m on P_{out} using optimum ϕ_{FoVr} for $U = 3$, 6, and 9 m/s and $\sigma_{\theta\text{r}} = 5°$. $Z = 100$ m, $P_{\text{Tx}} = 20$ W.

minimize the probability of receiving a too weak signal at the Rx. In other words, surface waves are more likely to direct the signal away from the Rx FoV, thus the beam should be widened to ensure the signal reaches the Rx. The optimum Rx FoV values are rather close; yet, $\phi_{\text{FoVr,opt}}$ decreases by increasing U: it equals 14°, 13°, and 12°, for $U = 3$, 6, and 9 m/s, respectively. To explain this, we note from (3.12) and (3.13) that the effective Rx area A_{eff} is inversely related to ϕ_{FoVr} due to the use of a non-imaging concentrator. Hence, a decrease in $\phi_{\text{FoVr,opt}}$ arising from an increased U is justified by achieving a larger effective light collection area, compensating for more pointing errors.

To see the effect of the Rx's $\sigma_{\theta\text{r}}$, we have fixed U at 3 m/s and increased $\sigma_{\theta\text{r}}$ to 7° and 10°. Results are summarized in Table 5.2, where we have also provided the corresponding values of P_{int}. From these results, we notice a rather low sensitivity of m_{opt} and $\phi_{\text{FoVr,opt}}$ to $\sigma_{\theta\text{r}}$. Interestingly, as $\sigma_{\theta\text{r}}$ increases, the beam needs to be more directive (m should be increased) and the Rx FoV should increase. Indeed, increasing m increases the directivity of the transmit beam towards the normal of the Rx, while the increase in the Rx FoV aims to improve signal reception for larger Rx deviations.

Let us now investigate the effect of the average transmit power on the parameter optimization. We have summarized the results in Table 5.3, where we notice that by decrease in P_{Tx}, m_{opt} is increased, i.e., the beam is made more directive to reduce the effect of geometric loss, while $\phi_{\text{FoVr,opt}}$ is decreased to increase the Rx effective area of light collection. Overall, these two factors compensate for the reduced SNR with decrease in P_{Tx}. We have further presented in Table 5.4 the results

Table 5.2: SCENARIO 1 (DOWNLINK): OPTIMUM PARAMETERS FOR DIFFERENT $\sigma_{\theta\mathrm{r}}$ OF AUV RX DISORIENTATION; $U = 3$ m/s, $Z = 100$ m, $P_{\mathrm{Tx}} = 20$ W.

$\sigma_{\theta\mathrm{r}}$ (deg.)	m_{opt}	$\phi_{\mathrm{FoVr,opt}}$ (deg.)	P_{out}	P_{int}
5	5	14	6.64×10^{-3}	5.1×10^{-3}
7	6	15	3.84×10^{-2}	3×10^{-2}
10	8	16	1.17×10^{-1}	8.9×10^{-2}

Table 5.3: SCENARIO 1 (DOWNLINK): OPTIMUM PARAMETERS FOR DIFFERENT P_{Tx}; $U = 3$ m/s, $\sigma_{\theta\mathrm{r}} = 5°$, $Z = 100$ m.

P_{Tx} (W)	m_{opt}	$\phi_{\mathrm{FoVr,opt}}$ (deg.)	P_{out}	P_{int}
30	4	16	1.5×10^{-3}	1.4×10^{-3}
20	5	14	6.64×10^{-3}	5.1×10^{-3}
10	7	11	4.67×10^{-2}	2.78×10^{-2}

for different link ranges. Logically, the trend in m_{opt} and $\phi_{\mathrm{FoVr,opt}}$ with increase in Z is the same as with decrease in P_{Tx}. We notice that, as the Tx-Rx distance increases, m_{opt} is increased while $\phi_{\mathrm{FoVr,opt}}$ is decreased.

5.5.3.2 Scenario 2: Considering Rx position displacement

Let us now include in the considered link configuration the deviations in the position of the AUV Rx with respect to the buoy Tx. We have presented in Table 5.5 the results for $U = 3$ m/s, $\sigma_{\theta\mathrm{r}} = 5°$, and different values of the Rx displacement standard deviation σ_{pr}. The case of $\sigma_{\mathrm{pr}} = 0$ corresponds to the results previously presented in Fig. 5.7. Reasonably, with an increase in σ_{pr}, the corresponding P_{out} and P_{int} increase. For more important displacements, i.e., higher σ_{pr}, we need to widen the Tx beam (by decreasing m) and increase the effective Rx area (by decreasing ϕ_{FoVr}).

Table 5.4: SCENARIO 1 (DOWNLINK): OPTIMUM PARAMETERS FOR DIFFERENT LINK SPANS Z; $U = 3$ m/s, $\sigma_{\theta\mathrm{r}} = 5°$, $P_{\mathrm{Tx}} = 20$ W.

Z (m)	m_{opt}	$\phi_{\mathrm{FoV,opt}}$ (deg.)	P_{out}	P_{int}
90	3	20	3.39×10^{-5}	3.1×10^{-5}
100	5	14	6.64×10^{-3}	5.1×10^{-3}
110	6	9	7.81×10^{-2}	7.17×10^{-2}

Table 5.5: SCENARIO 2 (DOWNLINK): OPTIMUM PARAMETERS FOR DIFFERENT σ_{pr} OF AUV RX DISPLACEMENTS; $U = 3\,\mathrm{m/s}$, $\sigma_{\theta\mathrm{r}} = 5°$, $Z = 100\,\mathrm{m}$, $P_{\mathrm{Tx}} = 20\,\mathrm{W}$.

σ_{pr} (m)	m_{opt}	$\phi_{\mathrm{FoVr,opt}}$ (deg.)	P_{out}	P_{int}
0	5	14	6.64×10^{-3}	5.1×10^{-3}
2	5	14	1.02×10^{-2}	6.5×10^{-3}
6	4	13	4.66×10^{-2}	4.03×10^{-2}
12	4	13	2.8×10^{-1}	2.33×10^{-1}

Meanwhile, notice the small change in the optimum parameters m_{opt} and $\phi_{\mathrm{FoVr,opt}}$ with increase in σ_{pr}. This can be explained by the fact that, given the Tx beam divergence and the link range, the Rx displacements are not significant compared to the beam spot radius. This latter is considered as the radius where we get the half intensity with respect to the beam center, which is around 30 m for $m = 5$, for instance.

5.5.4 Effect of Tx/Rx parameter optimization, AUV-to-Buoy uplink

For the case of uplink transmission, i.e., from the AUV to the buoy, the angular misalignments are modeled by $\sigma_{\theta\mathrm{t}}$ (for the Tx) and U (for the Rx), respectively.

5.5.4.1 Scenario 3: Negligible Tx position displacement

Figure 5.9 shows the 3D plots of P_{out} versus m and ϕ_{FoVr} for $\sigma_{\theta\mathrm{t}} = 5°$ at the Tx and $U = 3\,\mathrm{m/s}$ at the Rx side. The optimum parameters[9] are $m_{\mathrm{opt}} = 34$ and $\phi_{\mathrm{FoVr,opt}} = 31°$, resulting in the minimum achievable $P_{\mathrm{out}} = 8.55 \times 10^{-3}$.

Similar to Subsection 5.5.3, keeping U at 3 m/s, we have presented in Fig. 5.10 the 2D plots of P_{out} versus m for $\sigma_{\theta\mathrm{t}} = 5°$, 7°, and 10°. For each m, ϕ_{FoVr} is selected so as to result in the minimum P_{out}. Like for the downlink case in the previous subsection, as $\sigma_{\theta\mathrm{t}}$ is increased (from 5° to 7° and 10°), the beam needs to be widened (i.e., m_{opt} decreases from 34 to 30, and 26), and the effective area of light collection should be increased (i.e., $\phi_{\mathrm{FoVr,opt}}$ decreases from 31° to 29°, and 27°). Once again, the Tx-Rx parameter optimization trades off geometric loss (related to beam divergence) with the Rx concentrator gain (related to the Rx FoV).

To see better the impact of U, we set $\sigma_{\theta\mathrm{t}}$ to 5° and vary U from 3 to 6 and 9 m/s. The optimum parameters together with the minimum P_{out} and P_{int} are given in Table 5.6. We notice that for increased U, the respective m_{opt} and $\phi_{\mathrm{FoVr,opt}}$ increase as well, which is consistent with the results presented for Scenario 1 in the previous subsection: The increase in the Rx angular misalignments

---

[9] Note that the larger values of optimum parameters, compared to those of the previously discussed downlink, is due to the difference in the Tx distribution, and subsequently the parameters affecting their angular misalignment.

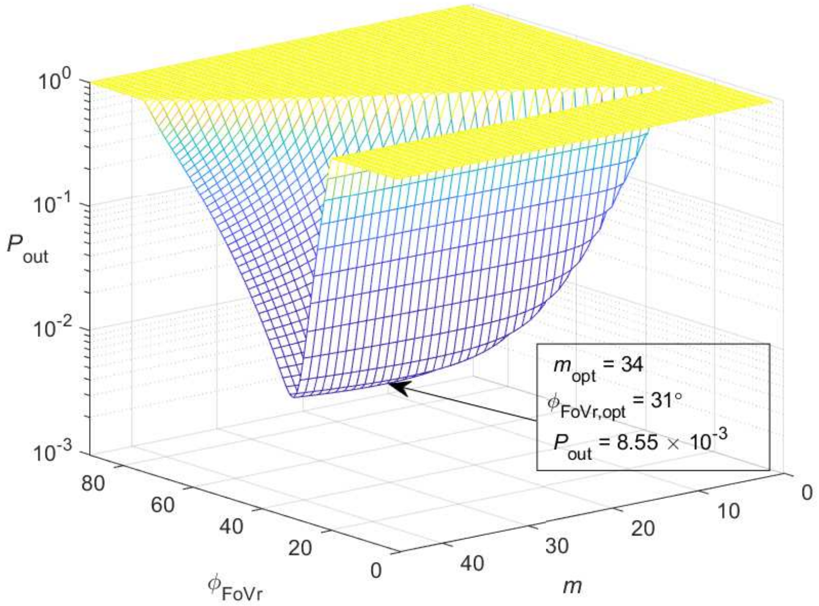

Figure 5.9: Scenario 3: Effect of m and ϕ_{FoVr} on P_{out} for the uplink. AUV's Tx with $\sigma_{\theta\mathrm{t}} = 5°$ and Buoy's Rx with $U = 3\,\mathrm{m/s}$. $Z = 100\,\mathrm{m}$, $P_{\mathrm{Tx}} = 20\,\mathrm{W}$.

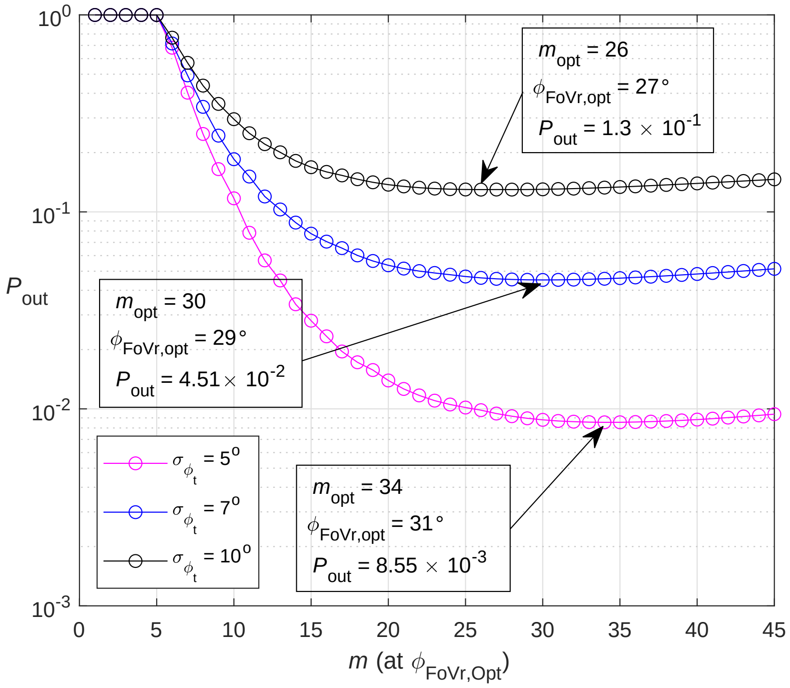

Figure 5.10: Scenario 3: Effect of m for an optimum ϕ_{FoVr} on P_{out} for AUV's Tx $\sigma_{\theta\mathrm{t}}$ of 5°, 7°, and 10° at Buoy's Rx $U = 3\,\mathrm{m/s}$. $Z = 100\,\mathrm{m}$, $P_{\mathrm{Tx}} = 20\,\mathrm{W}$.

Table 5.6: SCENARIO 3 (UPLINK): OPTIMUM PARAMETERS FOR DIFFERENT WIND SPEEDS U AFFECTING THE BUOY RX. NEGLIGIBLE TX (AUV) DISPLACEMENT; $\sigma_{\theta\mathrm{t}} = 5°$. $Z = 100\,\mathrm{m}$, $P_{\mathrm{Tx}} = 20\,\mathrm{W}$.

U (m/s)	m_{opt}	$\phi_{\mathrm{FoVr,opt}}$ (deg.)	P_{out}	P_{int}
3	34	31	8.55×10^{-3}	2×10^{-3}
6	44	35	2.05×10^{-2}	5×10^{-3}
9	45	38	3.34×10^{-2}	7.7×10^{-3}

Table 5.7: SCENARIO 4 (UPLINK): OPTIMUM PARAMETERS FOR DIFFERENT AUV TX DISPLACEMENT STANDARD DEVIATIONS σ_{pt}; $\sigma_{\theta\mathrm{t}} = 5°$, $U = 3\,\mathrm{m/s}$. $Z = 100\,\mathrm{m}$, $P_{\mathrm{Tx}} = 20\,\mathrm{W}$.

σ_{pt} (m)	m_{opt}	$\phi_{\mathrm{FoVr,opt}}$ (deg.)	P_{out}	P_{int}
0	34	31	8.55×10^{-3}	2×10^{-3}
2	37	32	1.29×10^{-2}	2.2×10^{-3}
6	40	33	5.8×10^{-2}	1.28×10^{-2}
12	43	34	3.15×10^{-1}	1.19×10^{-1}

is compensated by the increase in m (to make the beam more directive, and hence reduce the geometric loss), and an increase in ϕ_{FoVr} (to improve signal reception for larger Rx deviations although this also results in a smaller concentrator gain).

5.5.4.2 Scenario 4: Considering Tx position displacement

Including now into the link configuration the position displacements of the AUV Tx, Table 5.7 shows the optimum parameters and the performance metrics for $U = 3\,\mathrm{m/s}$, $\sigma_{\theta\mathrm{t}} = 5°$, and four values of $\sigma_{\mathrm{pt}} = 0$, 2, 6, and 12 m. Notice the relatively close optimum parameters for the considered cases. This can be justified by the fact that such small displacements impact negligibly the signal reception, given the relatively large size of the beam spot at the Rx side (which is around 17.5 m for $m = 34$, for instance; see also Subsection 5.5.3.2). In fact, with increase in σ_{pt}, m_{opt} and $\phi_{\mathrm{FoVr,opt}}$ should increase to make the beam more directional on one hand (to decrease the geometric loss), and increase the Rx FoV on the other hand (to improve signal reception). For instance, by increasing σ_{pt} from 0 to 2 m, m_{opt} and $\phi_{\mathrm{FoVr,opt}}$ are increased from 34 to 37, and from 31° to 32°, respectively.

5.6 Chapter summary

In this chapter, we have carried out a study in the design of a bi-directional UWOC link between the sea surface and a mobile underwater unit. In the link configuration, we considered the presence of misalignment between the Tx and the Rx. We have provided results for the effect of some systems parameters on the link misalignment. The presented analysis revealed that a substantial improvement in the link performance can be obtained by optimizing the main link parameters, namely the Tx Lambertian order and the Rx FoV. The corresponding optimal parameters depend on the channel and link deployment parameters including the sea-surface wind speed, AUV stability and positioning accuracy, and the received power. Note that the received power depends on the link range (here, the operating depth of the AUV) and the transmit power, for which the dependence of the optimal parameters was shown.

Chapter 6

Impact of pointing errors and oceanic turbulence on LD-based vertical UWOC link performance

Contents

6.1 Introduction

As previously emphasized, the performance of UWOC systems can be affected by oceanic turbulence-induced fading due to fluctuations in the water refractive index as a result of variations in the pressure and water temperature and salinity. Also, the reliability of UWOC links is reduced in practice by the misalignment of the Tx and the Rx due to the roughness of the sea surface, underwater currents, the mechanical and control accuracy of their host platforms, etc. Hence in this chapter, in addition to PEs we also investigate the effect of oceanic turbulence on the performance of an UWOC system.

We focus on the impact of turbulence on an optical beam propagating vertically through an aquatic media. Just as in our previous considered scenario, we assume the communication takes place vertically, between a surface unit, which can be a buoy, an autonomous surface vehicle (ASV), or a boat, and an AUV or an underwater sensor node beneath it. Typically, the surface unit can serve as a relay node for long-range data transmission from/to a ground station or a satellite [161]. Consider the typical scenario illustrated in Fig. 6.1, where the deviations in the orientation and the position of the buoy with respect to the AUV will affect the link reliability.

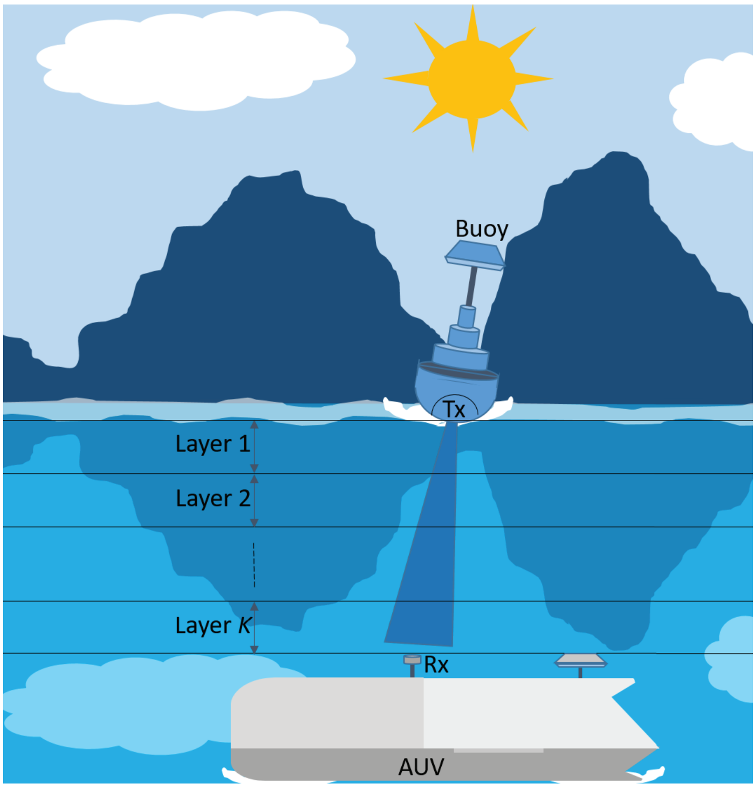

Figure 6.1: Buoy-AUV illustration of the considered vertical UWOC link.

In contrast to the previous Chapter 5, we take into account the effects of turbulence and solar background noise, as well as using a LD at the Tx (instead of LEDs as before). Note that the interest of using LDs is their relatively high modulation bandwidth and high beam directivity [41]. Also, an

SiPM-based Rx is still maintained herein, as we exploit its very high internal gain in improving the system performance, especially in extending the link range. We present an accurate statistical model for the channel turbulence to account for the aperture averaging effect, which, to the best of the authors' knowledge, has not been considered in the literature so far for the case of vertical links.

The subsequent discussions in this Chapter are as follows. Section 6.2 introduces the main assumptions of the considered system and the formulation of the link performance metrics. Next, Section 6.3 focuses on channel modelling, taking into account attenuation, turbulence, and PEs. Afterwards, numerical results are presented in Section 6.4 to investigate the interest of optimized parameter selection to improve the link performance. Lastly, Section 6.5 concludes the chapter.

Notations: Probability is denoted by $\Pr(\cdot)$; $\delta(\cdot)$ stands for the Dirac delta function; $\mathrm{E}\{\cdot\}$ denotes the expected value, and $\operatorname{erfc}(x) = \frac{2}{\sqrt{\pi}} \int_x^\infty e^{-t^2} dt$ is the well-known complementary error function.

6.2 Signal transmission modeling

Fig. 6.2 shows the general block diagram of the UWOC system based on IM/DD. The transmission range is denoted by L and the Rx lens diameter by D_r. An optical filter is typically used after the lens in order to reduce the background noise.

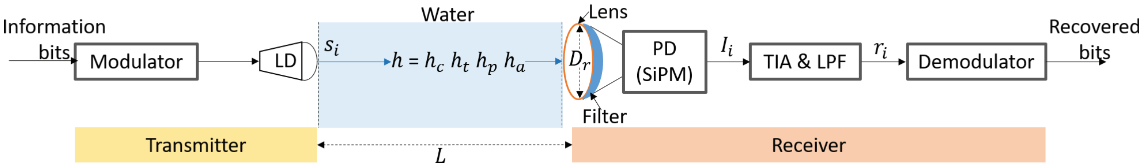

Figure 6.2: The block diagram of the UWOC communication link.

We denote the channel coefficient by h, which includes the effects of propagation loss, turbulence, and Tx-Rx random misalignment. No channel coding is considered, and signal modulation is based on NRZ OOK.

For the transmitted OOK signal s_i, $i \in \{0,1\}$, two intensity values of P_{Tx_0} and P_{Tx_1} are used, corresponding to OFF and ON states, respectively, with the average transmit optical power of P_{Tx} and the extinction ratio $\xi = P_{\mathrm{Tx}_0}/P_{\mathrm{Tx}_1}$. The average received power P_{Rx} at the Rx lens is related to P_{Tx} by $P_{\mathrm{Rx}} = h\, P_{\mathrm{Tx}}$. The generated photo-current I_i at the SiPM output is then:

$$I_i = \underbrace{\mathcal{R}_{\mathrm{e}}\, s_i\, h}_{I_{s,i}} + I_d + I_b + n_{s_i} = \check{I}_i + n_{s_i}, \tag{6.1}$$

where $I_{s,i}$, I_d, and I_b represent the useful signal, the dark current (3.6), and the background radiations; and n_{s_i} is the Rx noise, including shot noise and the random components of dark and background noises.

Considering the background noise optical power P_b due to solar radiations captured at the Rx, the subsequently generated current is expressed as [19]:

$$I_b = \mathcal{R}_\mathrm{e}\, \underbrace{E_\mathrm{sun}(\lambda, L)\, \pi\theta^2_\mathrm{FoVr}\, T_w\, T_f\, B_o\, \left(\pi D_r^2/4\right)}_{P_b}, \tag{6.2}$$

where $E_\mathrm{sun}(\lambda, L) = E_\mathrm{sun}(\lambda, 0)\, e^{-(L K_\mathrm{d})}$ is the down-welling spectral irradiance of the background at wavelength λ, with $E_\mathrm{sun}(\lambda, 0)$ as at the sea surface. Also, K_d denotes the diffuse attenuation coefficient which is dependent on the depth, the wavelength, and the concentration of particles in water [155]. The exponential term an approximation of the beam attenuation due to absorption and scattering. Furthermore, T_w is the water transmittance, B_o is the bandwidth of the Rx optical filter with transmittance T_f, and θ_FoVr is the Rx FoV in radians.

Denote the voltage signal at the LPF output by r_i:

$$r_i = R_\mathrm{L}\, I_i + n_\mathrm{th} = \underbrace{R_\mathrm{L}\, \check{I}_i}_{\check{r}_i} + R_\mathrm{L}\, n_{s_i} + n_\mathrm{th}, \tag{6.3}$$

with R_L being the load resistance of the TIA, and n_th the thermal noise with variance σ^2_th. The total Rx noise, which is signal-dependent, is modeled as a zero mean Gaussian noise with variance $\sigma^2_{n_i}$:

$$\begin{aligned} \sigma^2_{n_i} &= R^2_\mathrm{L}\, \sigma^2_{n_{s_i}} + \sigma^2_\mathrm{th} \\ &= R^2_\mathrm{L}\, (\sigma^2_{\mathrm{sh},i} + \sigma^2_\mathrm{d} + \sigma^2_\mathrm{b}) + \sigma^2_\mathrm{th}, \end{aligned} \tag{6.4}$$

where $\sigma^2_{\mathrm{sh},i}$, σ^2_d, and σ^2_b, denote the variances of the signal shot noise, dark noise, and background noise, respectively:

$$\begin{cases} \sigma^2_{\mathrm{sh},i} &= 2\,e\,G\,F\,B_e\,I_{s,i}, \\ \sigma^2_\mathrm{d} &= 2\,e\,G\,F\,B_e\,I_\mathrm{d}, \\ \sigma^2_\mathrm{b} &= 2\,e\,G\,F\,B_e\,I_\mathrm{b}, \\ \sigma^2_\mathrm{th} &= 4\,K_\mathrm{Z}\,T_e\,B_e\,R_\mathrm{L}. \end{cases} \tag{6.5}$$

Here, K_Z, T_e, F, and B_e denote the Boltzmann constant, the Rx equivalent temperature in kelvin, the PD excess noise factor, and the bandwidth of the Rx LPF, respectively. Let $B_e \approx R_\mathrm{b}/2$, with R_b being the bit rate [162].

We assume that the Rx has an exact knowledge of h, based on which it calculates the optimal OOK demodulation threshold γ_th. Taking into account the signal-dependent Rx noise, the instantaneous BER $P_e(e|h)$ (5.7) with optimal threshold (5.8), then, the average BER is given by:

$$P_e = \int_0^\infty f_h(h)\, P_e(e|h)\, dh, \tag{6.6}$$

where $f_h(h)$ is the probability density function (PDF) of h. Also, given the relatively slow channel time variations (due to either PEs or turbulence), the outage probability P_{out} is another appropriate metric for evaluating the link performance, which is defined as the probability of the instantaneous BER exceeding a threshold BER_{th}, or equivalently, the probability of h being smaller than a threshold h_{th} (5.16):

$$P_{\text{out}} = \Pr(h < h_{\text{th}}) = \int_{0}^{h_{\text{th}}} f_h(h)\,dh. \tag{6.7}$$

Obviously, both average BER and P_{out} depend on R_b.

6.3 Channel model

For the considered vertical UWOC system, the channel coefficient h is considered as:

$$h = h_c\, h_t\, h_p\, h_a, \tag{6.8}$$

where h_c denotes the propagation loss, which is the deterministic part of h, while the random components h_s, h_p and h_a represent the effect of turbulence, pointing error, and link interruption, respectively.

6.3.1 Propagation loss

h_c represents the attenuation in signal intensity as a result of absorption and scattering. Here, to simplify the derivation of analytical models for the link performance metrics, we approximate h_c by the exponential attenuation model of BL, which neglects the multiple scattering effect [68, 66]:

$$h_c = \exp(-L K_{\text{d}}). \tag{6.9}$$

6.3.2 Oceanic turbulence

Oceanic turbulence is as a result of random variations of the refractive index along the aquatic medium, which causes fluctuations in both intensity and phase of the average received signal of an UWOC system [1]. For vertical UXOC links, these fluctuations are mostly due to variations in the water temperature and salinity with depth. Based on the profiles of temperature and salinity in the Argo database [163] for different oceans and seas, different geographical locations (i.e., longitude and latitude), different seasons (i.e., summer, winter, autumn and spring) and over a long period of time, the majority of temperature and salinity gradients are in a range where the log-normal PDF shows a good match with the measurement results [70, 164]. So, modeling h_t by the log-normal distribution,

$$h_t = \exp(T), \tag{6.10}$$

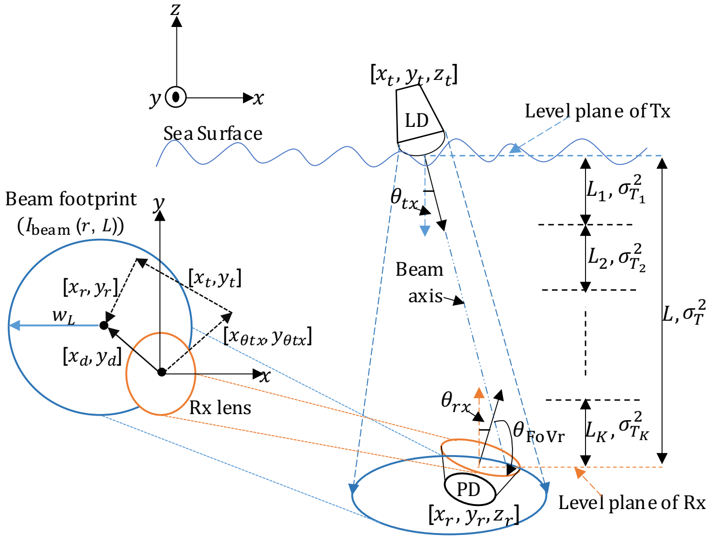

Figure 6.3: Geometry of the buoy-AUV downlink UWOC system (inspired from [20, 148]).

where T denotes the log-irradiance of turbulence, following the Gaussian distribution $\mathcal{N}(\mu_T, \sigma^2_T)$. Then, the PDF of h_t is:

$$f_{h_t}(h_t) = \frac{1}{h_t\sqrt{2\pi\sigma^2_T}} \exp\left(-\frac{\left(\ln(h_t) - \mu_T\right)^2}{2\sigma^2_T}\right). \tag{6.11}$$

Following the approach in [20], and as illustrated in Fig. 6.3, the channel is considered as a cascade of layers with different mean and variance turbulence parameters, where they are assumed as unchanged within each layer. Assume a total of K layers, with the k^{th} layer of thickness L_{T_k}, mean μ_{T_k}, and variance $\sigma^2_{T_k}$. The PDF of the corresponding channel coefficient h_{tk} is,

$$f_{h_{tk}}(h_{tk}) = \frac{1}{h_{tk}\sqrt{2\pi(4\sigma^2_{T_k})}} \exp\left(-\frac{\left(\ln(h_{tk}) - 2\mu_{T_k}\right)^2}{2(4\sigma^2_{T_k})}\right). \tag{6.12}$$

The relationship between $\sigma^2_{T_k}$ and the scintillation index of k^{th} layer $\sigma^2_{I_k}$ is given by [165]:

$$\sigma^2_{T_k} = 0.25\ln(1 + \sigma^2_{I_k}). \tag{6.13}$$

Assuming independent, non-identically distributed h_{tk} [20], μ_T and σ^2_T in (6.11) are:

$$\begin{cases} \mu_T & = & \sum_{k=1}^{K} 2\mu_{T_k}, \\ \sigma^2_T & = & \sum_{k=1}^{K} 4\sigma^2_{T_k}. \end{cases} \tag{6.14}$$

To normalize the fading coefficient, i.e., $\mathrm{E}\{h_{tk}\} = 1$, we set $\mu_{T_k} = -\sigma^2_{T_k}$.

A well-known method to reduce the scintillation effect on the received signal is aperture averaging, by using a Rx aperture diameter D_r, larger than the correlation width of the irradiance fluctuations ρ_c [166]. The correlation width for a Gaussian beam is related as $\rho_c \sim \sqrt{L/\mathcal{K}}$ with

Fresnel ratio $\wedge_0 \sim 1$, where $\mathcal{K} = 2\pi/\lambda$ is the wave number. The effect of aperture averaging has been studied in a few previous works for horizontal UWOC links [136, 137, 71]. To investigate the efficiency of aperture averaging in reducing the oceanic turbulence effect in the considered application scenario, we assume that the Rx uses a Gaussian lens, which is a combination of a thin lens with a Gaussian limiting aperture (i.e., soft aperture) [167].

Assuming a large enough photo-detector active area [166], and considering a lens of diameter D_r at the Rx, the parameters μ_T and σ_T^2 of (6.11) are obtained from (6.13) and (6.14), where the scintillation index corresponding to the k^{th}-layer, $\sigma_{I_k}^2(D_r)$, is given by (A.1) in Appendix A.1.

6.3.3 PEs

Considering the buoy-to-AUV UWOC link, the alignment between Tx and Rx is dynamically changing due to the sea surface waves, underwater currents, and instability of both the Tx and the Rx platforms. Hence at the Rx, the center of the transmitted beam spot with maximum signal intensity would deviate from the center of the Rx lens aperture.

In Fig. 6.3, considering a Gaussian beam at the Tx, the normalized spatial distribution of the irradiance at distance L of the Rx is given as [168]:

$$I_{\text{beam}}(r, L) = \frac{2}{\pi w_L^2} \exp\left(-\frac{2||r||^2}{w_L^2}\right), \tag{6.15}$$

where $r = [x, y]$ is the radial vector from the beam center and w_L is the beam waist at distance L. We denote the Cartesian coordinates of the Tx and the Rx by $[x_t, y_t, z_t]$ and $[x_r, y_r, z_r]$, respectively.

We assume under perfect Tx-Rx alignment conditions that the normal of the Tx and the Rx are co-linear to the z axis of their level plane. The Tx and the Rx angular misalignments $(\theta_{tx}, \theta_{ty}, \theta_{rx}, \theta_{ry})$ and displacements (x_t, y_t, x_r, y_r), are for simplicity modeled as zero mean Gaussian distribution with their respective variance as $(\sigma_{\theta t}^2, \sigma_{\theta r}^2)$ and $(\sigma_{pt}^2, \sigma_{pr}^2)$. It should be noted that these are the residual deviations in the orientation and the position of a stable[1] UWOC system.

Considering the orientation of the Tx, the positions of the Tx, and the Rx, the deviation of the transmitted beam spot from the center of the Rx aperture can be expressed as [148]:

$$r_d = \sqrt{x_d^2 + y_d^2}, \tag{6.16}$$

where,

$$x_d = x_t + x_r + Z\tan(\theta_{tx}) = x_{tr} + Zx_{\theta\, tx}, \tag{6.17}$$

$$y_d = y_t + y_r + Z\tan(\theta_{ty}) = y_{tr} + Zy_{\theta\, ty}. \tag{6.18}$$

---

[1] In AUVs with acoustic navigational systems such as Subsonus ultra-short baseline (USBL) and its transponder, Subsonus tag, have orientation accuracy as ~ 0.1° and ~ 1°, respectively [159, 160]. In addition, at a range of 100 m their position accuracy are about 0.5 and 1.5 m, respectively, [159, 160].

The effect on the received power by the link misalignment is the pointing error loss, which can be given by [114]:

$$h_p \approx A_0 \exp\left(-\frac{2r_d^2}{w_{Leq}^2}\right), \tag{6.19}$$

where r_d accounts for the effect of pointing error and the geometric loss [148], while the parameter for the maximum fraction of received power at $r_d = 0$ is $A_0 = (\mathrm{erf}(v))^2$ with $v = (D_r\sqrt{\pi})/(2\sqrt{2}w_L)$ and

$$w_{Leq} = \sqrt{w_L^2 \frac{\sqrt{\pi}\,\mathrm{erf}(v)}{2v\exp(-v^2)}} \tag{6.20}$$

is the equivalent beam width at the Rx. The cumulative distribution function (CDF) of h_p is,

$$\begin{aligned} F_{h_p}(h_p) &= \Pr\left(A_0 \exp\left(-\frac{2r_d^2}{w_{Leq}^2}\right) \le h_p\right) \\ &= \Pr\left(r_d > \sqrt{-\frac{w_{Leq}^2}{2}\ln\left(\frac{h_p}{A_0}\right)}\right) \\ &= 1 - F_{r_d}\left(\sqrt{-\frac{w_{Leq}^2}{2}\ln\left(\frac{h_p}{A_0}\right)}\right). \end{aligned} \tag{6.21}$$

Differentiating (6.21) with respect to h_p gives the PDF as:

$$f_{h_p}(h_p) = \frac{w_{Leq}^2}{4h_p\sqrt{-\frac{w_{Leq}^2}{2}\ln\left(\frac{h_p}{A_0}\right)}}\, f_{r_d}\left(\sqrt{-\frac{w_{Leq}^2}{2}\ln\left(\frac{h_p}{A_0}\right)}\right), \tag{6.22}$$

where $f_{r_d}(\cdot)$ is the PDF of r_d which due to prior assumptions follows a Rayleigh distribution, i.e.,

$$f_{r_d}(r_d) = (r_d/\sigma_{r_d}^2)\exp(-r_d^2/2\sigma_{r_d}^2), \tag{6.23}$$

with $\sigma_{r_d}^2$ denoting the jitter variance.

6.3.4 Link interruption

In order to take into account the link interruption h_a due to the angle-of-arrival (AoA) θ_a of the receiving beam being outside the Rx FoV, we further consider $h_a = \Pi\big(\theta_\mathrm{a}/\theta_\mathrm{FoVr}\big)$, where $\Pi(x) = 1$ if $|x| \le 1$, and zero, otherwise, then [169]:

$$\theta_\mathrm{a} = \tan^{-1}\left(\sqrt{(\tan(\theta_{tx}+\theta_{rx}))^2 + (\tan(\theta_{ty}+\theta_{ry}))^2}\right), \tag{6.24}$$

and

$$f_{\theta_\mathrm{a}}(\theta_\mathrm{a}) = \frac{\theta_\mathrm{a}}{\sigma_{\theta t}^2 + \sigma_{\theta r}^2}\exp\left(-\frac{\theta_\mathrm{a}^2}{2\left(\sigma_{\theta t}^2+\sigma_{\theta r}^2\right)}\right). \tag{6.25}$$

Also, the PDF of h_a is expressed as [148]:

$$f_{h_a}(h_a) = \left(\int_0^{\theta_{\text{FoVr}}} f_{\theta_\text{a}}(\theta_\text{a})\, d\theta_\text{a}\right)\delta(h_a - 1) + \left(1 - \int_0^{\theta_{\text{FoVr}}} f_{\theta_\text{a}}(\theta_\text{a}) d\theta_\text{a}\right)\delta(h_a), \tag{6.26}$$

where $\int_0^{\theta_{\text{FoVr}}} f_{\theta_\text{a}}(\theta_\text{a})\, d\theta_\text{a} = 1 - \exp\left(-\frac{\theta^2_{\text{FoVr}}}{2(\sigma^2_{\theta t} + \sigma^2_{\theta r})}\right)$, is the probability the AoA falls within the Rx FoV and can be denoted as $F_{\theta_\text{a}}(\theta_{\text{FoVr}})$.

6.3.5 Unlimited Rx FoV

Consider first the simple case of large Rx FoV where we assume $\theta_{\text{FoVr}} > \theta_\text{a}$. Then, $h = h_c\, h_t\, h_p$ with the PDF $f_h(h)$ as:

$$f_h(h) = \int_0^{\infty} f_{h_t}(h_t)\, f_{h|h_t}(h|h_t)\, dh_t, \tag{6.27}$$

where,

$$f_{h|h_t}(h|h_t) = \frac{1}{h_c\, h_t}\, f_{h_p}\left(\frac{h}{h_c\, h_t}\right). \tag{6.28}$$

For performance evaluation, P_{out} can be computed using (6.27) in (5.10), and after some manipulations explained in Appendix C.1, the following asymptotic closed-form expression is obtained, which is valid for small P_{out} (i.e., for $h_{\text{th}} \to 0$).

$$\begin{aligned}\lim_{h_{\text{th}}\to 0} P_{\text{out}} = (A_0\, h_c)^{-\frac{w^2_{Leq}}{4\sigma^2_{r_d}}} \exp\left(-\mu_T \frac{w^2_{Leq}}{4\sigma^2_{r_d}}\right)\\ \exp\left(\sigma^2_T \frac{w^4_{Leq}}{32\,\sigma^4_{r_d}}\right) h_{\text{th}}^{\frac{w^2_{Leq}}{4\sigma^2_{r_d}}}.\end{aligned} \tag{6.29}$$

6.3.6 Limited Rx FoV

For the case of a small Rx FoV compared to the angle of arrival, i.e. $\theta_{\text{FoVr}} < \theta_\text{a}$, hence $h = h_c\, h_t\, h_p\, h_a = h'\, h_a$, then the distribution of h, $f_h(h)$ is:

$$f_h(h) = \int_0^{\infty} f_{h'}(h')\, f_{h|h'}(h|h')\, dh', \tag{6.30}$$

where,

$$f_{h|h'}(h|h') = \frac{1}{h'}\, f_{h_a}\left(\frac{h}{h'}\right). \tag{6.31}$$

Replacing (6.31) in (6.30), the PDF of h, $f_h(h)$ can be simplified as:

$$
\begin{aligned}
f_h(h) &= \int_0^{\infty} f_{h'}(h')\,\frac{1}{h'}\left[F_{\theta_\mathrm{a}}(\theta_\mathrm{FoVr})\,\delta\left(\frac{h-h'}{h'}\right)+\left(1-F_{\theta_\mathrm{a}}(\theta_\mathrm{FoVr})\right)\delta\left(\frac{h}{h'}\right)\right]dh',\\
&= \int_0^{\infty} f_{h'}(h')\left[F_{\theta_\mathrm{a}}(\theta_\mathrm{FoVr})\,\delta\left(h-h'\right)+\left(1-F_{\theta_\mathrm{a}}(\theta_\mathrm{FoVr})\right)\delta\left(h\right)\right]dh',\\
&= \underbrace{f_{h'}(h)\,F_{\theta_\mathrm{a}}(\theta_\mathrm{FoVr})}_{f_h(h>0)}+\underbrace{\left(1-F_{\theta_\mathrm{a}}(\theta_\mathrm{FoVr})\right)\delta\left(h\right)}_{f_h(h=0)},
\end{aligned}
\tag{6.32}
$$

where $f_h(h>0)$ and $f_h(h=0)$ denote the absence and presence of link interruption in $f_h(h)$ respectively. Using (6.32), the asymptotic closed-form expression of P_out for a limited Rx FoV can be deduced from (6.29) as:

$$
\begin{aligned}
P_\mathrm{out} = \left(A_0\,h_c\right)^{-\frac{w_{Leq}^2}{4\sigma_{r_d}^2}}\exp\left(-\mu_T\frac{w_{Leq}^2}{4\sigma_{r_d}^2}\right)\\
\exp\left(\sigma_T^2\frac{w_{Leq}^4}{32\sigma_{r_d}^4}\right)h_\mathrm{th}^{\frac{w_{Leq}^2}{4\sigma_{r_d}^2}}\,F_{\theta_\mathrm{a}}(\theta_\mathrm{FoVr})+\left(1-F_{\theta_\mathrm{a}}(\theta_\mathrm{FoVr})\right).
\end{aligned}
\tag{6.33}
$$

In [39], we have investigated through a simulation-based approach the impact of system parameter optimization in improving the link performance. However, using (6.33), the values of the Tx-Rx parameter $(w_L, \theta_\mathrm{FoVr})$ for achieving a minimum P_out can be analytically computed. This is done by solving (6.33) for the minimum value of the function P_out, with two variables, w_L and θ_FoVr (i.e. $P_\mathrm{out}(w_L, \theta_\mathrm{FoVr})$). A solution can be realized through a derivative or a non-derivative method, of which the latter is used in this work (using the function 'fmincon' from MATLAB).

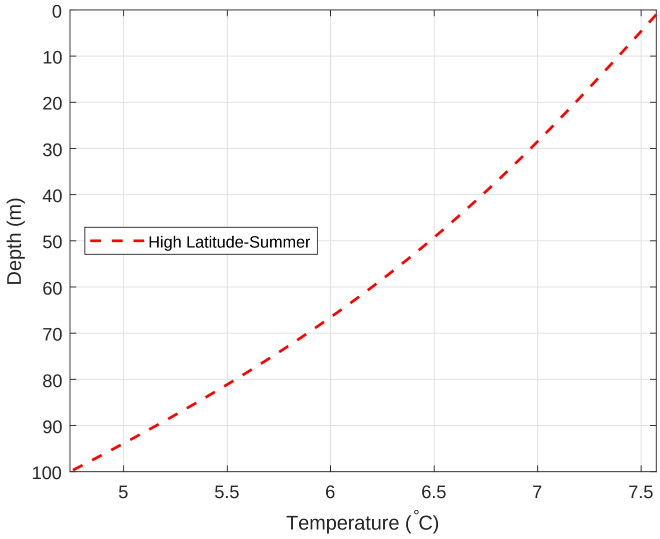

(a)

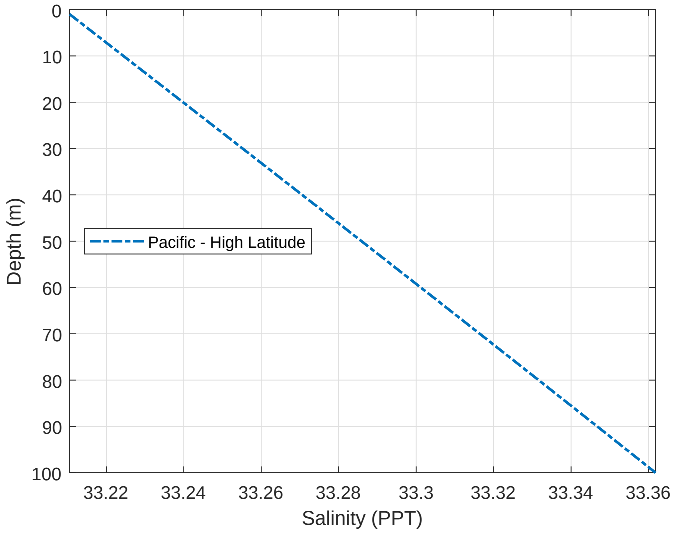

(b)

Figure 6.4: Oceanic Profile [20, 170]: (a) Temperature (b) Salinity

6.4 Numerical results and performance analysis

This section presents numerical results to analyze the performance of the considered UWOC link under the effects of turbulence and PEs.

6.4.1 Specification of underwater scenario and link parameters

The UWOC system is considered to operate in the Pacific Ocean of high latitudes, where it is well-stratified [171]. The corresponding temperature and salinity profiles are given in Fig. 6.4 [20, 170] and used to calculate the turbulence power spectrum and the scintillation index (given by (A.2) and (A.1), respectively).

The range of the vertical UWOC link is assumed to be $L = 100\,\mathrm{m}$, where clear ocean waters with a chlorophyll concentration of $C_{\mathrm{cl}} = 0.5\,\mathrm{mg/m^3}$ is considered [155]. Under these conditions, the blue-green wavelengths show the minimum beam attenuation [66]. For turbulence modeling, assuming a negligible change in the log-amplitude variance within a layer thickness of 20 m [20], we consider a 5-layer segmented vertical UWOC link, see Subsection 6.3.2.

At the Tx, a LD of wavelength $\lambda = 450\,\mathrm{nm}$ with output power of 4 W and spectral width of $\Delta\lambda = 2\,\mathrm{nm}$ is considered with a source size of $\alpha_s = 20\,\mathrm{mm}$. For this wavelength and the considered C_{cl}, we have $K_{\mathrm{d}} \approx 0.08\,\mathrm{m}^{-1}$ [155], $E_{\mathrm{sun}}(\lambda, 0) = 0.2\,\mathrm{Wm^{-2}nm^{-1}}$ [19]. Also, generalizing the results from [172], the water transmittance is considered as $T_w \approx 0.97$ for simplicity for the considered λ and C_{cl}. At the Rx, an optical filter with bandwidth $B_o = 2\,\mathrm{nm}$ is used (the same as the LD spectral width), with transmittance $T_f \approx 1$. Also, a blue-sensitive SiPM PD is used (Reference SensL B-series MicroSB 30020 [96]).

Concerning signal modulation, OOK signaling with extinction ratio of $\xi = 0.4$ and bit rate of $R_b = 20\,\mathrm{Mbps}$ is considered. Also, the target BER is considered as the forward error correction threshold, i.e., $\mathrm{BER_{th}} = 2 \times 10^{-3}$ [102].

Tables 6.1(a)-6.1(c) summarize the considered parameters used for the link performance evaluation.

6.4.2 Effect of solar noise and turbulence

Considering $E_{\mathrm{sun}}(\lambda, 0)$ of 0.2 and 0.8 $\mathrm{Wm^{-2}nm^{-1}}$, Fig. 6.5 presents the results from Monte Carlo simulations (Stat.) based on 10^8 channel realizations with the associated derived closed-form expression in (6.29) of the P_{out} with respect to the Rx FoV θ_{FoVr}. An aperture diameter D_r of 75 mm with a corresponding log-amplitude standard deviation $\sigma_T(D_r)$ of 0.0013 for 100 m link range was considered. It is observed as θ_{FoVr} increases the link P_{out} increases. This is because the amount of solar radiations captured at the Rx increases for larger θ_{FoVr}. Notice the link performance degradation is more for higher $E_{\mathrm{sun}}(\lambda, 0)$ and thus, a complete link outage ($P_{\mathrm{out}} = 1$) occurs at a smaller Rx FoV for 0.8 $\mathrm{Wm^{-2}nm^{-1}}$ with $\theta_{\mathrm{FoVr}} = \sim 100°$ compared to 0.2 $\mathrm{Wm^{-2}nm^{-1}}$ where $\theta_{\mathrm{FoVr}} = \sim 196°$.

Table 6.1: System and Channel Parameters

(a) Tx Parameters

Parameter	Value
LD wavelength λ	450 nm
LD spectral width $\Delta\lambda$	2 nm
LD transmit power for bit 1 $P_{\mathrm{Tx},1}$	4 W
OOK extinction ratio ξ	0.4
Bit rate R_b	20 Mbps

(b) Channel Parameters

Parameter	Value
Dissipation rate of mean-squared temperature $\mathcal{X}_T$	$10^{-5}\,\mathrm{K}^2\mathrm{s}^{-1}$
Dissipation rate of turbulent kinetic energy, per unit mass of fluid ϵ	$10^{-1}\,\mathrm{m}^2\mathrm{s}^{-3}$
Thermal expansion coefficient α_k	Computed by TEOS[1]
Saline contraction coefficient β_k	Computed by TEOS
Kinematic viscosity [28] υ_k	Computed by FVCOM[2]
Molecular thermal diffusivity D_{T_k}	Computed by FVCOM
Molecular salinity diffusivity D_{S_k}	$D_{S_k} \approx 0.01 D_{T_k}$

[1] TEOS: MATLAB Oceanographic Toolbox of International Thermodynamic Equation of Seawater-2010.

[2] FVCOM: MATLAB Finite Volume Community Ocean Model-toolbox.

(c) Rx Parameters

Parameter	Value
Optical filter bandwidth B_o	2 nm
LPF bandwidth B_e	$\approx R_\mathrm{b}/2$
Lens aperture diameter D_r	75 mm
SiPM active area A_PD	9 mm^2
SiPM, number of SPADs	10998
SiPM gain G	10^6
SiPM dark count rate f_DCR	6.6 MHz
SiPM dead-time τ_d	100 ns
SiPM prob. of cross-talk P_CT	0.03 %
SiPM prob. of after-pulsing P_AP	0.2 %
TIA load resistance R_L	1 kΩ

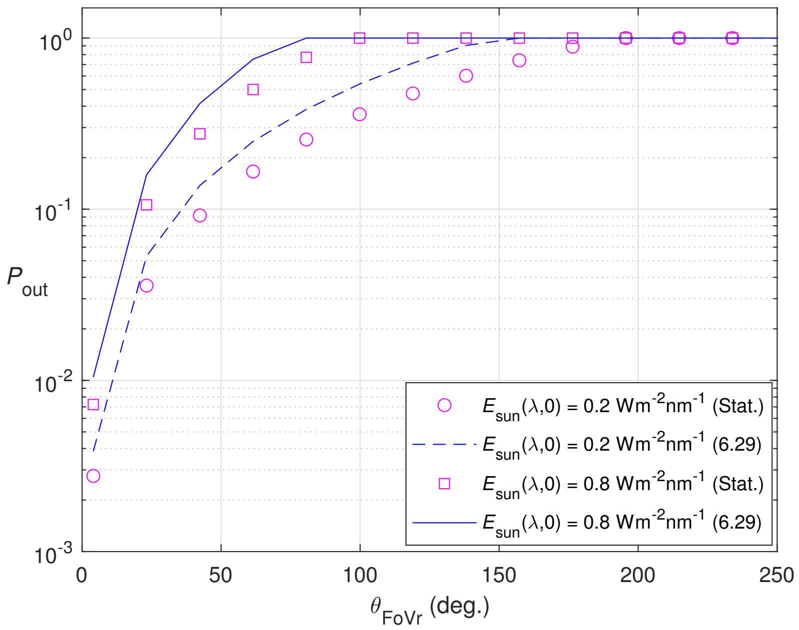

Figure 6.5: Effect of θ_{FoVr} on P_{out} performance using Monte Carlo simulations and analytical method; for $P_{\text{Tx},1} = 4\,\text{W}$, $\xi = 0.4$, $L = 100\,\text{m}$, $w_L = 4\,\text{m}$, $D_r = 75\,\text{mm}$, $\sigma_{\theta t} = 0.4°$, $\sigma_{\theta r} = 1°$, $\sigma_{pt} = 1\,\text{m}$ and $\sigma_{pr} = 1\,\text{m}$.

The relatively small deviations of the results for (Stat.) and (6.29) was because of the assumption that solar noise was negligible at the Rx in the derivation of h_{th} in (B.4) of Appendix B.1. The validity of this point will be examined in Subsection 6.4.3, where solar noise will be considered absent.

In Fig. 6.6, the use of aperture averaging in minimizing the impact of turbulence induced fading on the link performance is shown. As the effect of fading $\sigma_T(D_r)$ increases, the link P_{out} also increases. However, using a PD with a large aperture diameter D_r, the effect of the scintillation on the received signal is largely averaged and $\sigma_T(D_r)$ is reduced (consequently P_{out} is minimized). Hence at D_r = 75 and 35 mm, $\sigma_T(D_r) = 0.0013$ and 0.0264 respectively.

6.4.3 Effect of PEs

In Fig. 6.7 the impact of PEs on the link performance is studied by varying the $\sigma_{\theta\text{t}}$ of the Tx. Note that a large θ_{FoVr} ($\sim 9°$) was considered, hence there was no link interruption. Also, the effect of solar noise was not considered and it can be observed that the (Stat.) results closely matches with that of the (6.29), hence agreeing with the remark in Subsection 6.4.2. In Fig. 6.7(a), for any beam waist at distance L, w_L, as $\sigma_{\theta\text{t}}$ increases so also does the angular misalignment of the Tx, hence it largely points the beam away from the center of the PD (thus the P_{out} increases). However, the impact of PEs on the link performance is reduced at larger beam waist, for $\sigma_{\theta\text{t}} = 0.52°$, $w_L = 4$ and 8 m have P_{out} of 1.1×10^{-3} and 2.7×10^{-6} respectively. This is because despite the same effect of

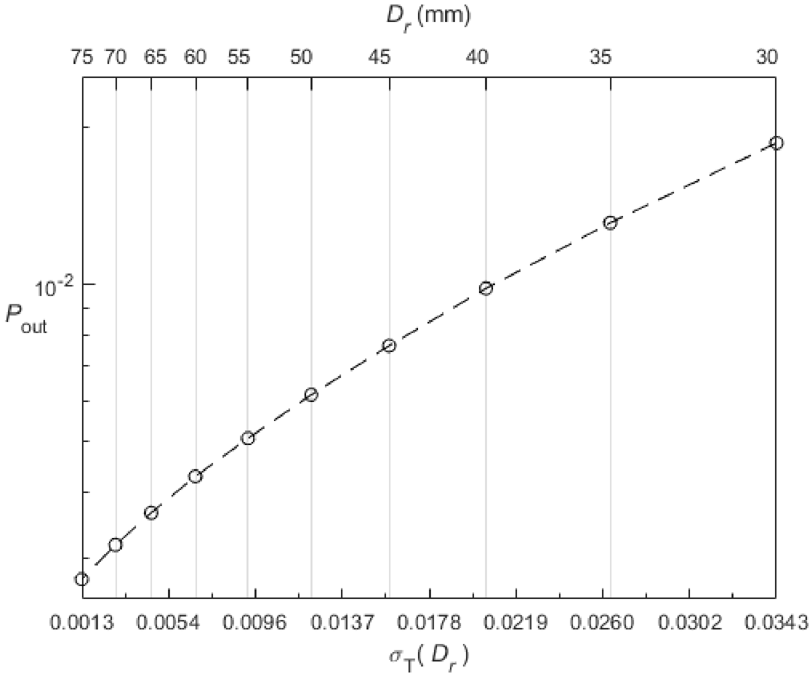

Figure 6.6: Effect of $\sigma_T(D_r)$ and D_r on P_{out} at $E_{\text{sun}}(\lambda,0) = 0.2\,\text{Wm}^{-2}\text{nm}^{-1}$; for $P_{\text{Tx},1} = 4$ W, $\xi = 0.4$, $L = 100$ m, $w_L = 4$ m, $\theta_{\text{FoVr}} = 4°$, $\sigma_{\theta t} = 0.4°$, $\sigma_{\theta r} = 1°$, $\sigma_{pt} = 1$ m and $\sigma_{pr} = 1$ m.

angular misalignment, the larger beam waist casts a wider beam footprint at the Rx plane hence it is closer to the PD center compared to a smaller beam waist. Considering a fixed beam waist $w_L = 4$ in Fig. 6.7(b), results for $D_r = 35$ mm and 75 mm are presented. As expected the link performance is improved for a larger PD aperture size, since there is a larger area to receive the photons incident at the PD, it will collect most photons that would have been lost due to PEs.

Assuming $w_L = 4$, $D_r = 75$ mm, for link ranges of $L = 50$ m and $L = 100$ m, Fig. 6.7(c) shows the trade-off between achievable link distance and the link performance. It will be observed that P_{out} is minimized at a shorter link range at the expense of a longer one. For $\sigma_{\theta\text{t}} = 0.52°$, the P_{out} at $L = 50$ m and $L = 100$ m are 8×10^{-8} and 1.1×10^{-3} respectively. The reduction in P_{out} at $L = 50$ m compared to at $L = 100$ m is due to the former having the Tx and Rx closer, hence less beam spread occurs and more photons are captured by the PD. This also suggests that compared to a longer link distance, a lesser transmit power would be required at a shorter distance to achieve the same P_{out}.

To further study the impact of transmit power in addition with link range on an UWOC system subject to PEs, three systems are considered in Fig. 6.8, namely tracked, untracked with stabilized buoy and untracked with unstabilized buoy systems. The extent of angular misalignments present in the considered systems is dependent on the accuracy of the stability control systems which comes at the expense of cost. Note that the control mechanisms for the systems in Fig. 6.8(a) and Fig. 6.8(b) keeps the highest possible $\sigma_{\theta\text{t}}$ at ~ 0.6° and ~ 2° respectively, while $\sigma_{\theta\text{t}}$ in Fig. 6.8(c) can go above 20°. Also, notice that the effect of large angular misalignments in Fig. 6.8(c) is minimized with a large beam waist $w_L = 30$.

In selecting the appropriate system to deploy, the existing conditions of the operating environment need to be considered, such as with the possible range of $\sigma_{\theta\mathrm{t}}$ (e.g. due to wind speed) if the target P_{out} for a reliable transmission can be achieved. Assuming a low-powered system ($P_{\mathrm{Tx},1}$ = 0.1 W) requires a target P_{out} of 1×10^{-3}, a reliable transmission can only be realized for $\sigma_{\theta\mathrm{t}}$ less than 0.23°, 0.7° and 10° in a tracked, untracked with stabilized buoy and untracked with unstabilized buoy systems respectively. In Fig. 6.8(a) for $\sigma_{\theta\mathrm{t}} = 0.6°$ the P_{out} is 5×10^{-2}, when compared to Fig. 6.8(b) with 1×10^{-3} at 0.7°, the interest of using the former system would be based on the larger achievable link range (100 m). Also, considering the simple and low-cost system in Fig. 6.8(c) comes with the compromise of operating within a short link range (20 m). Hence, while designing a low-powered system a trade-off of the maximum achievable link range for a target P_{out} has to be considered. Furthermore, as expected in all the cases, increasing the transmit power results in an increase in the achievable link range. However, note that most of these UWOC systems are powered by batteries, as such low power consumption for a long period of operation would be very desirable.

6.4.4 Effect of link interruption

All through the previous results, a large Rx FoV have been considered (i.e., the angle-of-arrival θ_{a} of the received signal was always less than θ_{FoVr}), hence there was no interruption in the link. For this case of no link interruption (unlimited Rx FoV), the derived closed-form of P_{out} in (6.29) is valid.

In Fig. 6.9, considering a tracked system, the impact of link interruption is investigated for different θ_{FoVr} across a given range of $\sigma_{\theta\mathrm{t}}$. Considering the parameters in Fig. 6.9, a distribution of θ_{a} from (6.24) and (6.25) is given in Fig. 6.10, for insight into the link interruption effect ($\theta_{\mathrm{a}} > \theta_{\mathrm{FoVr}}$) of any selected θ_{FoVr}. In Fig. 6.9(a), the considered θ_{FoVr} (2.3°) is larger than the range of significant θ_{a} in Fig. 6.10, hence there is a perfect match between (Stat.) and (6.29). As θ_{FoVr} is reduced to 1.15° in Fig. 6.9(b), link interruption will occur severely at θ_{a} closer to 1.15°. This affected range of θ_{a} corresponds to $\sigma_{\theta\mathrm{t}} > 0.25°$ (limited θ_{FoVr} region), hence there is a deviation between (Stat.) and (6.29) within this range [2]. However, (Stat.) and (6.29) still matches at $\sigma_{\theta\mathrm{t}}$ less than 0.25° since the for the corresponding range of θ_{a}, the selected θ_{FoVr} is unlimited. The same trend is observed in Fig. 6.9(c) as θ_{FoVr} is lowered from 1.15° to 0.6°, the limited θ_{FoVr} region increases. In conclusion, as the Rx FoV is limited, the performance of the link deteriorates due to the occurence of link interruption.

---

[2] Notice that (6.29) is always false in the limited θ_{FoVr} region.

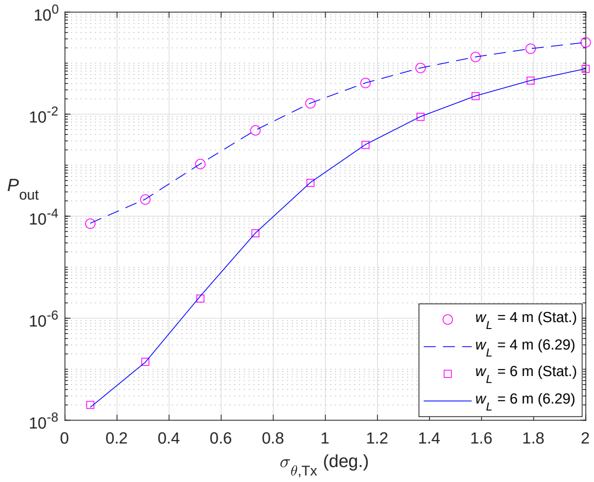

(a) Beam waist

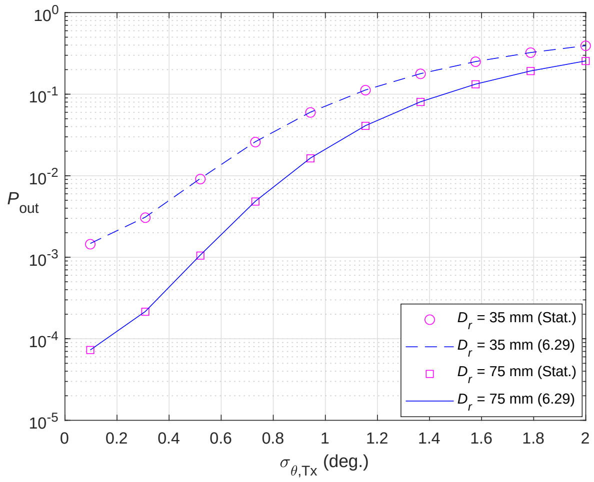

(b) Aperture diameter

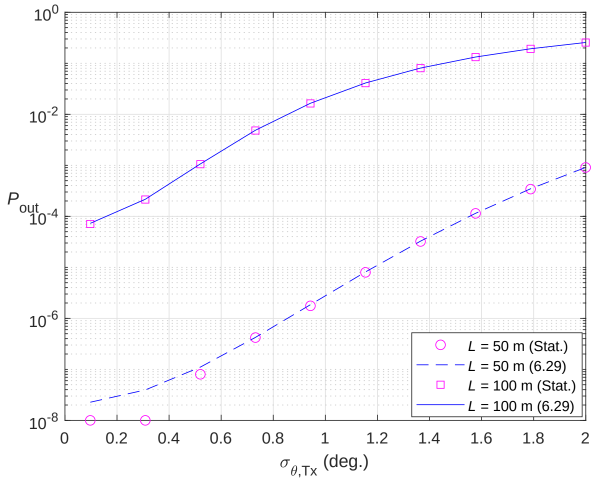

(c) Link range

Figure 6.7: Effect of PEs on P_{out} performance; for $P_{\text{Tx},1} = 4\,\text{W}$, $\xi = 0.4$, $\theta_{\text{FoVr}} = 9^\circ$, $\sigma_{\theta r} = 1^\circ$, $\sigma_{pt} = 1\,\text{m}$ and $\sigma_{pr} = 1\,\text{m}$; (a) $D_r = 75\,\text{mm}$, $L = 100\,\text{m}$; (b) $w_L = 4\,\text{m}$, $L = 100\,\text{m}$; (c) $w_L = 4\,\text{m}$, $D_r = 75\,\text{mm}$.

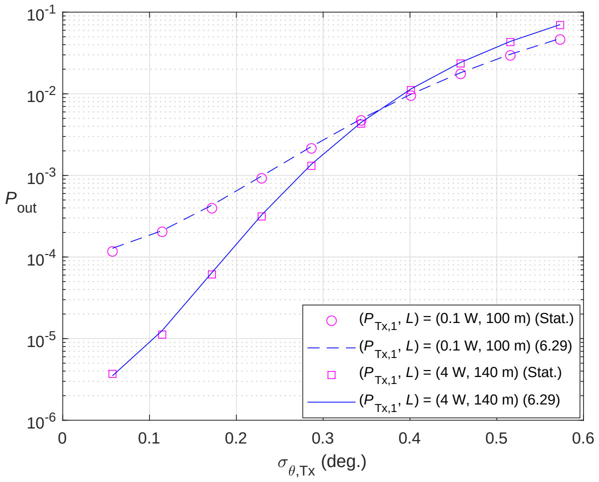

(a) Tracked system

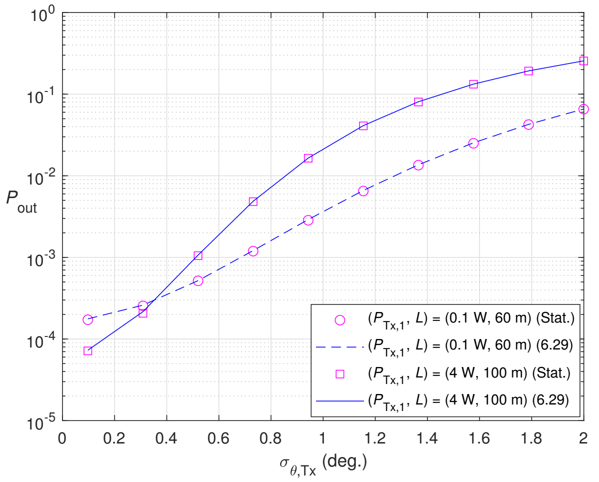

(b) Untracked with stabilized buoy system

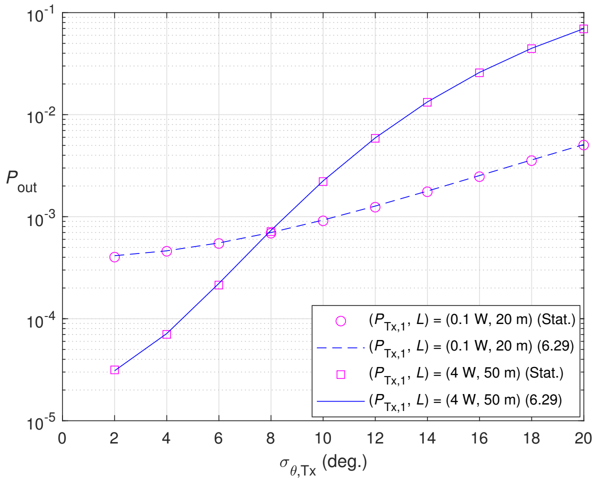

(c) Untracked with unstabilized buoy system

Figure 6.8: Impact of PEs on choice of transmit power and link range; for $\xi = 0.4$, $D_r = 75\,\text{mm}$; (a) $w_L = 4\,\text{m}$, $\theta_{\text{FoVr}} = 2.3°$, $\sigma_{\theta r} = 0.06°$, $\sigma_{pt} = 0.5\,\text{m}$ and $\sigma_{pr} = 0.5\,\text{m}$; (b) $w_L = 4\,\text{m}$, $\theta_{\text{FoVr}} = 9°$, $\sigma_{\theta r} = 1°$, $\sigma_{pt} = 1\,\text{m}$ and $\sigma_{pr} = 1\,\text{m}$; (c) $w_L = 30\,\text{m}$, $\theta_{\text{FoVr}} = 69°$, $\sigma_{\theta r} = 1°$, $\sigma_{pt} = 10\,\text{m}$ and $\sigma_{pr} = 1\,\text{m}$.

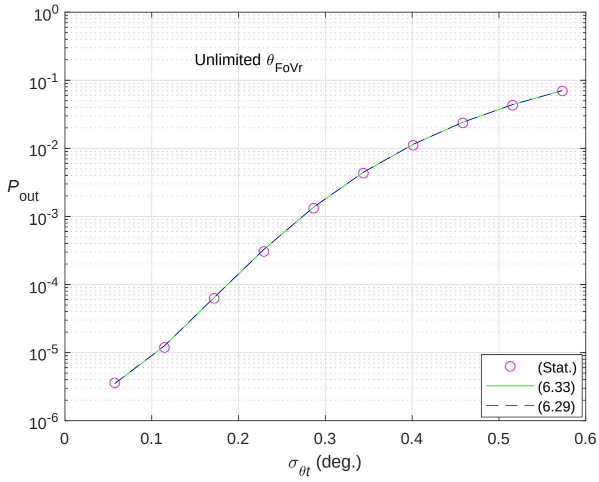

(a) $\theta_{\mathrm{FoVr}} = 2.3°$

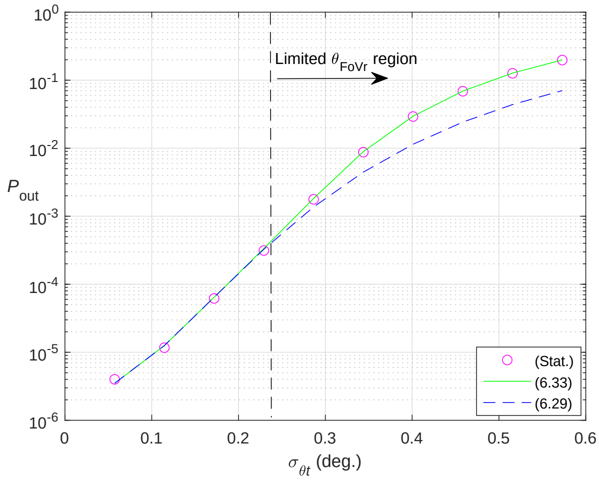

(b) $\theta_{\mathrm{FoVr}} = 1.15°$

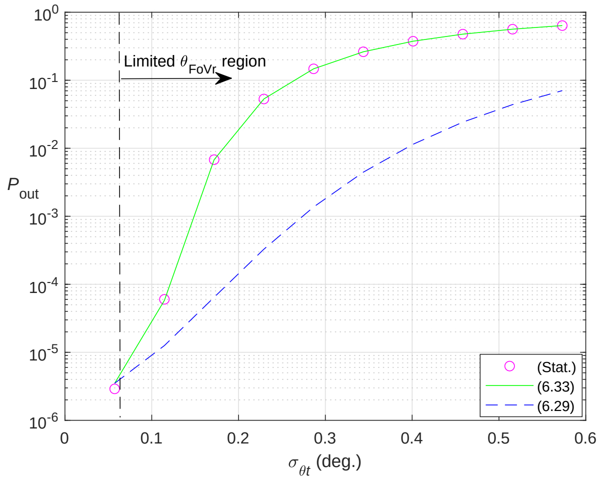

(c) $\theta_{\mathrm{FoVr}} = 0.6°$

Figure 6.9: Impact of limited Rx FoV θ_{FoVr} on P_{out}; for $P_{\mathrm{Tx},1} = 4\,\mathrm{W}$, $\xi = 0.4$, $w_L = 4\,\mathrm{m}$, $L = 140\,\mathrm{m}$, $\sigma_{\theta r} = 0.06°$, $\sigma_{pt} = 0.5\,\mathrm{m}$ and $\sigma_{pr} = 0.5\,\mathrm{m}$.

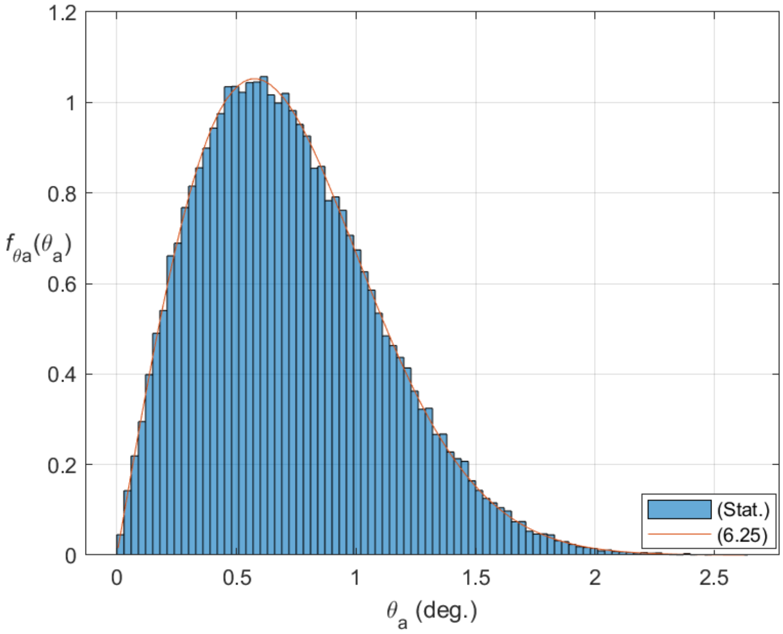

Figure 6.10: Distribution of θ_a for a tracked system; for $\sigma_{\theta t} = 0.6°$ and $\sigma_{\theta r} = 0.06°$.

6.4.5 Parameter Optimization

Figure 6.11 shows the 3D plot of simulation results for P_out with varying w_L and θ_FoVr. A minimum P_out of 1.1×10^{-3} is realized at $w_L = 3.76$ m and $\theta_\text{FoVr} = 0.4°$, referred to as optimum parameter values and denoted as $w_{L,\text{opt}}$ and $\theta_\text{FoVr,opt}$. Using (6.33), minimum P_out was solved analytically as a function with two variables w_L and θ_FoVr, using the non-derivative method, 'minsearch' from MATLAB. Table 6.2 shows the results of Tx-Rx parameter optimization using both the simulation and analytical methods. It will be observed that the both methods have a uniform trend of obtained values for change of certain parameters. Also, there are minimum differences in the results from the two methods which are negligible and can be attributed to the assumptions made prior to the derivation of (6.33).

In Table 6.2(a), the results for the impact of parameter optimization on PEs are given. It will be observed as $\sigma_{\theta t}$ is varied from 0.06° to 0.29° the optimum beam width $w_{L,\text{opt}}$ becomes more directed (3.76 m to 3.39 m) hence reducing geometric loss and the probability of a large portion of the beam footprint at the Rx plane being outside the light collection area. Also, this increased effect of link mislignment is compensated with increased optimum Rx FoV $\theta_\text{FoVr,opt}$ (0.4° to 0.97°).

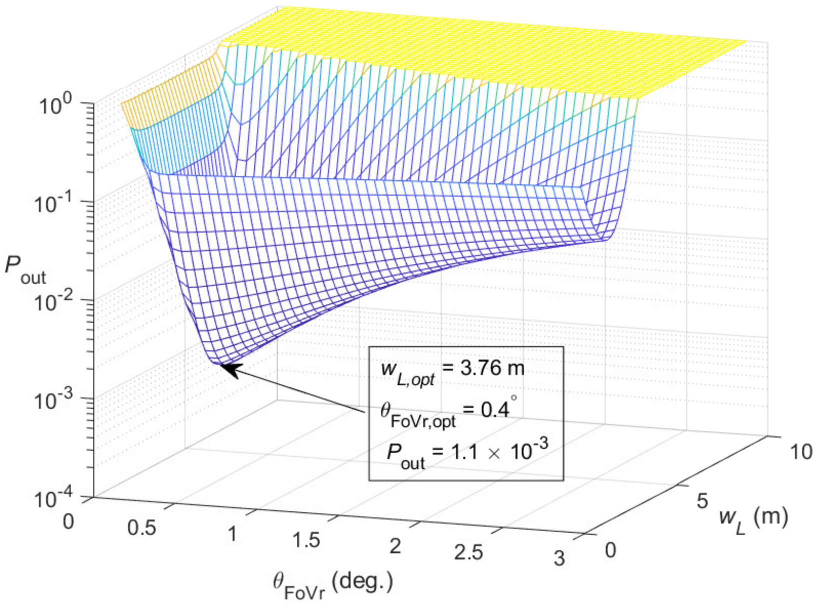

Figure 6.11: Link parameter optimization on P_{out} for $P_{\text{Tx},1} = 80\,\text{mW}$, $\xi = 0.4$, $\sigma_{\theta t} = 0.06°$, $\sigma_{\theta r} = 0.06°$, $\sigma_{pt} = 0.5\,\text{m}$, $\sigma_{pr} = 0.5\,\text{m}$, $E_{\text{sun}}(\lambda, 0) = 0.2\ \text{Wm}^{-2}\text{nm}^{-1}$ and $L = 100\,\text{m}$.

Table 6.2: Link parameter optimization on P_{out} for $P_{\text{Tx},1} = 80\,\text{mW}$, $\xi = 0.4$, $\sigma_{\theta r} = 0.06°$, $\sigma_{pt} = 0.5\,\text{m}$ and $\sigma_{pr} = 0.5\,\text{m}$; (a) $E_{\text{sun}}(\lambda, 0) = 0.2\ \text{Wm}^{-2}\text{nm}^{-1}$, $L = 100\,\text{m}$; (b) $\sigma_{\theta t} = 0.06°$, $L = 100\,\text{m}$; (c) $\sigma_{\theta t} = 0.06°$, $E_{\text{sun}}(\lambda, 0) = 0.2\ \text{Wm}^{-2}\text{nm}^{-1}$.

(a) Impact on Pointing Errors

$\sigma_{\theta t}$ (deg.)	Simulation			Analytical		
	$w_{L,\text{opt}}$	$\theta_{\text{FoVr,opt}}$ (deg.)	P_{out}	$w_{L,\text{opt}}$	$\theta_{\text{FoVr,opt}}$ (deg.)	P_{out}
0.06	3.76	0.4	1.1×10^{-3}	3.69	0.36	1.3×10^{-3}
0.17	3.57	0.69	5.5×10^{-3}	3.42	0.68	7.9×10^{-3}
0.29	3.39	0.97	2.75×10^{-2}	3.2	0.95	3.82×10^{-2}

(b) Impact on Solar Noise

$E_{\text{sun}}(\lambda, 0)\,(\text{Wm}^{-2}\text{nm}^{-1})$	Simulation			Analytical		
	$w_{L,\text{opt}}$	$\theta_{\text{FoVr,opt}}$ (deg.)	P_{out}	$w_{L,\text{opt}}$	$\theta_{\text{FoVr,opt}}$ (deg.)	P_{out}
0.1	3.76	0.4	8.6×10^{-4}	3.76	0.37	1×10^{-3}
0.3	3.76	0.34	1.2×10^{-3}	3.64	0.35	1.6×10^{-3}
0.8	3.57	0.34	2.2×10^{-3}	3.45	0.32	3.3×10^{-3}

(c) Impact on Link Range

L (m)	Simulation			Analytical		
	$w_{L,\text{opt}}$	$\theta_{\text{FoVr,opt}}$ (deg.)	P_{out}	$w_{L,\text{opt}}$	$\theta_{\text{FoVr,opt}}$ (deg.)	P_{out}
120	1.73	0.34	2.35×10^{-1}	1.71	0.3	2.4×10^{-1}
110	2.47	0.34	4.13×10^{-2}	2.54	0.32	4.37×10^{-2}
105	3.02	0.34	9.1×10^{-3}	3.07	0.33	1.02×10^{-2}

6.5 Chapter summary

In this chapter, we have considered a vertical UWOC link subject to oceanic turbulence and PEs. Aperture averaging was adopted to mitigate the effect of turbulence at the Rx lens aperture. In our presented results, we have discussed how the link performance is affected by solar noise due to an increase in the Rx FoV. The impact of turbulence and PEs are considerably reduced for larger PD size. Also analyzed was how the divergence angle of the beam and link range could relax the effect of PEs on the link performance. The trade-off between power consumption and achievable communication range was discussed in terms of system complexity and cost. The interest of these system parameters in improving the link performance could be optimized (optionally as discussed in Chapter 5) especially during UWOC system design. Given that our study of the UWOC so far has been based on simulations, in the next chapter, we will carry out some experimental demonstration of the UWOC system.

Chapter 7

Experimental Work

Contents

7.1 Introduction

In the preceding chapters, our performance evaluation of the UWOC system has been mostly simulation-based. This prompts our aim in this chapter, to practically demonstrate the feasibility of deploying an UWOC system, and to assess the different practical considerations. We have developed an experimental test-bed in a lab and conducted a series of preliminary experiments. We experimentally demonstrated signal transmission through a 4 m UWOC link based on light reflections in a 1 m water tank. A measure of the power loss in transmission is done to assess the signal attenuation imposed by the water quality. In particular, we studied the frequency response of the entire transmission system to assess the impact of the Tx-Rx components and the aquatic channel on it.

The subsequent sections of this chapter are organized as follows. The description of the experimental setup and the components is provided in Section 7.2. Then, in Section 7.3, we demonstrated signal transmission and carried out experimental measurements and analysis of the power loss in transmission and the end-to-end channel frequency response of the system. Finally, Section 7.4 concludes this chapter.

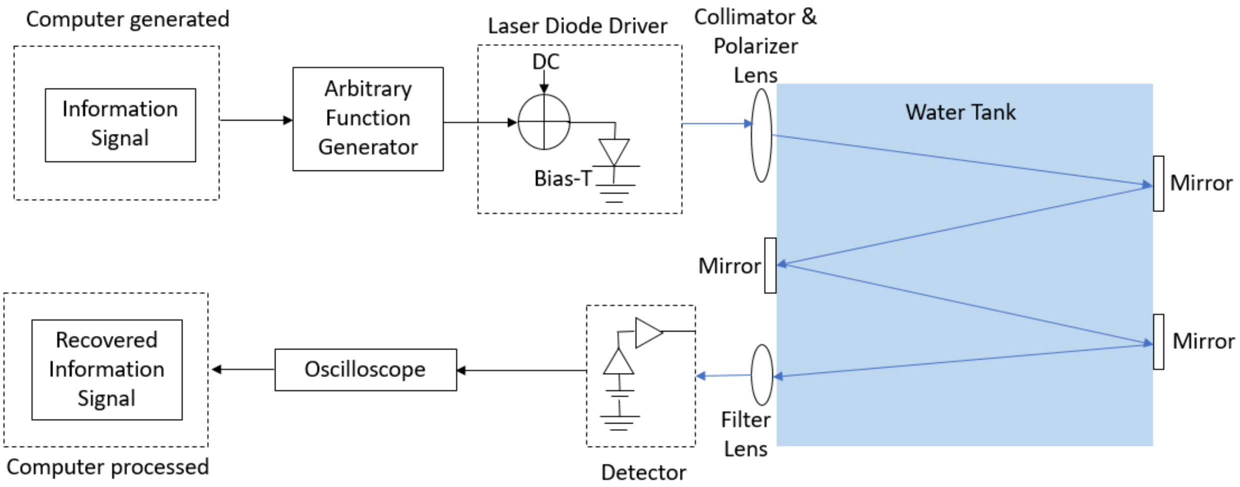

Figure 7.1: Experimental setup for the UWOC link.

7.2 Experimental setup

For the experiments, a perfectly aligned UWOC link is set up as depicted with a schematic diagram in Fig 7.1. The Tx side is comprised of a laptop computer with signal processing capabilities e.g. with MATLAB®, an arbitrary function generator (AFG) from Tektronix (AFG1022), a 450 nm blue LD (Thorlabs LP450-SF15) used as the light source, and an LD driver (Thorlabs CLD1010LP) with a temperature control system. Using the computer, we generate the information signals, which are fed into the AFG. The AFG generates the electrical signals which are combined with a DC bias using a bias-tee circuit in the LD driver to modulate the LD; hence, converting the electrical signal into an optical signal. The optical signal is then collimated using a collimator (Thorlabs CFC8-A) to narrow its divergence angle and horizontally polarized using a polarizer (Thorlabs LPVISE100-A) to minimize the reflections at the surface of the water tank as it propagates through the UWOC channel. Our water tank of glass thickness 1 cm, is of dimension 1 m × 0.6 m × 0.4 m, and filled with tap water. The optical path length is extended to 4 m using 3 pieces of reflective mirrors (Thorlabs broadband dielectric mirror - BB07-E02) fixed outside both ends of the tank.

At the Rx side, a band pass filter (Thorlabs filter wheel station - FW1A) is used to moderate the amplitude of the received optical signal, which is then detected and converted into an electrical signal by an MPPC module (Hamamatsu C13366-3050GA) [173]. The module among many other circuits comprises a TIA circuit and a temperature control circuit. The MPPC signal output is connected to a digital storage oscilloscope (Keysight DSOX1204G) for data acquisition, visualization and analysis. Finally, signal detection and demodulation is performed offline using MATLAB®. Snapshots of our developed test-bed are given in Fig 7.2.

In the following section, we will discuss the operational capability of our test-bed. We will show the signal realized at the Rx, and further extract data from it for an insightful analysis of our system. In the course of the experiments, the operating conditions of the LD driver were set at;

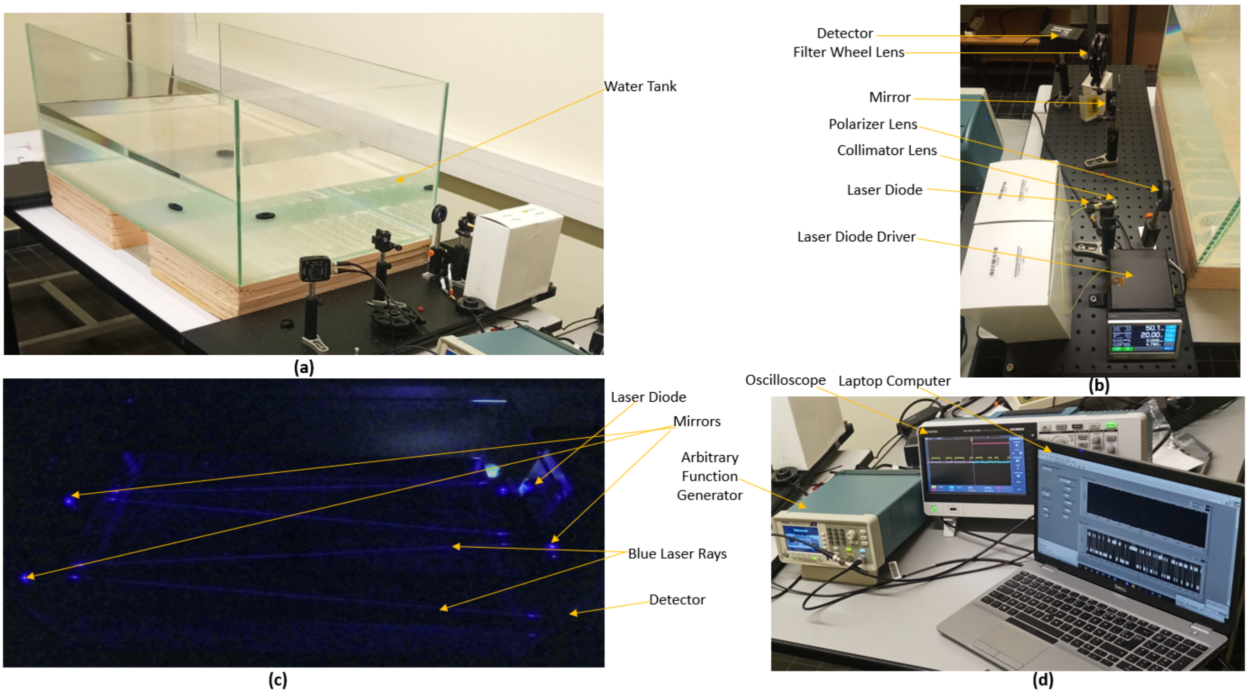

Figure 7.2: Snapshots of the test-bed: (a) water tank, (b) transceiver components, (c) blue light paths, (d) electronic devices.

current - 50 mA, voltage - 4.785 V, and temperature - 20 °C.

7.3 Measurements and analysis

Herein, we present the measurements from our experiments and discuss the results. In particular, we experimentally study the loss in signal intensity through the channel and also the frequency response of the system.

7.3.1 Signal transmission

Firstly in the evaluation of our transmitted optical signal, using a Nova handheld laser power meter from Ophir Optronics, we measured the power from the LD output (7.7 mW) to the input of the PD (1.47 mW). This measurement was done outside the water tank, over each 1 m optical path, for both the incident and reflected light ray on and from the mirrors respectively. The power at the output of the polarizer is 3.17 mW, on average, a 99 % loss of the incident light on the mirrors was measured as the reflected light, also the power loss from air-to-glass was 91 %. The interest of these power measurements was further explored to assess the water type of our UWOC link by estimating the diffuse attenuation coefficient K_d from the power decay BL model as:

$$P_\mathrm{r} = P_\mathrm{t} \exp\left(-L K_\mathrm{d}\right), \tag{7.1}$$

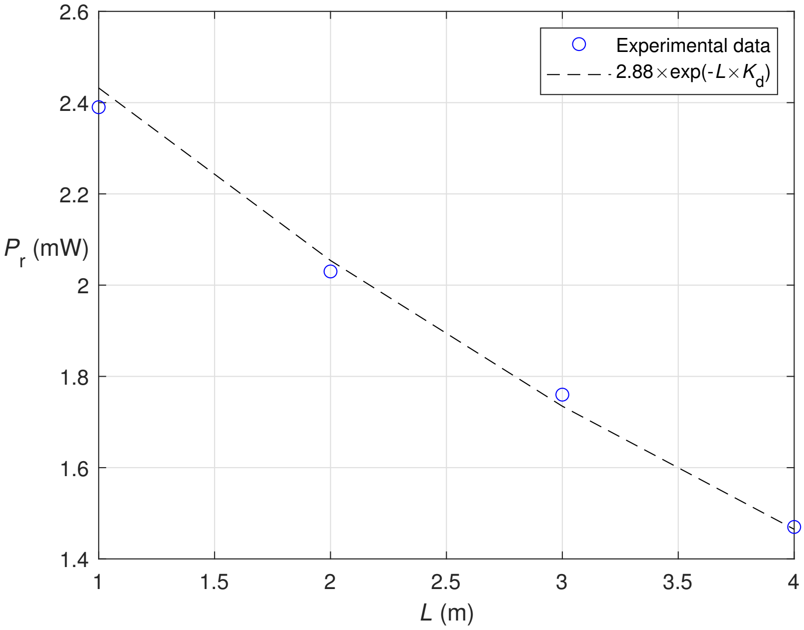

Figure 7.3: Received power P_r as a function of link range L.

where P_t is the transmitted power and P_r is the received power over an optical path of length L. The loss from both the glass and the mirrors were already removed from P_t and P_r. In Fig. 7.3, a plot of the measured P_r is given against distance L, then curve fitting is done using (7.1) to ascertain the estimate of K_d. Note, at the beginning of the first 1 m optical path, P_t inside the glass water tank was calculated to be 2.88 mV (91 % of 3.17 mW). During curve fitting, the estimated K_d was 0.169 m^{-1}, which for our LD wavelength of 450 nm, falls between Jerlov I and II water classifications for clear waters [174, 34].

7.3.2 Aggregate channel frequency response

After our study of the attenuation of the transmitted optical signal by the water properties, we measured the aggregate channel frequency response, $H(f)$, which includes the effects of the LD, the aquatic channel, and the MPPC PD. The measurement of the $H(f)$ was done by transmitting sinusoidal signals with different frequencies, from 100 kHz to 20 MHz (using the frequency analysis feature of Keysight DSOX1204G oscilloscope). Experimental results are shown in Fig. 7.4 for the magnitude $|H(f)|$ of the frequency response (in dB). It could be observed that the system has a bandpass frequency response with -3 dB low and high cut-off frequencies at 100 kHz and 4.2 MHz, respectively. The low cut-off frequency of the system is caused by the LD driver, which has a response starting from 200 kHz to more than 1 GHz [175]. The high cut-off frequency of the system results from the bandwidth limitation of the MPPC which has a -3 dB cut-off frequency at 4 MHz [173].

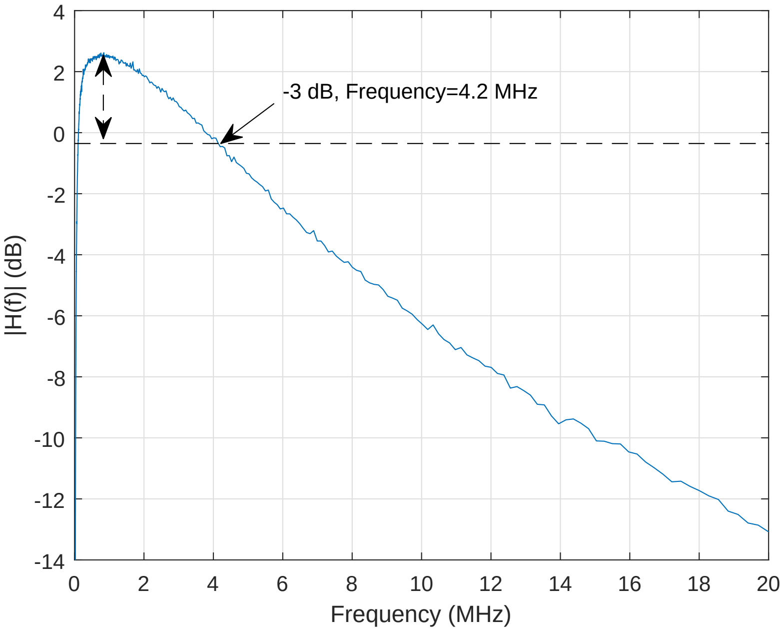

Figure 7.4: Frequency response of the transmission system.

7.4 Chapter summary

In this chapter, we experimentally demonstrated the feasibility of deploying an UWOC system. We provided a description of the test-bed used and studied its performance by carrying out some preliminary experimental measurements on the UWOC link and some insightful results were realized and discussed. In particular, the optical path loss through the aquatic medium was evaluated and the water type confirmed. Also, the frequency of the UWOC system was investigated and it was realized that the MPPC component imposes a significant limitation on the system performance.

Chapter 8

Conclusions and Perspectives

Contents

8.1 Conclusions

UWOC is considered as an efficient complementary transmission technology to acoustic communications for short-to-moderate link ranges, allowing for high data-rate and low latency transmissions. However, there exist several practical challenges that limit the performance of UWOC links. Among these, link misalignments and oceanic turbulence are problematic in UWOC applications, thus necessitating efficient techniques for mitigating them. Other issues include accurate modeling of signal degradation due to water absorption and scattering, solar background noise effect, as well as developing efficient transmission techniques to ascertain the reliability of the communication link. On the other hand, in order to increase the link range, the use of highly sensitive PDs at the Rx is of particular interest. In this thesis, we focused on investigating, both through simulation and analytically, the random effects of the aquatic channel due to link misalignments and oceanic turbulence considering an SiPM-based Rx. We also studied the interest of appropriate selection of the Tx/Rx parameters to reduce the impact of these random effects on the link performance.

In line with the above, in Chapter 2, we presented an overview of the UWOC technology, highlighting the various system components and challenges in deployment. Due to the importance in achieving long range transmissions, we provided in Chapter 3 a brief study of the SiPM-based Rxs in UWOC systems. Also, a brief state-of-the-art on the impact of link misalignments and turbulence in UWOC systems was presented in Chapter 4.

Our main contributions in this thesis concentrate on Chapters 5 and 6. In Chapter 5, we studied the effect of link misalignments on a vertical UWOC link using an LED light source and an SiPM at the Rx, which to the best of our knowledge is done for the first time. We considered the practical scenario for downlink and uplink transmission between a buoy and an AUV, and took into account the effects of sea surface roughness and underwater currents. For this latter, and also to consider AUV angular misalignments, we used realistic mathematical models. We developed the statistical distribution of the link and used it to numerically evaluate the performance of the link, hence avoiding long Monte Carlo simulations. We lastly verified the impact the system parameters have in improving the system performance. In our presented analysis, it was observed that a substantial improvement in the link performance can be obtained by optimizing the main link parameters, namely the Tx Lambertian order and the Rx FoV. The corresponding optimal parameters depend on the channel and link characteristics including the sea-surface wind speed, AUV stability and positioning accuracy, and the received power. Note that the received power depends on the link range (here, the operating depth of the AUV) and the transmit power, for which the dependence of the optimal parameters was shown.

In practice, these link parameters can be estimated either at the Tx or at the Rx and be shared with the other side of the link in real time in order to adapt Tx-Rx parameters. This assumes, of course, a bi-directional transmission between the two ends of the link. Note that in the case that one of the terminals is not equipped with an optical transmitter, sending the estimated channel parameters to the other side of the link can be done using an acoustic link given the corresponding required low data rate. The buoy can use a gyroscope or an accelerometer in order to estimate the underlying conditions (i.e., the wind surface speed) in real time. Also, depending on the positioning system used by the AUV and the operational conditions, the displacement and angular misalignment variances can be estimated. Lastly, given the estimated link parameters, the Tx beam divergence can be adjusted using a diffuser in front of the LED, whereas the Rx FoV can be changed using a mechanical iris in front of the Rx lens. For practical implementation, the Tx beam-width and the Rx FoV could be selected amongst a discrete set of available values (using the closest values to the optimally calculated ones).

In Chapter 6, still for an SiPM-based Rx but with a LD light source, we investigated the impact of PEs and turbulence on the performance of a vertical UWOC link using a more complete model. For this, we accurately modelled the effect of oceanic turbulence on an inhomogeneous vertical link. Also, we considered the effect of background noise from solar radiation. The statistical distribution of the link taking into account the effect of aperture averaging was developed and used to derive the analytical expression of the performance evaluation metric, P_{out}. Lastly, we studied the effect of the various considered system parameters on link performance.

Lastly, in Chapter 7 we presented a set of preliminary experimental works to assess the different practical components of establishing an UWOC link.

8.2 Perspectives

This thesis was dedicated to the performance study of vertical UWOC links subject to misalignments and oceanic turbulence, and the interest of improving the link reliability by system parameter optimization. The work carried out in this thesis meets the thesis objectives outlined in Chapter 1. However, there remain several other aspects worthy of future investigations as discussed below.

Some practical challenges existing in deployed UWOC links were considered in this thesis. However, it will be necessary to consider the impact of shadowing and physical obstructions (e.g. from marine life or activities) on the link performance as it cannot always be avoided and to a great extent, they determine the reliability of the data transmission. Due to the complexities of the aquatic channel (e.g. from absorption, scattering, turbulence, etc.), studying the aforementioned practical constraints in terms of channel modeling and practical experiments especially in a real underwater environment is very challenging. This necessitates research in carrying out standard UWOC experiments in real environments, accurate/realistic channel modeling, documenting and making available significant ocean data [176].

Although this thesis considered a vertical LOS UWOC link, it is just among the few research works in that domain as most literature are devoted to investigating horizontal links. However, given the stratified properties of the vertical aquatic channel, such as the changes in temperature and salinity at various depths, it is very necessary to carefully study the vertical UWOC links. Also, this imposes more requirements for the modeling, simulation and deployment of vertical UWOC links [176]. Some of the existing research for vertical links have explored the chlorophyll concentration [177], the impact of solar noise [19] and the performance evaluation for inhomogeneous LOS and NLOS scenarios [178]. Despite all these, there are still relevant research gaps to be filled in vertical UWOC links.

We investigated the interest of LD, LED and SiPM in improving the UWOC link performance. There is still an essential need for enhanced optical sources and PDs, capable of meeting the demands of UWOC systems with reliable long-range transmission at a high-data rate. Especially components with high efficiency, low noise, large bandwidth, low latency and high sensitivity. In [179], the potentials of hybrid LD- and LED-based UWOC systems was investigated. It will be of further research interest, to develop intelligent adaptive UWOC transceivers with the capability of mitigating varying practical challenges. For instance, given the shift in the minimum absorption range of optical wavelengths in varying underwater environments (e.g. for pure sea water towards the shore is from the blue-green wavelengths to the yellow-green region), reliable and efficient communication can be maintained by employing an adaptive scheme with tunable wavelengths [1, 180]. This technique is also applicable in mitigating the impact of turbulence on an UWOC network of mobile sensor nodes existing in river meets ocean environment [181]. Potentially, multiplexing signals on different wavelengths to improve the link throughput can be achieved with optical sources of varying wavelengths [29].

We had considered an uncoded OOK modulation in this thesis, but it will be important to explore more efficient signaling techniques with enhanced modulation and coding schemes especially with energy-efficient capabilities as most practical UWOC systems will be powered by batteries for a long duration. Also worthy to be explored are higher spectral efficiency signaling schemes, to ensure an increase in data rate over system bandwidth limitation [62, 61].

More importantly, the recent popularity of artificial intelligence in various fields should be extensively leveraged to address some of the issues in UWOC systems. Several existing works have explored the use of machine learning and computer vision in UWOC for areas such as improved signal detection [182], efficient modulation recognition [183], improved channel classification [184], smart routing protocol [185], mitigation of link misalignment [186], enhanced decoding process for turbulence-induced fading [187] and adaptive transmission scheme [188]. The continuance of quality research on artificial intelligence in UWOC will to a great extent improve the technology.

Appendix A

A.1 Derivation of the scintillation index taking into account aperture averaging

Considering a circular lens of diameter D_r, the scintillation index corresponding to the k^{th} layer, denoted by $\sigma^2_{I_\mathrm{k}}(D_r)$, is given by [165]:

$$\begin{aligned}\sigma^2_{I_\mathrm{k}}(D_r) = 8\pi^2\mathcal{K}^2 L_{T_k} \int_0^1 \int_0^\infty & \kappa\,\Phi_{n_k}(\kappa) \\ & \times \exp\left\{ -\frac{L_{T_k}\kappa^2}{\mathcal{K}} \frac{\left[\left(1-\bar{\Theta}_{1_k}\xi\right)^2 + \wedge_{1_k}\Omega_{G_k}\xi^2\right]}{\left(\Omega_{G_k}+\wedge_{1_k}\right)} \right\} \\ & \times \left\{ 1 - \cos\left[\frac{L_{T_k}\kappa^2}{\mathcal{K}} \frac{\left(\Omega_{G_k}-\wedge_{1_k}\right)}{\left(\Omega_{G_k}+\wedge_{1_k}\right)} \xi\left(1-\bar{\Theta}_{1_k}\xi\right) \right] \right\} d\kappa\, d\xi,\end{aligned} \tag{A.1}$$

where κ is the magnitude of the spatial frequency, $\Phi_{n_k}(\kappa)$ is the spatial power spectrum model of oceanic turbulence for the k^{th} layer, $\Omega_{G_k} = 16L_{T_k}/\mathcal{K}D_r^2$ is a dimensionless parameter characterizing the spot radius of the Rx lens, $\wedge_{1_k} = \wedge_{0_k}/(\Theta^2_{0_k} + \wedge^2_{0_k})$, $\wedge_{0_k} = L_{T_k}/\mathcal{K}\alpha_s^2$, $\Theta_{0_k} = 1 - L_{T_k}/F_0$, the radius of curvature is set as $F_0 = \infty$ which corresponds to a collimated beam with source size α_s, $\bar{\Theta}_{1_k} = 1 - \Theta_{1_k}$ and $\Theta_{1_k} = \Theta_{0_k}/(\Theta^2_{0_k} + \wedge^2_{0_k})$. The corresponding k^{th}-layer turbulence power spectrum is given by [189]:

$$\begin{aligned}\Phi_{n_k}(\kappa) = & \left(4\pi\kappa^2\right)^{-1} C_0 \left(\frac{\alpha_k^2 \mathcal{X}_T}{\omega_k^2}\right) \epsilon^{-1/3} \kappa^{-5/3} \left[1 + C_1\left(\kappa\eta_k\right)^{2/3}\right] \\ & \times \begin{bmatrix} \omega_k^2 \exp\left(-C_0 C_1^{-2} P_{T_k}^{-1} \delta_k\right) \\ + d_{r_k} \exp\left(-C_0 C_1^{-2} P_{S_k}^{-1} \delta_k\right) \\ -\omega_k\left(d_{r_k}+1\right) \exp\left(-0.5 C_0 C_1^{-2} P_{TS_k}^{-1} \delta_k\right) \end{bmatrix},\end{aligned} \tag{A.2}$$

where ϵ is the dissipation rate of kinetic energy per unit mass of fluid, $\mathcal{X}_T$ is the dissipation rate of mean-squared temperature. The constants C_0 and C_1 are equal to 0.72 and 2.35, respectively. Further defined are the parameters specific to the k^{th} layer. The Prandtl numbers for temperature and salinity are given by $P_{T_k} = \upsilon_k D_{T_k}^{-1}$ and $P_{S_k} = \upsilon_k D_{S_k}^{-1}$, respectively, where υ_k is the kinematic viscosity, and D_{T_k} and D_{S_k} are molecular diffusivity of temperature and salinity, respectively. The term P_{TS_k} is one-half of the harmonic mean of P_{T_k} and P_{S_k}. Also, $\delta_k = 1.5C_1^2\left(\kappa\eta_k\right)^{2/3} + C_1^3\left(\kappa\eta_k\right)^2$, where $\eta_k = \left(v_k^3/\epsilon\right)^{1/4}$ is the Kolmogorov micro-scale length.

Furthermore, ω_k in (A.2) denotes the relative strength of temperature and salinity fluctuations. Considering $(dT0/dz)_k$ and $(dS0/dz)_k$ as the temperature and salinity differences between top and bottom boundaries of the k^{th} layer, respectively, then [190, 191, 192]:

$$\omega_k = \frac{\alpha_k(dT0/dz)_k}{\beta_k(dS0/dz)_k}, \tag{A.3}$$

where α_k is the thermal expansion coefficient and β_k is the saline contraction coefficient. Lastly, the eddy diffusivity ratio d_{r_k} in (A.2) is given by [190, 191, 192]:

$$d_{r_k} \approx \begin{cases} |\omega_k|\Big(|\omega_k| - \sqrt{|\omega_k|\big(|\omega_k|-1\big)}\Big)^{-1}, & |\omega_k| \geq 1 \\ 1.85|\omega_k| - 0.85, & 0.5 \leq |\omega_k| \leq 1 \\ 0.15|\omega_k|. & |\omega_k| < 0.5 \end{cases} \tag{A.4}$$

Appendix B

B.1 Derivation of the h threshold h_{th} for an UWOC system affected by solar noise

Assuming shot noise is the dominant noise at the Rx, it implies a large PD gain G, which is true for the SiPM (in the order of 10^6). Therefore in the OOK signaling, a relatively large extinction ratio ξ is used, which implies that even for "off" OOK symbols, the thermal, dark and solar noises are negligible compared with the corresponding signal-dependent shot noise.

As a result of the above assumptions, given that $\mathcal{R}_{\text{e}}\, P_{\text{Tx}_0}\, h = \mathcal{R}_{\text{e}}\, \xi\, P_{\text{Tx}_1}\, h$ (with the denotations $I_{s,0} = \xi\, I_{s,1}$), we set $\breve{r}_0 \approx \xi\, \breve{r}_1$ and also $\sigma^2_{n_0} \approx \xi\, \sigma^2_{n_1}$. Hence, the expression for the optimal thresholding for signal detection (5.8) can be reduced to:

$$\begin{aligned} \gamma_{\text{th}} &\approx R_{\text{L}} \sqrt{\xi\, I^2_{s,1} - \frac{\xi\, \sigma^2_{n_1}}{1-\xi} \log \xi} \\ &\approx R_{\text{L}}\, I_{s,1} \sqrt{\xi} = R_{\text{L}}\, I_{s,0} \sqrt{\frac{1}{\xi}}. \end{aligned} \tag{B.1}$$

Using the above simplifications and assumptions, (5.7) can be approximated as:

$$P_e(e|h) \approx \frac{1}{2} \text{erfc}\left(\frac{R_{\text{L}}\, I_{s,0} \sqrt{\frac{1}{\xi}} - R_{\text{L}}\, I_{s,0}}{\sqrt{2\,\sigma^2_{n_0}}} \right). \tag{B.2}$$

The expression of $P_e(e|h)$ above can further be re-written using the following denotations; $\omega = R_{\text{L}}\, \mathcal{R}_{\text{e}}\, P_{\text{Tx}_0}$, $\alpha = 2\, e\, G\, F\, B_e\, R_{\text{L}}\, \omega$, and $\beta = R^2_{\text{L}}\, \sigma^2_{\text{d}} + R^2_{\text{L}}\, \sigma^2_{\text{b}} + \sigma^2_{\text{th}}$; as:

$$P_e(e|h) = \frac{1}{2} \text{erfc}\left(\frac{\omega\, h \left(\sqrt{\frac{1}{\xi}} - 1 \right)}{\sqrt{2\, \alpha\, h + 2\, \beta}} \right). \tag{B.3}$$

Note, to derive the channel threshold h_{th}, such that $P_e(e|h_{\text{th}}) = \text{BER}_{\text{th}}$, (B.3) can be manipulated to yield h_{th} as:

$$h_{\text{th}} = \frac{\mathcal{B} + \sqrt{\mathcal{B}^2 + 4\mathcal{A}\mathcal{C}}}{2\mathcal{A}}, \tag{B.4}$$

where $\mathcal{A} = \left(\omega\sqrt{\frac{1}{\xi}} - \omega\right)^2$, $\mathcal{B} = \alpha\mathcal{D}^2$, $\mathcal{C} = \beta\mathcal{D}^2$, $\mathcal{D} = Q^{-1}\left(\text{BER}_{\text{th}}\right)$, and Q^{-1} is the inverse Q-function.

Appendix C

C.1 Derivation of the closed form equation for outage probability

Here, we explain our approach for deriving the closed form asymptotic expression for Subsection 6.3.5, Equation (6.29). Using (6.27), (6.9), (6.22), (6.11), and the definition of P_{out} given in (5.10), it can be shown that,

$$\begin{aligned} P_{\text{out}} = {} & \frac{(A_0\, h_c)^{-\frac{w_{Leq}^2}{4\sigma_{r_d}^2}}}{\sqrt{\pi}} \frac{w_{Leq}^2}{4\sigma_{r_d}^2} \int\limits_0^{h_{\text{th}}} h^{\frac{w_{Leq}^2}{4\sigma_{r_d}^2}-1}\, dh \\ & \int\limits_{h/A_0\, h_c}^{\infty} h_t^{-\frac{w_{Leq}^2}{4\sigma_{r_d}^2}-1} \frac{1}{\sqrt{2\sigma_T^2}} \exp\left(-\frac{\left(\ln(h_t)-\mu_T\right)^2}{2\sigma_T^2}\right) dh_t. \end{aligned} \tag{C.1}$$

Considering change of variables in (C.1) as $X = \left(\ln(h_t) - \mu_T\right)/\sqrt{2\sigma_T^2}$ and utilizing [193, Section 2.33, Eq.(1)] then (C.1) can be rewritten as:

$$\begin{aligned} P_{\text{out}} = {} & (A_0\, h_c)^{-\frac{w_{Leq}^2}{4\sigma_{r_d}^2}} \frac{w_{Leq}^2}{8\sigma_{r_d}^2} \exp\left(-\mu_T \frac{w_{Leq}^2}{4\sigma_{r_d}^2}\right) \exp\left(\sigma_T^2 \frac{w_{Leq}^4}{32\,\sigma_{r_d}^4}\right) \\ & \int\limits_0^{h_{\text{th}}} h^{\frac{w_{Leq}^2}{4\sigma_{r_d}^2}-1} \operatorname{erfc}\left(\sqrt{2\sigma_T^2}\frac{w_{Leq}^2}{8\,\sigma_{r_d}^2} + X_l\right) dh, \end{aligned} \tag{C.2}$$

where $X_l = \left(\ln(h) - \ln(A_0\, h_c) - \mu_T\right)/\sqrt{2\sigma_T^2}$.
Now, defining Y as follows,

$$Y = \sqrt{2\sigma_T^2}\frac{w_{Leq}^2}{8\,\sigma_{r_d}^2} + \frac{\left(-\ln(A_0\, h_c) - \mu_T\right)}{\sqrt{2\sigma_T^2}} + \ln(h)\frac{1}{\sqrt{2\sigma_T^2}}, \tag{C.3}$$

then, (C.2) can be expressed as:

$$
\begin{aligned}
P_{\text{out}} = {} & \frac{(A_0\, h_c)^{-\frac{w_{Leq}^2}{4\sigma_{r_d}^2}}}{\sqrt{2\sigma_T^2}} \frac{w_{Leq}^2}{8\sigma_{r_d}^2} \exp\left(-\mu_T \frac{w_{Leq}^2}{4\sigma_{r_d}^2}\right) \exp\left(\sigma_T^2 \frac{w_{Leq}^4}{32\sigma_{r_d}^4}\right) \\
& \exp\left(-\left(\frac{w_{Leq}^2}{8\sigma_{r_d}^2} + \frac{\left(-\ln(A_0\, h_c) - \mu_T\right)}{2\sigma_T^2}\right) \frac{w_{Leq}^2}{4\sigma_{r_d}^2}\right) \\
& \int_{-\infty}^{Y_u} \exp\left(\frac{Y}{\sqrt{2\sigma_T^2}} \frac{w_{Leq}^2}{4\sigma_{r_d}^2}\right) \operatorname{erfc}(Y)\, dY,
\end{aligned}
\tag{C.4}
$$

where

$$
Y_u = \sqrt{2\sigma_T^2} \frac{w_{Leq}^2}{8\sigma_{r_d}^2} + \frac{\left(-\ln(A_0\, h_c) - \mu_T\right)}{\sqrt{2\sigma_T^2}} + \ln(h_{\text{th}}) \frac{1}{\sqrt{2\sigma_T^2}}. \tag{C.5}
$$

The integration in (C.4) can be solved by using [194, Section 4.2, Eq.(2)] and further simplified as:

$$
\begin{aligned}
P_{\text{out}} = {} & \frac{(A_0\, h_c)^{-\frac{w_{Leq}^2}{4\sigma_{r_d}^2}}}{2} \exp\left(-\mu_T \frac{w_{Leq}^2}{4\sigma_{r_d}^2}\right) \exp\left(\sigma_T^2 \frac{w_{Leq}^4}{32\sigma_{r_d}^4}\right) \\
\times & \left[\begin{array}{c}
h_{\text{th}}^{\frac{w_{Leq}^2}{4\sigma_{r_d}^2}} \operatorname{erfc}\left(\frac{2\sigma_T^2\, w_{Leq}^2 + 8\sigma_{r_d}^2 (\ln(h_{\text{th}}) - \ln(A_0\, h_c) - \mu_T)}{8\sigma_{r_d}^2 \sqrt{2\sigma_T^2}}\right) \\
+ \exp\left(\frac{1}{\sigma_T^2} \frac{w_{Leq}^4}{128\sigma_{r_d}^4}\right) \\
\exp\left(-\frac{8\sigma_{r_d}^2 \sigma_T^2\, w_{Leq}^4 - 32\sigma_{r_d}^4\, w_{Leq}^2 (-\ln(A_0\, h_c) - \mu_T)}{256\sigma_{r_d}^6 \sigma_T^2}\right) \\
\operatorname{erfc}\left(\frac{-2\sigma_T^2\, w_{Leq}^2 - 8\sigma_{r_d}^2 (\ln(h_{\text{th}}) - \ln(A_0\, h_c) - \mu_T) + w_{Leq}^2}{8\sigma_{r_d}^2 \sqrt{2\sigma_T^2}}\right)
\end{array}\right].
\end{aligned}
\tag{C.6}
$$

Lastly, for $h_{\text{th}} \to 0$, (C.6) can be simplified as follows.

$$
\begin{aligned}
\lim_{h_{\text{th}} \to 0} P_{\text{out}} = {} & (A_0\, h_c)^{-\frac{w_{Leq}^2}{4\sigma_{r_d}^2}} \exp\left(-\mu_T \frac{w_{Leq}^2}{4\sigma_{r_d}^2}\right) \\
& \exp\left(\sigma_T^2 \frac{w_{Leq}^4}{32\sigma_{r_d}^4}\right) h_{\text{th}}^{\frac{w_{Leq}^2}{4\sigma_{r_d}^2}}.
\end{aligned}
\tag{C.7}
$$

List of Figures

List of Tables

Bibliography

[1] H. Kaushal and G. Kaddoum, “Underwater optical wireless communication,” *IEEE Access*, vol. 4, pp. 1518–1547, 2016.

[2] C. M. Gussen, P. S. Diniz, M. Campos, W. A. Martins, F. M. Costa, and J. N. Gois, “A survey of underwater wireless communication technologies,” *Journal of Communication and Information Systems*, vol. 31, no. 1, pp. 242–255, 2016.

[3] M. A. Khalighi, C. J. Gabriel, L. M. Pessoa, and B. Silva, *Visible Light Communications: Theory and Applications*, chapter Underwater Visible Light Communications, Channel Modeling and System Design, pp. 337–372, CRC-Press, 2017.

[4] G. Schirripa Spagnolo, L. Cozzella, and F. Leccese, “Underwater optical wireless communications: Overview,” *Sensors*, vol. 20, no. 8, pp. 2261, Apr. 2020.

[5] J. Lloret, S. Sendra, M. Ardid, and J. J. Rodrigues, “Underwater wireless sensor communications in the 2.4 GHz ISM frequency band,” *Sensors*, vol. 12, no. 4, pp. 4237–4264, 2012.

[6] A. I. Al-Shamma’a, A. Shaw, and S. Saman, “Propagation of electromagnetic waves at MHz frequencies through seawater,” *IEEE Transactions on Antennas and Propagation*, vol. 52, no. 11, pp. 2843–2849, 2004.

[7] H. Kulhandjian, “Inside out: Underwater communications,” *Journal of Ocean Technology*, vol. 9, no. 2, pp. 104–105, 2014.

[8] R. S. Istepanian and M. Stojanovic, *Underwater acoustic digital signal processing and communication systems*, Springer, 2002.

[9] O. George and R. Bahl, “Simulation of backscattering of high frequency sound from complex objects and sand sea-bottom,” *IEEE Journal of Oceanic Engineering*, vol. 20, no. 2, pp. 119–130, 1995.

[10] M. Stojanovic, “Underwater wireless communications: Current achievements and research challenges,” *IEEE Oceanic Engineering Society Newsletter*, vol. 41, no. 2, pp. 1–5, 2006.

[11] R. E. Williams and H. F. Battestin, "Coherent recombination of acoustic multipath signals propagated in the deep ocean," *Journal of the Acoustical Society of America*, vol. 50, no. 6A, pp. 1433–1442, 1971.

[12] B. S. Sharif, J. Neasham, O. R. Hinton, and A. E. Adams, "A computationally efficient doppler compensation system for underwater acoustic communications," *IEEE Journal of Oceanic Engineering*, vol. 25, no. 1, pp. 52–61, 2000.

[13] B. Li, S. Zhou, M. Stojanovic, L. Freitag, and P. Willett, "Multicarrier communication over underwater acoustic channels with nonuniform doppler shifts," *IEEE Journal of Oceanic Engineering*, vol. 33, no. 2, pp. 198–209, 2008.

[14] Z. Ghassemlooy, S. Zvanovec, M.-A. Khalighi, W. O. Popoola, and J. Perez, "Optical wireless communication systems," *Optik*, vol. 151, pp. 1–6, 2017.

[15] M. A. Khalighi, Z. Ghassemlooy, M.-S. Alouini, S. Hranilovic, and S. Zvanovec, "Special issue on: Optical wireless communications for emerging connectivity requirements," *IEEE Open Journal of the Communications Society*, vol. 2, pp. 82–86, 2021.

[16] Z. Ghassemlooy, M. Uysal, M. A. Khalighi, V. Ribeiro, F. Moll, S. Zvanovec, and A. Belmonte, "An overview of optical wireless communications," *Optical Wireless Communications*, pp. 1–23, 2016.

[17] M. A. Khalighi, C. Gabriel, T. Hamza, S. Bourennane, P. Léon, and V. Rigaud, "Underwater wireless optical communication; recent advances and remaining challenges," in *2014 16th International Conference on Transparent Optical Networks (ICTON)*. IEEE, 2014, pp. 1–4.

[18] C. Gabriel, M. A. Khalighi, S. Bourennane, P. Léon, and V. Rigaud, "Misalignment considerations on point-to-point underwater wireless optical links," *IEEE OCEANS Conference*, June 2013, Bergen, Norway.

[19] T. Hamza, M. A. Khalighi, S. Bourennane, P. Léon, and J. Opderbecke, "Investigation of solar noise impact on the performance of underwater wireless optical communication links," *Optics Express*, vol. 24, no. 22, pp. 25832–25845, Oct. 2016.

[20] M. Elamassie and M. Uysal, "Vertical underwater visible light communication links: Channel modeling and performance analysis," *IEEE Transactions on Communications*, vol. 19, no. 10, pp. 6948–6959, 2020.

[21] *MC100 Underwater Optical Wireless Communication Modem*, 2020, https://www.shimadzu.com/news/g16mjizzgbhz3–y.html.

[22] *Luma X, High speed, long range wireless optical modem*, Hydromea, https://www.hydromea.com/underwater-wireless-communication/.

[23] *BlueComm 200, Underwater optical communications and data transfer modem,* Sonardyne, https://www.sonardyne.com/products/bluecomm-200-wireless-underwater-link/.

[24] *Underwater optical networks technologies,* http://www.uontechnologies.com/about.php.

[25] M. Doniec, C. Detweiler, I. Vasilescu, M. Chitre, M. Hoffmann-Kuhnt, and D. Rus, "Aquaoptical: A lightweight device for high-rate long-range underwater point-to-point communication," *Marine Technology Society Journal*, vol. 44, no. 4, pp. 55–65, 2010.

[26] M. Doniec and D. Rus, "Bidirectional optical communication with [aquaoptical ii," in *2010 IEEE International Conference on Communication Systems.*

[27] P. Léon, F. Roland, L. Brignone, J. Opderbecke, J. Greer, M. A. Khalighi, T. Hamza, S. Bourennane, and M. Bigand, "A new underwater optical modem based on highly sensitive silicon photo-multipliers," *IEEE OCEANS Conference*, June 2017, Aberdeen, UK.

[28] B. Shihada, O. Amin, C. Bainbridge, S. Jardak, O. Alkhazragi, T. K. Ng, B. Ooi, M. Berumen, and M.-S. Alouini, "Aqua-fi: Delivering internet underwater using wireless optical networks," *IEEE Communications Magazine*, vol. 58, no. 5, pp. 84–89, 2020.

[29] T. Essalih, *High Spectral-Efficiency Signaling Schemes for Underwater Wireless Optical Communication Systems,* Ph.D. thesis, École Centrale Marseille, Mar. 2021.

[30] T. Jiang, D. Chen, C. Ni, and D. Qu, *OQAM/FBMC for future wireless communications: Principles, technologies and applications,* Academic Press, 2017.

[31] Z. Ghassemlooy, W. Popoola, and S. Rajbhandari, *Optical Wireless Communications: System and Channel Modelling with* MATLAB, CRC Press, Boca Raton, FL, 1st edition, 2013.

[32] T. Cseh, S. Rajbhandari, G. Fekete, and E. Udvary, *Visible Light Communications: Theory and Applications,* chapter Modulation Schemes, pp. 97–144, CRC-Press, 2017.

[33] S. Long, *Indoor Channel Modeling and High Data-Rate Transmission for Visible Light Communication Systems,* Ph.D. thesis, École Centrale Marseille, Sept. 2016.

[34] T. Hamza, *Underwater Wireless Optical Communications: Long-range High-data-rate Transmission and Performance Analysis,* Ph.D. thesis, École Centrale Marseille, Mar. 2017.

[35] C. Gabriel, *Channel Characterization and Performance Analysis for an Underwater Optical Transmission System,* Ph.D. thesis, Aix-Marseille University, May 2013.

[36] M. A. Khalighi, T. Hamza, S. Bourennane, P. Léon, and J. Opderbecke, "Underwater wireless optical communications using silicon photo-multipliers," *IEEE Photonics Journal*, vol. 9, no. 4, 2017, DOI 10.1109/JPHOT.2017.2726565.

[37] J. Shen, J. Wang, C. Yu, X. Chen, J. Wu, M. Zhao, F. Qu, Z. Xu, J. Han, and J. Xu, "Single LED-based 46-m underwater wireless optical communication enabled by a multi-pixel photon counter with digital output," *Optics Communications*, vol. 438, pp. 78–82, 2019.

[38] W. Wei, C. Zhang, W. Zhang, W. Jiang, C. Shu, and Q. Xiaorui, "LED-based underwater wireless optical communication for small mobile platforms: Experimental channel study in highly-turbid lake water," *IEEE Access*, vol. 8, pp. 169304–169313, 2020.

[39] I. C. Ijeh, M. A. Khalighi, and S. Hranilovic, "Parameter optimization for an underwater optical wireless vertical link subject to link misalignments," *IEEE Journal of Oceanic Engineering*, 2021, Early Access.

[40] C. T. Geldard, J. Thompson, and W. O. Popoola, "Empirical study of the underwater turbulence effect on non-coherent light," *IEEE Photonics Technology Letters*, vol. 32, no. 20, pp. 1307–1310, 2020.

[41] F. Zafar, M. Bakaul, and R. Parthiban, "Laser-diode-based visible light communication: Toward gigabit class communication," *IEEE Communications Magazine*, vol. 55, no. 2, pp. 144–151, 2017.

[42] X. Liu, S. Yi, X. Zhou, Z. Fang, Z.-J. Qiu, L. Hu, C. Cong, L. Zheng, R. Liu, and P. Tian, "34.5 m underwater optical wireless communication with 2.70 Gbps data rate based on a green laser diode with NRZ-OOK modulation," *Optical Express*, vol. 25, no. 22, pp. 27937–27947, Oct 2017.

[43] J. Wang, C. Lu, S. Li, and Z. Xu, "100 m/500 Mbps underwater optical wireless communication using an NRZ-OOK modulated 520 nm laser diode," *Optical Express*, vol. 27, no. 9, pp. 12171–12181, Apr 2019.

[44] A. Al-Halafi, H. M. Oubei, B. S. Ooi, and B. Shihada, "Real-time video transmission over different underwater wireless optical channels using a directly modulated 520 nm laser diode," *IEEE/OSA Journal of Optical Communications and Networking*, vol. 9, no. 10, pp. 826–832, 2017.

[45] A. Al-Halafi and B. Shihada, "UHD video transmission over bidirectional underwater wireless optical communication," *IEEE Photonics Journal*, vol. 10, no. 2, pp. 1–14, 2018.

[46] F. Xu, M. A. Khalighi, and S. Bourennane, "Impact of different noise sources on the performance of PIN- and APD-based FSO receivers," in *Proceedings of the 11th International Conference on Telecommunications*, 2011, pp. 211–218.

[47] J. Wang, C. Tian, X. Yang, W. Shi, Q. Niu, and T. A. Gulliver, "Underwater wireless optical communication system using a 16-QAM modulated 450-nm laser diode based on an FPGA," *Applied Optics*, vol. 58, no. 16, pp. 4553–4559, Jun 2019.

[48] T. C. Wu, Y. C. Chi, H.-Y. Wang, C. T. Tsai, and G. R. Lin, “Blue laser diode enables underwater communication at 12.4 Gbps,” *Scientific reports*, vol. 7, no. 1, pp. 1–10, 2017.

[49] D. Chen, C. Li, and Z. Xu, “Performance evaluation of OOK and PAM modulations in underwater optical wireless communication system based on APD receiver,” in *2017 16th International Conference on Optical Communications and Networks (ICOCN)*, 2017, pp. 1–3.

[50] M. P. A. Das, P. Arjun, A. S. Bhaskaran, P. S. Aravind, T. R. Aswin, and V. Sadasivan, “Estimation of maximum range for underwater optical communication using PIN and avalanche photodetectors,” in *2019 International Conference on Advances in Computing and Communication Engineering (ICACCE)*, 2019, pp. 1–6.

[51] M. A. A. Ali, “Comparison of modulation techniques for underwater optical wireless communication employing APD receivers,” *Research Journal of Applied Sciences, Engineering and Technology*, vol. 10, no. 6, pp. 707–715, 2015.

[52] P. Wang, C. Li, B. Wang, and Z. Xu, “Real-time 25Mb/s data transmission for underwater optical wireless communication using a commercial blue LED and APD detection,” in *2016 Asia Communications and Photonics Conference (ACP)*, 2016, pp. 1–3.

[53] J. Li, B. Yang, D. Ye, L. Wang, K. Fu, J. Piao, and Y. Wang, “A real-time, full-duplex system for underwater wireless optical communication: Hardware structure and optical link model,” *IEEE Access*, vol. 8, pp. 109372–109387, 2020.

[54] P. Lacovara, “High-bandwidth underwater communications,” *Marine Technology Society Journal*, vol. 42, no. 1, pp. 93–102, 2008.

[55] T. Hakamata, *Photomultiplier Tube-Basics and Applications*, Hamamatsu Photonics K.K., Shizuoka, 3rd edition, 2007.

[56] J. Ning, G. Gao, J. Zhang, H. Peng, and Y. Guo, “Adaptive receiver control for reliable high-speed underwater wireless optical communication with photomultiplier tube receiver,” *IEEE Photonics Journal*, vol. 13, no. 4, pp. 1–7, 2021.

[57] T. Liu, H. Zhang, Y. Zhang, and J. Song, “Experimental demonstration of LED based underwater wireless optical communication,” in *2017 4th International Conference on Information Science and Control Engineering (ICISCE)*, 2017, pp. 1501–1504.

[58] K. Nakamura, K. Nagaoka, D. Matsuo, T. Kodama, and M. Hanawa, “Over 1 Gbit/s NRZ-OOK underwater wireless optical transmission experiment using wideband PMT,” in *2019 24th OptoElectronics and Communications Conference (OECC) and 2019 International Conference on Photonics in Switching and Computing (PSC)*, 2019, pp. 1–3.

[59] T. Hamza, M. A. Khalighi, S. Bourennane, P. Léon, and J. Opderbecke, “On the suitability of employing silicon photomultipliers for underwater wireless optical communication links,”

in *2016 10th International Symposium on Communication Systems, Networks and Digital Signal Processing (CSNDSP)*, 2016, pp. 1–5.

[60] T. Hamza and M. A. Khalighi, "On limitations of using silicon photo-multipliers for underwater wireless optical communications," in *2019 2nd West Asian Colloquium on Optical Wireless Communications (WACOWC)*, 2019, pp. 74–79.

[61] T. Essalih, M. A. Khalighi, S. Hranilovic, and H. Akhouayri, "Optical OFDM for SiPM-based underwater optical wireless communication links," *MDPI Sensors, Special Issue on Visible Light Communication, Networking, and Sensing*, vol. 20, no. 6057, pp. 1–28, Oct. 2020, Invited Paper.

[62] M. A. Khalighi, H. Akhouayri, and S. Hranilovic, "SiPM-based underwater wireless optical communication using pulse-amplitude modulation," *IEEE Journal of Oceanic Engineering*, vol. 45, no. 4, pp. 1611–1621, Oct. 2020.

[63] Z. Chen, X. Tang, C. Sun, Z. Li, W Shi, H. Wang, L. Zhang, and A. Zhang, "Experimental demonstration of over 14 AL underwater wireless optical communication," *IEEE Photonics Technology Letters*, vol. 33, no. 4, pp. 173–176, 2021.

[64] L. Zhang, X. Tang, C. Sun, Z. Chen, Z. Li, H. Wang, R. Jiang, W. Shi, and A. Zhang, "Over 10 attenuation length gigabits per second underwater wireless optical communication using a silicon photomultiplier (SiPM) based receiver," *OpticS Express*, vol. 28, no. 17, pp. 24968–24980, Aug 2020.

[65] J. Shen, J. Wang, X. Chen, C. Zhang, M. Kong, Z. Tong, and J. Xu, "Towards power-efficient long-reach underwater wireless optical communication using a multi-pixel photon counter," *Optics express*, vol. 26, no. 18, pp. 23565–23571, 2018.

[66] C. Gabriel, M. A. Khalighi, S. Bourennane, P. Léon, and V. Rigaud, "Monte-Carlo-based channel characterization for underwater optical communication systems," *IEEE/OSA Journal of Optical Communications and Networking*, vol. 5, no. 1, pp. 1–12, 2013.

[67] S. Jaruwatanadilok, "Underwater wireless optical communication channel modeling and performance evaluation using vector radiative transfer theory," *IEEE Journal on Selected Areas in Communications*, vol. 26, no. 9, pp. 1620–1627, 2008.

[68] B. Cochenour, L. Mullen, and J. Muth, "Temporal response of the underwater optical channel for high-bandwidth wireless laser communications," *IEEE Journal of Oceanic Engineering*, vol. 38, no. 4, pp. 730–742, 2013.

[69] M. Bernotas and C. Nelson, "Probability density function analysis for optimization of underwater optical communications systems," in *OCEANS 2015 - MTS/IEEE Washington*, 2015, pp. 1–8.

[70] M. V. Jamali, A. Mirani, A. Parsay, B. Abolhassani, P. Nabavi, A. Chizari, P. Khorramshahi, S. Abdollahramezani, and J. A. Salehi, "Statistical studies of fading in underwater wireless optical channels in the presence of air bubble, temperature, and salinity random variations," *IEEE Transactions on Communications*, vol. 66, no. 10, pp. 4706–4723, 2018.

[71] Y. Fu, C. Huang, and Y. Du, "Effect of aperture averaging on mean bit error rate for UWOC system over moderate to strong oceanic turbulence," *Optics Communications*, vol. 451, pp. 6–12, 2019.

[72] Y. Baykal, "Adaptive optics correction of scintillation in underwater medium," *Journal of Modern Optics*, vol. 67, no. 3, pp. 220–225, 2020.

[73] W. Liu, Z. Xu, and L. Yang, "SIMO detection schemes for underwater optical wireless communication under turbulence," *Photonics Research*, vol. 3, no. 3, pp. 48–53, Jun 2015.

[74] S. Tang, Y. Dong, and X. Zhang, "On link misalignment for underwater wireless optical communications," *IEEE Communications Letters*, vol. 16, no. 10, pp. 1688–1690, 2012.

[75] J. A. Simpson, B. L. Hughes, and J. F. Muth, "Smart transmitters and receivers for underwater free-space optical communication," *IEEE Journal on Selected Areas in Communications*, vol. 30, no. 5, pp. 964–974, 2012.

[76] Z. Vali, A. Gholami, D. G. Michelson, Z. Ghassemlooy, M. Omoomi, and H. Noori, "Use of Gaussian beam divergence to compensate for misalignment of underwater wireless optical communication links," *IET Optoelectronics*, vol. 11, no. 5, pp. 171–175, 2017.

[77] J. Sticklus, M. Hieronymi, and P. A. Hoeher, "Effects and constraints of optical filtering on ambient light suppression in LED-based underwater communications," *Sensors*, vol. 18, no. 11, 2018.

[78] R. Stokes, M. Bermal, C. Griffith, R. Blair, E. J. Marttila, and G. Mooradian, "An adaptive data rate controller (ADRC) for the through cloud, undersea laser communications channel," in *2012 IEEE Photonics Society Summer Topical Meeting Series*, 2012, pp. 107–108.

[79] F. Miramirkhani and M. Uysal, "Visible light communication channel modeling for underwater environments with blocking and shadowing," *IEEE Access*, vol. 6, pp. 1082–1090, 2018.

[80] P. Kwatra, "ARQ protocol studies in underwater communication networks," in *2013 INTERNATIONAL CONFERENCE ON SIGNAL PROCESSING AND COMMUNICATION (ICSC)*, 2013, pp. 121–126.

[81] A. Babiker and N. Zakaria, "Energy efficient communication for underwater wireless sensors networks," *Energy Efficiency in Communications and Networks*, vol. 47, 2012.

[82] Y. Zhao, A Wang, L. Zhu, W. Lv, J. Xu, S. Li, and J. Wang, "Performance evaluation of underwater optical communications using spatial modes subjected to bubbles and obstructions," *Optics Letters*, vol. 42, no. 22, pp. 4699–4702, Nov 2017.

[83] X. Tang, L. Zhang, C. Sun, Z. Chen, H. Wang, R. Jiang, Z. Li, W. Shi, and A. Zhang, “Underwater wireless optical communication based on DPSK modulation and silicon photomultiplier,” *IEEE Access*, vol. 8, pp. 204676–204683, 2020.

[84] J. Wang, X. Yang, W. Lv, C. Yu, J. Wu, M. Zhao, F. Qu, Z. Xu, J. Han, and J. Xu, “Underwater wireless optical communication based on multi-pixel photon counter and OFDM modulation,” *Optics Communications*, vol. 451, pp. 181–185, 2019.

[85] J. F. C. Carreira, G. N. Arvanitakis, A. D. Griffiths, J. J. D. McKendry, E. Xie, J. Kosman, R. K. Henderson, E. Gu, and M. D. Dawson, “Underwater wireless optical communications at 100 Mb/s using integrated dual-color micro-LEDs,” in *2019 IEEE Photonics Conference (IPC)*, 2019, pp. 1–2.

[86] M. Zhao, X. Li, X. Chen, Z. Tong, W. Lyu, Z. Zhang, and J. Xu, “Long-reach underwater wireless optical communication with relaxed link alignment enabled by optical combination and arrayed sensitive receivers,” *Optics express*, vol. 28, no. 23, pp. 34450–34460, 2020.

[87] A. Ghassemi, K. Sato, and K. Kobayashi, “MPPC,” 2017, available at `https://www.hamamatsu.com/resources/pdf/ssd/mppc_kapd9005e.pdf`.

[88] *Introduction to SiPM, Technical Note*, ON Semiconductor® - SensL, 2011 (Rev. 6.0, Feb. 2017), available at `https://www.sensl.com/downloads/ds/TN%20-%20Intro%20to%20SPM%20Tech.pdf`.

[89] D. Renker and E. Lorenz, “Advances in solid state photon detectors,” *Journal of Instrumentation*, vol. 4, no. 04, pp. P04004, 2009.

[90] F. Castro, *Silicon Photomultipliers*, 2015, available at `https://www.researchgate.net/publication/275039208$_$Silicon$_$Photomultipliers`.

[91] Y. Li, M. Safari, R. Henderson, and H. Haas, “Nonlinear distortion in SPAD-based optical OFDM systems,” in *2015 IEEE Globecom Workshops (GC Wkshps)*, 2015, pp. 1–6.

[92] Y. Li, S. Videv, M. Abdallah, K. Qaraqe, M. Uysal, and H. Haas, “Single photon avalanche diode (SPAD) VLC system and application to downhole monitoring,” in *2014 IEEE Global Communications Conference*, 2014, pp. 2108–2113.

[93] N. Otte, “The silicon photomultiplier-a new device for high energy physics, astroparticle physics, industrial and medical applications,” in *Proceedings of the IX International Symposium on Detectors for Particle, Astroparticle and Synchrotron Radiation Experiments*, 2006, pp. 1–9.

[94] A. Para, “Afterpulsing in silicon photomultipliers: Impact on the photodetectors characterization,” *arXiv preprint arXiv:1503.01525*, 2015.

[95] *ID 150 VIS 8 channel SPAD: Miniature 8-channel photon counter for OEM applications*, ID Quantique, 2010, http://www.idquantique.com.

[96] *B-Series Fast, Blue-Sensitive Silicon Photomultiplier Sensors datasheet*, SensL, 2013, http://www.sensl.com/downloads/ds/DS-MicroBseries.pdf.

[97] J. M. Kahn and J. R. Barry, "Wireless infrared communications," *Proceedings of the IEEE*, vol. 85, no. 2, pp. 265–298, Feb 1997.

[98] *LUXEON Rebel Color Line datasheet DS68 20171106*, LUMILEDS, 2017, available at `https://www.lumileds.com/uploads/265/DS68-pdf`.

[99] J. W. Giles and I. N. Bankman, "Underwater optical communication systems. Part 2 : Basic design considerations," *Military Communications Conference (MILCOM)*, vol. 3, pp. 1700–1705, Oct. 2005, Atlantic City, NJ, USA.

[100] T. Komine and M. Nakagawa, "Fundamental analysis for visible-light communication system using LED lights," *IEEE Transactions on Consumer Electronics*, vol. 50, no. 1, pp. 100–107, Feb 2004.

[101] J. R. Barry, J. M. Kahn, W. J. Krause, E. A. Lee, and D. G. Messerschmitt, "Simulation of multipath impulse response for indoor wireless optical channels," *IEEE Journal on Selected Areas in Communications*, vol. 11, no. 3, pp. 367–379, April 1993.

[102] "ITU-T recommendation g.975.1," (02/2004).

[103] N. Kaur, P. Singh, and P. Kaur, "Under water environment: A brief of explored work and future scope," *IJCA International Conference on Advances in Emerging Technology*, , no. 2, pp. 12–17, Sept. 2016.

[104] S. Arnon, "Underwater optical wireless communication network," *Optical Engineering*, vol. 49, no. 1, pp. 1–6, Jan. 2010.

[105] B. M. Cochenour, L. J. Mullen, and A. E. Laux, "Characterization of the beam-spread function for underwater wireless optical communications links," *IEEE Journal of Oceanic Engineering*, vol. 33, no. 4, pp. 513–521, Oct. 2008.

[106] M. Doniec, M. Angermann, and D. Rus, "An end-to-end signal strength model for underwater optical communications," *IEEE Journal of Oceanic Engineering*, vol. 38, no. 4, pp. 743–757, 2013.

[107] Y. Ata and Y. Baykal, "Structure functions for optical wave propagation in underwater medium," *Waves in Random and Complex Media*, vol. 24, no. 2, pp. 164–173, Feb. 2014.

[108] Y. Baykal, "Scintillations of LED sources in oceanic turbulence," *Applied Optics*, vol. 55, no. 31, pp. 8860–8863, Nov. 2016.

[109] E. Zedini, H. M. Oubei, A. Kammoun, M. Hamdi, B. S. Ooi, and M. S. Alouini, "Unified statistical channel model for turbulence-induced fading in underwater wireless optical communication systems," *IEEE Transcations on Communications*, vol. 67, no. 4, pp. 2893–2907, Apr. 2019.

[110] R. A. Khalil, M. I. Babar, N. Saeed, T. Jan, and H. S. Cho, "Effect of link misalignment in the optical-internet of underwater things," *MDPI Electronics*, vol. 9, no. 4, pp. 646, Apr. 2020.

[111] Y. Dong, S. Tang, and X. Zhang, "Effect of random sea surface on downlink underwater wireless optical communications," *IEEE Communications Letters*, vol. 17, no. 11, pp. 2164–2167, Nov. 2013.

[112] H. Zhang, Y. Dong, and L. Hui, "On capacity of downlink underwater wireless optical MIMO systems with random sea surface," *IEEE Communications Letters*, vol. 19, no. 12, pp. 2166–2169, Dec 2015.

[113] A. S. Ghazy, S. Hranilovic, and M. A. Khalighi, "Angular MIMO for underwater wireless optical communications: Link modeling and tracking," *IEEE Journal of Oceanic Engineering*, pp. 1–17, 2021.

[114] A. A Farid and S. Hranilovic, "Outage capacity optimization for free-space optical links with pointing errors," *Journal of Lightwave Technology*, vol. 25, no. 7, pp. 1702–1710, 2007.

[115] M. A. Khalighi and M. Uysal, "Survey on Free Space Optical Communication: A Communication Theory Perspective," *IEEE Communications Surveys & Tutorials*, vol. 16, no. 4, pp. 2231–2258, Nov. 2014.

[116] D. K. Borah and D. G. Voelz, "Pointing error effects on free-space optical communication links in the presence of atmospheric turbulence," *Journal of Lightwave Technology*, vol. 27, no. 18, pp. 3965–3973, 2009.

[117] F. Yang, J. Cheng, and T. A. Tsiftsis, "Free-space optical communication with nonzero boresight pointing errors," *IEEE Transactions on Communications*, vol. 62, no. 2, pp. 713–725, 2014.

[118] W. H. Wells, "Theory of small angle scattering," in *Optics of the Sea*, vol. 61. NATO, 1973.

[119] S. Arnon and D. Kedar, "Non-line-of-sight underwater optical wireless communication network," *Journal of the Optical Society of America A*, vol. 26, no. 3, pp. 530–539, Mar. 2009.

[120] C. Cox and W. Munk, "Measurement of the roughness of the sea surface from photographs of the sun's glitter," *Journal of the Optical Society of America*, vol. 44, no. 11, pp. 838–850, Nov. 1954.

[121] R. Boluda-Ruiz, A. García-Zambrana, B. Castillo-Vázquez, and S. Hranilovic, "Impact of angular pointing error on BER performance of underwater optical wireless links," *Optics Express*, vol. 28, no. 23, pp. 34606–34622, Nov 2020.

[122] Y. Li, Y. Zhang, and Y. Zhu, "Capacity of underwater wireless optical links with pointing errors," *Optics Communications*, vol. 446, pp. 16–22, 2019.

[123] J. Liu, Y. Dong, and H. Zhang, "On received intensity for misaligned underwater wireless optical links," *IEEE OCEANS Conference*, Apr. 2016, Shanghai, China.

[124] C. M. Swenson, C. A. Steed, A. Imelda, and R. Q. Fugate, "Low-power FLC-based retromodulator communications system," in *Free-Space Laser Communication Technologies IX*. International Society for Optics and Photonics, 1997, vol. 2990, pp. 296–310.

[125] W. C. Cox, K. F. Gray, J. A. Simpson, B. Cochenour, B. L. Hughes, and J. F. Muth, "A MEMS blue/green retroreflecting modulator for underwater optical communications," in *OCEANS 2010 MTS/IEEE SEATTLE*. IEEE, 2010, pp. 1–4.

[126] W. S. Rabinovich, R. Mahon, P. G. Goetz, E. Waluschka, D. S. Katzer, S. C. Binari, and G. C. Gilbreath, "A cat's eye multiple quantum-well modulating retro-reflector," *IEEE Photonics Technology Letters*, vol. 15, no. 3, pp. 461–463, 2003.

[127] B. Cochenour and L. Mullen, "Channel response measurements for diffuse non-line-of-sight (NLOS) optical communication links underwater," in *OCEANS'11 MTS/IEEE KONA*. IEEE, 2011, pp. 1–5.

[128] A. E. A. El-Fikky, M. E. Eldin, H. A. Fayed, A. Abd El Aziz, H. M. H. Shalaby, and M. H. Aly, "NLoS underwater VLC system performance: static and dynamic channel modeling," *Applied optics*, vol. 58, no. 30, pp. 8272–8281, 2019.

[129] A. S. Ghazy, S. Hranilovic, and M. A. Khalighi, "Angular MIMO for underwater wireless optical communications: Channel modelling and capacity," *IEEE Canadian Workshop on Information Theory (CWIT)*, pp. 1–6, June 2019, Hamilton, ON, Canada.

[130] L. J. Johnson, R. J. Green, and M. S. Leeson, "Underwater optical wireless communications: depth-dependent beam refraction," *Applied optics*, vol. 53, no. 31, pp. 7273–7277, 2014.

[131] X. Sun, C. H. Kang, M. Kong, O. Alkhazragi, Y. Guo, M. Ouhssain, Y. Weng, B. H. Jones, T. K. Ng, and B. S. Ooi, "A review on practical considerations and solutions in underwater wireless optical communication," *Journal of Lightwave Technology*, vol. 38, no. 2, pp. 421–431, Jan. 2020.

[132] Z. Lv, G. He, C. Qiu, and Z. Liu, "Investigation of underwater wireless optical communications links with surface currents and tides for oceanic signal transmission," *IEEE Photonics Journal*, vol. 13, no. 3, pp. 1–8, 2021.

[133] Y. Baykal, "Signal-to-noise ratio reduction due to oceanic turbulence in oceanic wireless optical communication links," *Optics Communications*, vol. 427, pp. 44–47, 2018.

[134] G. Kullenberg, *Pollutant Transfer and Transport in the Sea: Volume II*, CRC-Press, 2018.

[135] Y. Lou, J. Cheng, D. Nie, and G. Qiao, "Performance of underwater wireless optical communications in presents of cascaded mixture exponential-generalized gamma turbulence," *arXiv preprint arXiv:2008.02868*, 2020.

[136] M. C. Gökçe and Y. Baykal, "Aperture averaging and BER for Gaussian beam in underwater oceanic turbulence," *Optics Communications*, vol. 410, pp. 830–835, 2018.

[137] I. Toselli and S. Gladysz, "Improving system performance by using adaptive optics and aperture averaging for laser communications in oceanic turbulence," *Optics Express*, vol. 28, no. 12, pp. 17347–17361, 2020.

[138] Z. Vali, A. Gholami, Z. Ghassemlooy, and D. G. Michelson, "System parameters effect on the turbulent underwater optical wireless communications link," *Optik*, vol. 198, pp. 163153, 2019.

[139] I. Sahnoun, I. S. Ansari, M. Abdallah, and K. Qaraqe, "Performance analysis of adaptive modulation in underwater visible light communications," in *2017 25th International Conference on Software, Telecommunications and Computer Networks (SoftCOM)*, 2017, pp. 1–6.

[140] Z. Wang, Y. Dong, X. Zhang, and S. Tang, "Adaptive modulation schemes for underwater wireless optical communication systems," in *Proceedings of the Seventh ACM International Conference on Underwater Networks and Systems*. 2012, pp. 1–2, Association for Computing Machinery.

[141] J. Nie, L. Tian, H. Wang, L. Chen, Z. Li, S. Yue, Z. Zhang, and H. Yang, "Adaptive beam shaping for enhanced underwater wireless optical communication," *Optics Express*, vol. 29, no. 17, pp. 26404–26417, 2021.

[142] M. Elamassie and M. Uysal, "Feedback-free adaptive modulation selection algorithm for FSO systems," *IEEE Wireless Communications Letters*, vol. 10, no. 9, pp. 1964–1968, 2021.

[143] F. Mattoussi, M. A. Khalighi, and S. Bourennane, "Improving the performance of underwater wireless optical communication links by channel coding," *Applied Optics*, vol. 57, no. 9, pp. 2115–2120, Mar 2018.

[144] C. Gabriel, M. A. Khalighi, S. Bourennane, P. Léon, and V. Rigaud, "Investigation of suitable modulation techniques for underwater wireless optical communication," in *2012 International Workshop on Optical Wireless Communications (IWOW)*, 2012, pp. 1–3.

[145] F. Xu, M. A. Khalighi, and S. Bourennane, "Impact of different noise sources on the performance of PIN- and APD-based FSO receivers," *COST IC0802 Workshop, IEEE ConTEL Conference*, pp. 211–218, June 2011, Graz, Austria.

[146] F. Xu, M. A. Khalighi, P. Caussé, and S. Bourennane, "Channel coding and time-diversity for optical wireless links," *Optics Express*, vol. 17, no. 2, pp. 872–887, Jan. 2009.

[147] M. T. Dabiri, S. M. S. Sadough, and M. A. Khalighi, "FSO channel estimation for OOK modulation with APD receiver over atmospheric turbulence and pointing errors," *Optics Communications*, vol. 402, pp. 577–584, 2017.

[148] M. T. Dabiri, S. M. S. Sadough, and M. A. Khalighi, "Channel modeling and parameter optimization for hovering UAV-based free-space optical links," *IEEE Journal on Selected Areas in Communications*, vol. 36, no. 9, pp. 2104–2113, Sep. 2018.

[149] *Inverse Q function - MATLAB qfuncinv*, The MathWorks, Inc., 2020 (Ver. 9.8.0.1396136 (R2020a)), available at `https://www.mathworks.com/help/comm/ref/qfuncinv.html`.

[150] T. Elfouhaily, B. Chapron, K. Katsaros, and D. Vandemark, "A unified directional spectrum for long and short wind-driven waves," *Journal of Geophysical Research*, vol. 102, no. C7, pp. 781–796, July 1997.

[151] M. D. Soltani, A. A. Purwita, Z. Zeng, H. Haas, and M. Safari, "Modeling the random orientation of mobile devices: Measurement, analysis and LiFi use case," *IEEE Transactions on Communications*, vol. 67, no. 3, pp. 2157–2172, March 2019.

[152] J. N. Monks, L. Yue, B. Yan, B. Aldred, A. Hurst, and Z. Wang, "A wide-angle shift-free metamaterial filter design for anti-laser striking application," *Optics Communications*, vol. 429, pp. 53–59, 2018.

[153] A. A. Purwita, M. D. Soltani, M. Safari, and H. Haas, "Impact of terminal orientation on performance in LiFi systems," in *IEEE Wireless Communications and Networking Conference (WCNC)*, 2018, pp. 1–6.

[154] Y. S. Eroğlu, Y. Yapıcı, and İ. Güvenç, "Impact of random receiver orientation on visible light communications channel," *IEEE Transactions on Communications*, vol. 67, no. 2, pp. 1313–1325, Feb 2019.

[155] C. D. Mobley, *Light and Water: Radiative Transfer in Natural Waters*, Academic Press, 1994.

[156] S. Q. Duntley, "Light in the sea," *Journal of the Optical Society of America*, vol. 53, no. 2, pp. 214–233, Feb 1963.

[157] S. Huang, S. M. Patanwala, J. Kosman, R. K. Henderson, and M. Safari, "Optimal photon counting receiver for sub-dead-time signal transmission," *Journal of Lightwave Technology*, vol. 38, no. 18, pp. 5225–5235, Sept. 2020.

[158] *Numerical integration - MATLAB integral*, The MathWorks, Inc., 2020 (Ver. 9.8.0.1396136(R2020a)), available at `https://www.mathworks.com/help/matlab/ref/integral.html`.

[159] *Subsonus USBL/INS Datasheet*, Advanced Navigation, 2019 (Ver. 3.0), available at `https://www.advancednavigation.com/sites/default/files/product\_documents/Subsonus_Datasheet_0.pdf`.

[160] *Subsonus TAG Transponder Datasheet,* Advanced Navigation, 2019 (Ver. 3.0), available at `https://www.advancednavigation.com/sites/default/files/product\_documents/Subsonus_Tag_Datasheet_0.pdf`.

[161] S. Li, L. Yang, D. B. da Costa, J. Zhang, and M. S. Alouini, "Performance analysis of mixed RF-UWOC dual-hop transmission systems," *IEEE Transactions on Vehicular Technology*, vol. 69, no. 11, pp. 14043–14048, 2020.

[162] F. Xu, M. A. Khalighi, and S. Bourennane, "Impact of different noise sources on the performance of PIN- and APD-based FSO receivers," *COST IC0802 Workshop, IEEE ConTEL Conference*, pp. 211–218, June 2011, Graz, Austria.

[163] Global Ocean Data Assimilation Experiment (GODAE), ," `https://nrlgodae1.nrlmry.navy.mil/index.html`.

[164] Z. Vali, A. Gholami, Z. Ghassemlooy, M. Omoomi, and D. G. Michelson, "Experimental study of the turbulence effect on underwater optical wireless communications," *Applied Optics*, vol. 57, no. 28, pp. 8314–8319, Oct 2018.

[165] L. C. Andrews, R. L Phillips, and C. Y Hopen, *Laser beam scintillation with applications*, vol. 99, SPIE press, 2001.

[166] M. A. Khalighi, N. Schwartz, N. Aitamer, and S. Bourennane, "Fading reduction by aperture averaging and spatial diversity in optical wireless systems," *IEEE/OSA Journal of Optical Communications and Networking*, vol. 1, no. 6, pp. 580–593, 2009.

[167] L. C. Andrews and R. L. Phillips, *Laser beam propagation through random media*, 2005.

[168] B. E. A. Saleh and M. C. Teich, *Fundamentals of Photonics*, New York: Wiley, 1991.

[169] M. T. Dabiri, M. Rezaee, I. S. Ansari, and V. Yazdanian, "Channel modeling for UAV-based optical wireless links with nonzero boresight pointing errors," *IEEE Transactions on Vehicular Technology*, vol. 69, no. 12, pp. 14238–14246, 2020.

[170] R. Chester and T. D. Jickells, *Descriptive Oceanography: Water-Column Parameters*, chapter 7, pp. 125–153, John Wiley and Sons, Ltd, 2012.

[171] R. X. Huang, *Ocean circulation: wind-driven and thermohaline processes*, Cambridge University Press, 2010.

[172] C. Mobley, E. Boss, and C. Roesler, *Ocean Optics Web Book*, 2016.

[173] *MPPC Module Datasheet*, Hamamatsu, 2020, available at `https://www.hamamatsu.com/resources/pdf/ssd/c13366-1350ga$_$etc$_$kacc1228e.pdf`.

[174] B. Woźniak and V. N. Pelevin, "Optical classifications of the seas in relation to phytoplankton characteristics," *Oceanologia*, vol. 31, 1991.

[175] *LD Driver Datasheet*, Thorlabs, 2018, available at `https://www.thorlabs.com/drawings/b85b512b23d97c61-33F98C48-CF76-0F3E-B4A3A64ADCE0B3D9/CLD1010LP-EnglishManual.pdf`.

[176] S. Zhu, X. Chen, X. Liu, G. Zhang, and P. Tian, "Recent progress in and perspectives of underwater wireless optical communication," *Progress in Quantum Electronics*, p. 100274, 2020.

[177] Y. X. Yap, F. Jasman, and T. C. E. Marcus, "Impact of chlorophyll concentration on underwater optical wireless communications," in *2018 7th International Conference on Computer and Communication Engineering (ICCCE)*, 2018, pp. 1–6.

[178] N. Anous, M. Abdallah, M. Uysal, and K. Qaraqe, "Performance evaluation of LOS and NLOS vertical inhomogeneous links in underwater visible light communications," *IEEE Access*, vol. 6, pp. 22408–22420, 2018.

[179] X. Huang, F. Yang, and J. Song, "Hybrid LD and LED-based underwater optical communication: state-of-the-art, opportunities, challenges, and trends," *Chinese Optics Letters*, vol. 17, no. 10, pp. 100002, 2019.

[180] Y. Ito, S. Haruyama, and M. Nakagawa, "Short-range underwater wireless communication using visible light LEDs," *WSEAS Transactions on Communications*, vol. 9, pp. 525–552, 2010.

[181] A. Uppalapati, R. P. Naik, and P. Krishnan, "Analysis of M-QAM modulated underwater wireless optical communication system for reconfigurable UOWSNs employed in river meets ocean scenario," *IEEE Transactions on Vehicular Technology*, vol. 69, no. 12, pp. 15244–15252, 2020.

[182] R. Jiang, C. Sun, L. Zhang, X. Tang, H. Wang, and A. Zhang, "Deep learning aided signal detection for SPAD-based underwater optical wireless communications," *IEEE Access*, vol. 8, pp. 20363–20374, 2020.

[183] L. Zhang, X. Zhou, J. Du, and P. Tian, "Fast self-learning modulation recognition method for smart underwater optical communication systems," *Optics Express*, vol. 28, no. 25, pp. 38223–38240, 2020.

[184] A. Trichili, C. B. Issaid, B. S. Ooi, and M. S. Alouini, "A CNN-based structured light communication scheme for internet of underwater things applications," *IEEE Internet of Things Journal*, vol. 7, no. 10, pp. 10038–10047, 2020.

[185] X. Li, X. Hu, R. Zhang, and L. Yang, "Routing protocol design for underwater optical wireless sensor networks: A multiagent reinforcement learning approach," *IEEE Internet of Things Journal*, vol. 7, no. 10, pp. 9805–9818, 2020.

[186] H. Lu, W. Chen, and M. Jiang, "Deep learning aided misalignment-robust blind receiver for underwater optical communication," *IEEE Wireless Communications Letters*, vol. 10, no. 9, pp. 1984–1988, 2021.

[187] X. Cui, X. Yin, H. Chang, H. Liao, X. Chen, X. Xin, and Y. Wang, "Experimental study of machine-learning-based orbital angular momentum shift keying decoders in optical underwater channels," *Optics Communications*, vol. 452, pp. 116–123, 2019.

[188] Z. Huang, L. Zu, Z. Zhou, X. Tang, and Y. Ji, "Computer-vision–based intelligent adaptive transmission for optical wireless communication," *Optics Express*, vol. 27, no. 6, pp. 7979–7987, 2019.

[189] M. Elamassie, M. Uysal, Y. Baykal, M. Abdallah, and K. Qaraqe, "Effect of eddy diffusivity ratio on underwater optical scintillation index," *Journal of the Optical Society of America A*, vol. 34, no. 11, pp. 1969–1973, 2017.

[190] K. N. Fedorov, *The Thermohaline Finestructure of the Ocean: Pergamon Marine Series*, vol. 2, Elsevier, 2013.

[191] T. Radko, *Double-diffusive convection*, Cambridge University Press, 2013.

[192] E. Kunze, "A review of oceanic salt-fingering theory," *Progress in Oceanography*, vol. 56, no. 3-4, pp. 399–417, 2003.

[193] I. S. Gradshteyn and I. M. Ryzhik, *Table of integrals, series, and products*, Academic press, 2014.

[194] E. W. Ng and M. Geller, "A table of integrals of the error functions," *Journal of Research of the National Bureau of Standards*, vol. 73B, no. 1, pp. 1–20, 1969.